論文 / 著書情報
Article / Book Information

題目(和文)	
Title(English)	Study on site characterization and strong ground motion estimation in the western Marmara region, Turkey
著者(和文)	KARAGOZOZLEM
Author(English)	Ozlem Karagoz
出典(和文)	学位:博士(学術), 学位授与機関:東京工業大学, 報告番号:甲第10571号, 授与年月日:2017年3月26日, 学位の種別:課程博士, 審査員:山中 浩明,海江田 秀志,田村 哲郎,翠川 三郎,盛川 仁,松岡 昌志
Citation(English)	Degree:Doctor (Academic), Conferring organization: Tokyo Institute of Technology, Report number:甲第10571号, Conferred date:2017/3/26, Degree Type:Course doctor, Examiner:,,,,,
学位種別(和文)	博士論文
Type(English)	Doctoral Thesis

Study on site characterization and strong ground motion estimation in the western Marmara region, Turkey

OZLEM KARAGOZ

Supervisor: Prof. Dr. Hiroaki Yamanaka

Interdisciplinary Graduate School of Science and Engineering
Department of Environmental Science and Technology
Tokyo Institute of Technology

February 2017

Study on site characterization and strong ground motion estimation in the western Marmara region, Turkey

OZLEM KARAGOZ

Supervisor: Prof. Dr. Hiroki Yamanaka

A Thesis presented to
the Faculty of the Department of Environmental Science and Technology
Tokyo Institute of Technology
In fulfillment of the Requirements of the Degree

Doctor of Philosophy

February 2017
Tokyo, Japan

Study on site characterization and strong ground motion estimation in the western Marmara region, Turkey

KARAGOZ OZLEM

Prof. Dr. Hiroaki Yamanaka
Academic Advisor

Committee Members

Prof. Dr. Saburoh Midorikawa
Department of Architecture and Building Engineering Department
Tokyo Institute of Technology

Prof. Dr. Hitoshi Morikawa
Department of Architecture and Building Engineering Department
Tokyo Institute of Technology

Assoc. Prof. Dr. Masashi Matsuoka
Department of Architecture and Building Engineering Department
Tokyo Institute of Technology

Prof. Dr. Tetsuro Tamura
Department of Environmental Science and Technology
Tokyo Institute of Technology

Prof. Dr. Hideshi Kaieda
Central Research Institute of Electric Power Industry
Japan

ACKNOWLEDGMENT

I would like to express my sincere gratitude to my supervisor Prof. Hiroaki Yamanaka and Asst. Prof. Dr. Kosuke Chimoto of the Department of Environmental Science and Technology, Tokyo Institute of Technology, who gave me an opportunity for my doctoral study in Japan, sincerely supervised and guided me throughout my studies. Thanks for their patience, for their understandings, guidance, constructive suggestions and criticisms. Prof. Hiroaki Yamanaka always compelled me to become a better investigator and tries to orient me towards to think and approach scientific when I studied on the other researcher's studies. When I think that I could not continue, he encouraged me.

I would like to express my deepest gratitude to my supervisor Prof. Dr. Oguz Ozel from Istanbul University, in Turkey. He always supports and encourages me during my Ph.D. education since 2010. I think it is a big change for me to meet him. He offered Ph.D. education in Japan that is the greatest contribution in my education life.

I am also thankful to all my teachers who contributed to my education and mental development in my life since elementary school.

I am thankful to the Engineering Faculty, Canakkale Onsekiz Mart University for their supports during my Ph.D education. I also would like to express gratitude to the Japan Ministry of Education, Culture, Sport, Science, and Technology (MEXT) for financial support to my PhD education at the Tokyo Institute of Technology, and Japan Science and Technology Agency (JST) and Japan International Cooperation Agency (JICA) for the financial support in conducting the field survey under the SATREPS project MarDiM "Earthquake and Tsunami Disaster Mitigation in the Marmara Region and Disaster Education in Turkey". I would like to thank to Dr. Seckin Ozgur Citak (JAMSTEC) and Dr. Hatayama Ken for their contribution for the field studies and also Mehmet Safa Arslan and Bengi Behiye Aksahin who are the master student in Istanbul University.

I would like to thank all my fellow lab-mates in Yamanaka lab: Dr. Hussam Eldein Zaineh, Dr. Koichiro Saguchi san, Andi Muhamad Pramatadie (Rama), Saifuddin (Udin), Mohamed Amrouche , Noyori san , Imai san, Sorimachi san, Nogami san, Kojima san, Tsuchiya san, Hirose san, Liu san, Ishihara san, Ishige san, Shimizu san, Chujo san, Yuny Shofy, Miyanaga san, Seita san, Miyakoshi san, Harigaya san and Ozgur Tuna Ozmen (from AFAD) for their

support and stimulating discussions, as well as for togetherness during lab seminars and for all the fun during lab activity in the last three and half years. My special thanks to Shimamoto san for her assistance in the laboratory documents and coffee-time talks during my stay.

I also would like to thank my best friends Ong Soo Peng from Malaysia, Aliya Arenova from Kazakhstan, Maria Gurova from Rusia and Anissa Nurdiawati from Indonesia for their honest friendships, considerable advises and supports in Japan.

Finally, I would like to express the profound gratitude from my deep heart to my beloved mother Suna, father Cahit, sister Ipek Elif, and brother Kutluer. Without my parents' continuous support and encouragement in both spiritually and mental throughout my life, I would not have been here to take on this study.

To all of you, I am eternally grateful.

Table of Contents

ABSTRACT

The most important key to assessing of earthquake hazard is the prediction of ground motion that is controlled by source, path and site effects. It is essential that characterizing earthquake source, the effect of the propagation path from source to the seismic or engineering bedrock, and amplification of shallow soil structures are defined as accurate as possible to close the real ones in simulation studies to predict and mitigate the damage of a future earthquake in a broadband frequency range. Among them, local geological and soil conditions (site effects) have sometimes played a principal role on damage of buildings due to the essential characteristics such as amplitude, frequency content, and duration of strong ground motions.

In this study, the characteristic of ground motions was investigated using 1D simulation of past two earthquakes in the western Marmara Region. First, the S-wave velocity structures of shallow sedimentary layers down to the engineering bedrock were explored by applying short-period microtremor array measurements on the different geological units in Tekirdag and surrounding area. The observed Rayleigh wave phase velocities were between ~90 and 930 m/s in a frequency range from 2 to 30 Hz. The S-wave structures of the shallow soil in Tekirdag city center and coastal area were deduced. The top layers of sites located on the sandstone, claystone, and siltstone units had velocities of ~200 m/s. One of significant result of the study was clearly identification of the S-wave velocities and thickness of the alluvial creek beds in coastal area. The observed phase velocities change due to the thickness of alluvium and shapes of them were similar. The engineering bedrock velocities in the study area ranged from 700 to 930 m/s. The site amplifications, predominant frequencies, and site classifications according to the AVs30 values were also determined to be a proxy for future microzonation studies in Tekirdag and surroundings. According to the NEHRP site classification, about 67% of the observation sites are on dense soil/soft rock (class C) and about 26% of them are on stiff soil (class D). The results indicate that Tekirdag city center and the northern parts have amplifications from 3 to 6 with fundamental frequency range of 2-3 and 4-6 Hz, respectively. Most of the sites located on claystone, sandstone and siltstone units in Tekirdag had predominant frequencies higher than 2 Hz. The fundamental frequency range in Tekirdag was 1-10 Hz while the predominant frequency

range was 1-16 Hz. The relationship equations for AVs30-slope and AVs30-amplification were proposed for future usage in site response prediction studies.

The second part of this study is to determinate 1D deep velocity structures from the engineering bedrock to Moho beneath the 12 strong ground motion stations operated by Prime Ministry Disaster and Emergency Management Authority, Republic of Turkey (AFAD) in different azimuthal directions by comparing theoretical surface wave group velocity dispersion curves with the observed ones of the 2014 Gokceada mainshock' seismograms. This approach is provided to determine effectively the S-wave velocities and thickness of the layers in the upper 4-5 km part of the crust. The tuned models have deeper layer interfaces depths than the initial model defined from previous studies. The engineering bedrock thicknesses are found thicker than the initial model.

The third part of this study is to validate the integrated 1D crustal velocity structures from the surface to Moho and to model ground motions of the latest moderate 2014 Gokceada mainshock in the region. Its broadband (0.1-10 Hz) ground motions were simulated with a characterized source model and the 1D shallow and deep subsurface structures. The characterized source model of the earthquake was defined utilizing the slip distribution from analysis of teleseismic data (Pinar, 2014) and the strong ground motion recipe (Irikura and Miyake, 2011). It consisted of one asperity area and background area to predict low and high frequencies, respectively. The seismogram on the engineering bedrock of each sub-fault was calculated with the discrete wavenumber method. The point source summation technique with the rupture times was performed to get synthetic waveform in the time domain. The linear approximation of the site amplification was used in the frequency domain to estimate surface ground motions.

The results indicate that the defined asperity area in the source model is sufficient to generate high frequency synthetic ground motions of the 2014 Gokceada earthquake. The importance of a proper 1D deep velocity structure beneath engineering bedrock to simulate low frequencies is emphasized. The synthetic arrival times of the body and surface waves are similar to the observations because the subsurface models have been constructed from the surface wave group velocity dispersion analyses. The S-wave velocity structure of the shallow soils was also included into the models to obtain the effects of the complete 1D crustal velocity structure from the surface to Moho. The local site effects were mostly successfully generated on the synthetic high

frequency seismograms. It is clear that the 1D simulation cannot generate sufficient results at special sites where on a thick sediment basin with low seismic velocity or at large epicentral distances (i.e. >150 km).

The final part of the study is investigation of the destructive historical 1912 Murefte (Mw 7.3) earthquake ground motions in the region. The characterized source model was defined using previous studies. Two source models with two and three asperities were examined. The 1D simulation for the characterized source models were performed using the 1D velocity structure at the strong motion sites. The characteristic source model with three asperities is much appropriate for the 1912 Murefte earthquake because the intensity differences are minimum at the sites. The estimated near-fault strong ground motions indicate that characteristics of the spectral accelerations change according to the site location respect to the location of fault and asperities. The amplitudes of the spectral acceleration of the sites are higher than the limits of the Turkish Building Code (2007).

The broadband 1D simulation of the past two earthquakes were succeeded to estimate the response of the 1D deep velocity structures from the engineering bedrock to Moho and to generate the high frequency ground motions including the local site effects. The results of this study can be used for more reliable estimation of scenario earthquake simulations and seismic hazard evaluation in the Marmara Region.

Chapter 1

Introduction

1.1 Background of the Research

1.2 General Tectonic Settings and Seismicity of the Marmara Region

1.3 Previous Researches on Site Effects and Seismic Hazard in the Marmara Region

1.3.1 Site effect studies

1.3.2 Seismic hazard studies

1.3.3 Previous studies on the 24 May 2014 Gokceada Earthquake

1.3.4 Previous studies on the 9 August 1912 Murefte Earthquake

1.4 Objectives of the Research

1.5 Thesis Organization

1.1 Background of the Research

Destructive earthquakes with magnitudes larger than 7 (M ≥ 7) such as 1985 Michoacan (Mexico), 1995 Kobe (Japan), 1999 Kocaeli and Duzce (Turkey), 2014 Iquique (Chile) and Nagano (Japan), 2015 Gorkha (Nepal) and 2016 Kumamoto (Japan) show that local site conditions have a major effect on characteristics of ground shaking. S-wave velocity (Vs) structure is an important parameter in site amplification calculations for earthquake damages scenarios. Validating site effects is inevitable to estimate earthquake ground motion and disaster mitigation. Therefore, one of the important points for local seismic hazard studies is the definition of 1D velocity structure from the surface to the seismic or engineering bedrock. This is necessary to know site responses to estimate strong ground motions impact of the buildings.

The most important key for assessing and mitigation of earthquake disaster is prediction of ground motion as close as real one. It is the first step of an earthquake damage assessment. Prediction of ground motion generally consists of two processes that are shown in Figure 1.1. The first process is prediction of ground motion on seismic bedrock or engineering bedrock and the second process is evaluation of soil effect in sedimentary layers. After both processes are calculated, ground motion at the surface can be predicted.

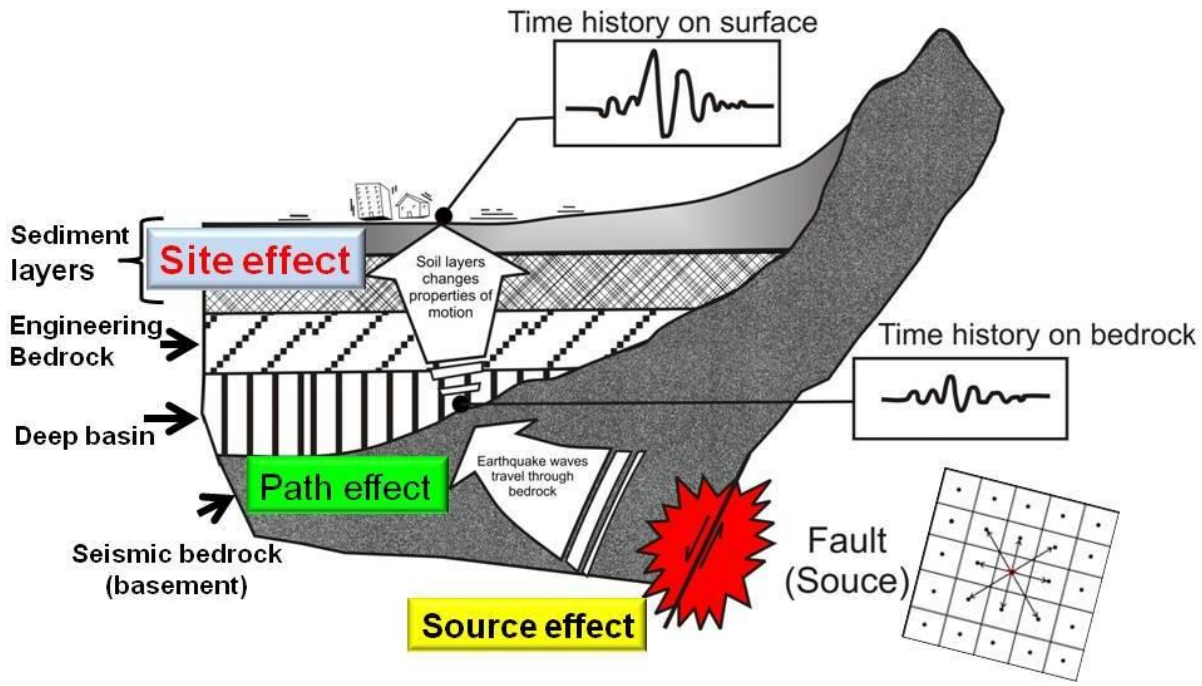

Figure 1.1 Schematic illustration of wave propagation through seismic bedrock and soil surface (modified from http://seismo.geology.upatras.gr/MICROZON-THEORY1.htm).

The amplitude of a ground motion is controlled by three major effects: source, path and site effects as shown in Figure 1.1. Among them, site effects have sometimes played a principal role on damage to buildings due to local geological and soil conditions. Local site conditions can profoundly influence all the important characteristics such as amplitude, frequency content, and duration of strong ground motion (Kramer, 1996, at p: 309). The local geology significantly modifies strong motion characters and controls the irregular distribution of damage observed during large earthquakes. Therefore, shallow low-velocity layers are responsible for variation of earthquake ground motion amplification in an area. Heterogeneity of the soil structures, velocity impedance differences between layers, resonant effects, irregular topography of the layers beneath a basin, effect of the surface topography, nonlinear soil behavior, fault geometry and lateral variation of S-velocity causes variation of earthquake ground motion amplifications. Most of these effects cannot be determined easily and comprehensive studies are needed. On the other hand, it is important to estimate S-wave velocity structure in near surface layers for estimating strong motion characteristics during an earthquake. One-dimensional (1D) soil profile can be obtained by different geophysical methods, using earthquake data or ambient noise recording to retrieve the vertical soil structure as well as borehole logging. The 1D assumption of the soil structure is widely accepted and easy to implement. Array exploration of microtremors has been gaining much popularity in 1D Vs profiling because estimation of Vs structure requires only a simple circular array with a few seismometers. If the microtremors are recorded by vertical sensors, they are often regarded to have the dispersive characteristics of Rayleigh waves. Additionally, surface wave group velocity dispersion curves from ground motions of an earthquake can be used to determine the horizontal 1D velocity structures for deep sediments and earth's crust from focal layer to the engineering bedrock/seismic bedrock beneath a site. If there is no detailed 3D velocity information for a region, determining approximate 1D velocity structure helps to generate more reliable simulation results for seismic hazard studies.

1.2 General Tectonic Settings and Seismicity of the Marmara Region

Turkey is located between the three main tectonic plates: Eurasia, Arabia and Africa. Due to the Eurasian-Arabian continental collision in the east and extensional regime in the west, the Anatolian Plate escapes to the west between the North and East Anatolian strike-slip fault systems as shown in Figure 1.2. The North Anatolian Fault Zone (NAFZ) is one of the significant right-lateral strike-slip faults on the Earth. It is about is about 1,200 km-long between the Eurasian and Anatolian plates. It begins from the eastern Turkey, cuts the Sea of Marmara in roughly east-west direction and then extends to the Aegean Sea in the west (Ketin 1968; Dewey and Sengor 1979; Le Pichon et al. 1987; Barka 1992). The NAFZ has a uniform slip-rate of ~25 mm/yr (McClusky et al. 2000) and releases the accumulated seismic energy with large earthquakes (M>7). The most significant earthquakes occurred along the NAFZ are 1939 Erzincan (M 8.3), 1942 Erbaa-Niksar (M 7.1), 1943 Tosya (M 7.6), 1944 Bolu–Gerede (M 7.3), 1957 Abant (M 7.0), 1967 Mudurnu valley (M 7.1), 1992 Erzincan (M 6.8), 1999 Kocaeli (M 7.4) and 1999 Duzce (M 7.2) (Bozkurt 2001).

The segments of the NAFZ are very close to highly populated cities in the Marmara Region. The segment located in the Marmara Sea is called the Main Marmara Fault. The NAFZ is observed on the land in Gazikoy and then enters to the Saros Bay in north-northeast of Canakkale city and is named the Ganos Fault, as shown in Figure 1.2. According to the historical records, the Marmara Region has been frequently visited by destructive earthquakes (Ambraseys and Finkel 1995). The last two significant earthquakes occurred in the western (9 August 1912 Murefte, Mw 7.3) and eastern (17 August 1999 Kocaeli, Mw 7.4) parts of the region (Figure 1.2) in the last century. The Gokceada earthquake (24 May 2014, Mw 6.9) also affected the west of the region.

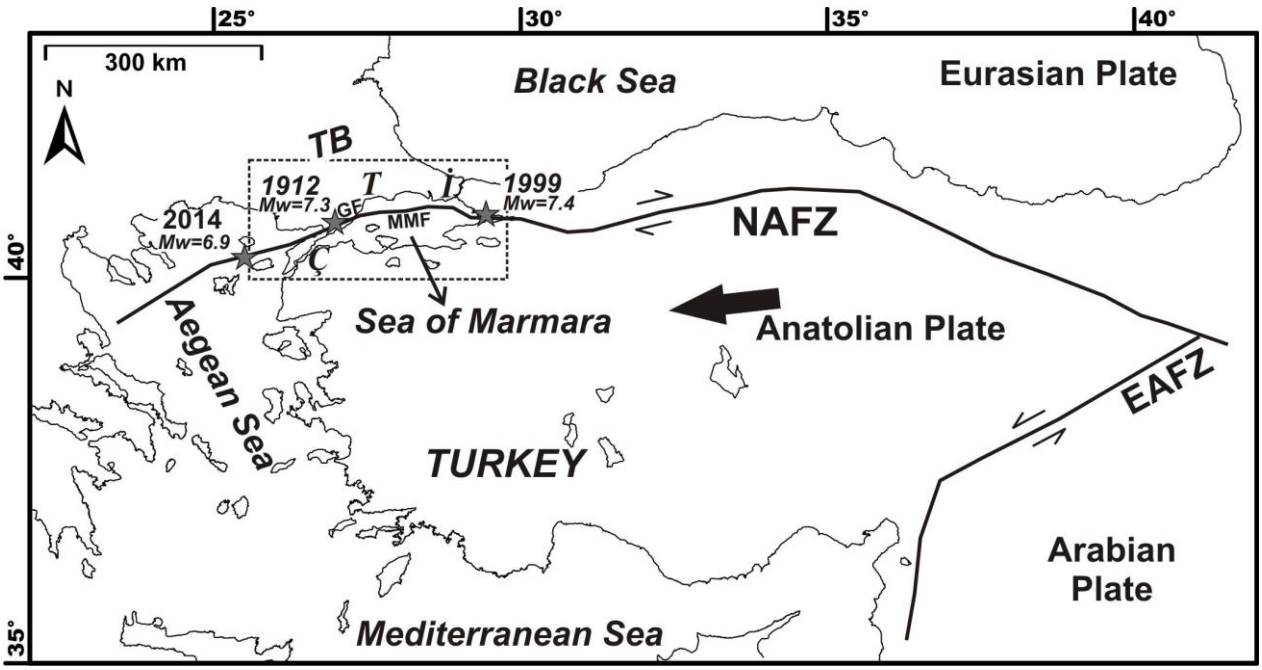

Figure 1.2 Main tectonic units and fault systems in Turkey. The Marmara Region is shown in the rectangle. Ç: Çanakkale, İ: Istanbul, T: Tekirdag. EAFZ: East Anatolian Fault Zone, NAFZ: North Anatolian Fault Zone, MMF: Main Marmara Fault, GF: Ganos Fault, TB: Thrace Basin. Stars show the significant earthquakes in the last century.

The Marmara Region is one of the seismically active regions in the world. The epicenters of the earthquakes that occurred after 1970 in the catalog of Bogazici University - Kandilli Observatory and Earthquake Research Institute National Earthquake Observatory Centre (BU-KOERI) with magnitude larger than 3 (M $\geq$3.0) are shown in Figure 1.3. A large number of earthquakes are observed at Tekirdag Basin and Cinarcik Basin in the Marmara Sea. The activity also continues in the northern Aegean Sea, around Gokceada on the North Aegean Though (NAT). Contrary, there is extremely low seismicity on the Ganos Fault segment and Main Marmara Segment. Therefore, most of the research studies focus on the seismic gap area where the possible future earthquake may occur. The depth section of the earthquakes along the NAFZ is given in Figure 1.3 along the profile ABC. The focal depths reach to about 20 km in the region (Figure 1.3). This is the evidence for the width of the seismogenic zone. The focal mechanism solutions of the three major earthquakes have the similar strike-slip mechanism on the NAFZ.

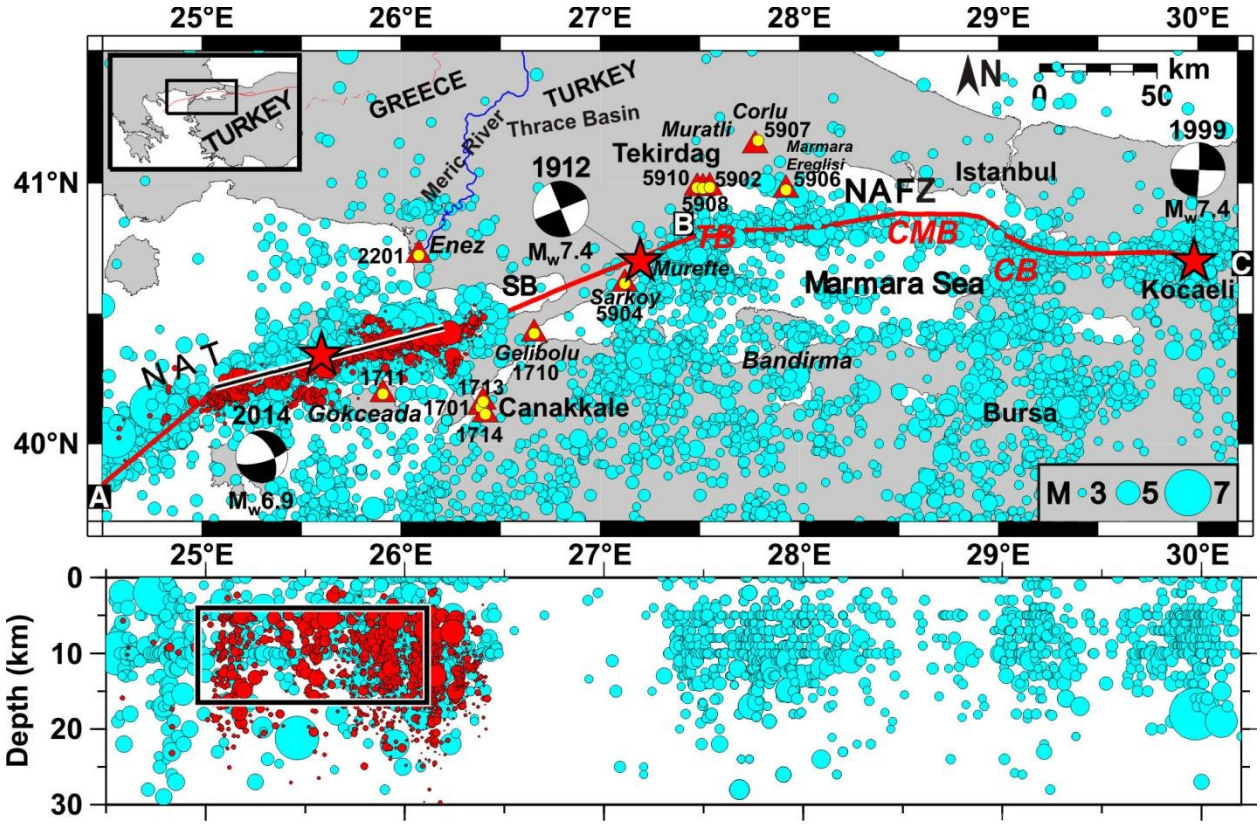

Figure 1.3 Seismicity map of the Marmara Region (top) and the depth section of the earthquakes along the NAFZ (red line) on the ABC profile (bottom). Blue circles represent the earthquakes between 1970 and November 2016 with M ≥ 3.0 in the BU-KOERI database. Red circles are the aftershocks of the 2014 Gokceada earthquake with M ≥ 1 (May-August 2014) on the NAT. The focal depth of the 2014 Gokceada mainshock is given as 21.2 km in the KOERI catalogue. The focal mechanism solutions of the 2014 Gokceada, 1912 Murefte and 1999 Kocaeli mainshocks (red starts) are from Pinar (2014), Aksoy et al. (2010) and Taymaz (1999), respectively. The red triangles and yellow circles show the AFAD strong ground motion stations and microtremor array sites, respectively. The black rectangle on the depth section is the ruptured area of the 2014 Gokceada earthquake given by Pinar (2014) and the black line on the map is its projection. NAT: North Aegean Through; SB: Saros Bay, TB: Tekirdag Basin, CMB: Central Marmara Basin, CB: Cinarcik Basin. The districts of the main cities are written in italic letters.

1.3 Previous Researches on Site Effects and Seismic Hazard in the Marmara Region

1.3.1 Site Effect Studies

The importance of site effect studies has been more widely recognized since the 1999 Kocaeli earthquake (Mw 7.4) in the Marmara Region (NW Turkey), especially in the Istanbul megacity. There have been several site effect studies for Istanbul, Kocaeli, Yalova and Bursa cities. Although the Avcilar district of Istanbul in the western part of the city is ~150 km far from the Kocaeli earthquake epicenter, many buildings collapsed during the earthquake. This demonstrates that even places that are far from an earthquake source cannot be considered safe.

Ozel et al. (2002, 2004), Kudo et al. (2002), Ergin et al. (2004), Bozdag and Kocaoglu (2005), and Kilic et al. (2006) studied site effects in the western Istanbul (Avcilar, Yesilkoy, Bakirkoy, Zeytinburnu districts) using aftershock and microtremor records. They reported the existence of low S-wave velocities (~200 m/s) for shallow layers, and high amplifications at low frequencies (<5 Hz). Picozzi et al. (2009) studied in seven districts of Istanbul city (Avcilar, Bakirkoy, Atakoy, Gungoren, Bagcilar, Fatih, Kagithane) by using a single station microtremor measurements method. They collected single station data at 192 sites and array measurement at 8 sites and found that the complex S-wave velocity structures. Most of the sites were characterized by amplification factors higher than 2 in the frequency range from 0.2 to 10 Hz. They also introduced the stiff Paleozoic bedrock with a velocity of 2000 m/s. On the other hand, Sarosen et al. (2006) applied the 3D finite difference method to obtain 1D velocity model with site effects for a local 3D velocity structure at Atakoy and its surrounding area. They used engineering bedrock S-wave velocity as 1490 m/s for the 1D velocity model. They obtained dominant peak amplifications of 3-4 around 1 Hz from microtremor horizontal to vertical ratio (H/V) results. They also simulated a target earthquake of magnitude 7.5 in the Marmara Sea, and found a minimum amplification factor 1.5 within the frequency band of 0.5-1.5 Hz. Birgoren et al. (2009) targeted to the south coast of Istanbul to determine the depth of seismic bedrock. The maximum depth was found as about 440 m in the southwest of Istanbul. Additionally, the engineering bedrock velocity was determined 760 m/s by using microtremor array measurements and borehole data. H/V ratios indicated that resonance frequencies are as high as 1.5 and 5 Hz in European and Asian sides of Istanbul city, respectively.

The site effects in the Kocaeli metropolitan area (eastern Marmara) area were investigated and the 3D basin structure was mapped (Zor et al. 2010; Ozalaybey et al. 2011). Yalcinkaya et al. (2013) collected single station data along the coastline of Yalova city located in west of Kocaeli. They observed high amplifications at 0.5-2 Hz in the residential areas on the alluvial creek beds. They found a resonance peak around 1 Hz and flat amplification factor for valley and ridge sites in Yalova, respectively. Gok and Polat (2012) studied site effects in Bursa city and obtained the dominant frequency less than 2 Hz at the sites in the Neogene and Quaternary ages of the basin. The rock sites in Bursa show the dominant frequencies higher than 5 Hz in an agreement with the surface geology of the city. The latest study in this region was done by Ozmen et al. (2016). They performed microtremor array explorations in Kocaeli, Yalova and Bursa and showed that the dominant fundamental frequencies in the amplification factors were distributed in a frequency range from 0.7 to 5 Hz at AFAD strong motion stations.

Asten et al. (2014) collected microtremor array data at the AFAD stations in Bolu and Duzce. They applied Spatial Autocorrelation Coefficient (SPAC) method and found a surface layer with an S-wave velocity of less than 200 m/s and with a thickness of 5 m and 6 m for Bolu and Duzce, respectively. They accepted that H/V was from the fundamental mode of Rayleigh wave and determined two moderate Vs contrast interfaces in soft Miocene and Eocene sediments at a depth between 136 and 209 m, and at a depth in the range from 2000 to 2200 m, respectively.

The previous studies were concentrated in the eastern Marmara Region and there has been no comprehensive site effect study in the western part of the Marmara Region. Therefore, one of the objectives of this study is to explore the 1D Vs layer structures of shallow depths (0-250 m) from microtremor explorations in Tekirdag city center, Muratli, Corlu, Marmara Ereglisi and at the AFAD stations in Gelibolu, Sarkoy, Enez, Gokceada and Canakkale city center for future engineering applications.

1.3.2 Seismic Hazard Studies

Marmara Region as mentioned above suffered from destructive earthquakes and was selected as Supersites (http://supersites.earthobservations.org/) that are principle study regions for natural hazards in the world. Simulation of the large earthquakes is important for hazard analyses and mitigation of the damage for the region. The latest destructive earthquake (1999 Kocaeli) occurred in eastern Marmara and affected Kocaeli, Yalova and Istanbul cities while there were no significant events affected central and western Marmara for more than a hundred years. The latest earthquake was 1912 Murefte event in the west part of the region and the ruptured fault segment may be re-activate in future.

After the 1999 Kocaeli earthquake, site effect and ground motion simulation studies have been focused in the large cities (i.e. Istanbul, Yalova, Kocaeli, Bursa) in the eastern Marmara Region (i.e. Erdik 1999: Erdik and Durukal 2001; Erdik et al. 2004; Ozel et al. 2004, Pulido 2004; Erdik 2005; Sorensen et al. 2007; Tanırcan and Savas 2011; Tanırcan 2012; Yalcinkaya et al. 2012; Aochi and Ulrich 2015; Mert et al. 2016; Spagnuolo 2016; Sahin 2016; Douglas and Aochi 2016). Probabilistic (Atakan et al. 2002; Erdik et al. 2004) and hybrid (Pulido et al. 2004; Sørensen et al. 2007, Ansal et al. 2009; Tanircan 2012) simulations were used in hazard studies for the Marmara Region. Deterministic simulation to obtain low frequencies and semi-stochastic method for high frequency part of ground motion on bedrock were combined in hybrid simulation studies of Pulido et al. (2004) and Sørensen et al (2007). Similarly, Erdik and Durukal (2001) were applied discrete wave number approach and stochastic simulation for low and high frequency parts of ground motion for a port facility near the NAFZ in Kocaeli. A finite difference algorithm with a 3D velocity structure and a stochastic method were performed by Tanircan (2012) to simulate ground motions in Istanbul for different scenario earthquakes with M_w 7.2. Mert et al. (2014a, b) also used a hybrid simulation for an earthquake close to Istanbul. They obtained low and high frequency parts using a finite difference algorithm and empirical Green's functions, respectively. Aochi and Ulrich (2015) performed strong motion simulation of dynamic rupture on the fault in the Marmara Sea. Douglas and Aochi (2016) were simulated many earthquakes in the Marmara Region to demonstrate ground motion variability due to the path. Sahin et al. (2016) introduced an integrated earthquake simulation system for Zeytinburnu district of Istanbul.

Figure 1.4 shows the areas studied in details on the peak ground acceleration (PGA) map with 10% probability of exceedance in 50 years (475-year return period) on the soft rock given by Kuzak (2003). There is no similar study in the western part of the Marmara Region. A part of the area is not sufficient for generating reliable hazard scenarios for past and future earthquakes for whole Marmara Region. To generate complete seismic hazard maps (i.e. PGA/PGV, intensity) and then understand possible damages in the future earthquake in whole Marmara, it must be enlarged observation area and knowledge. Therefore we focus on the western Marmara Region in northwestern Turkey (Figure 1.4).

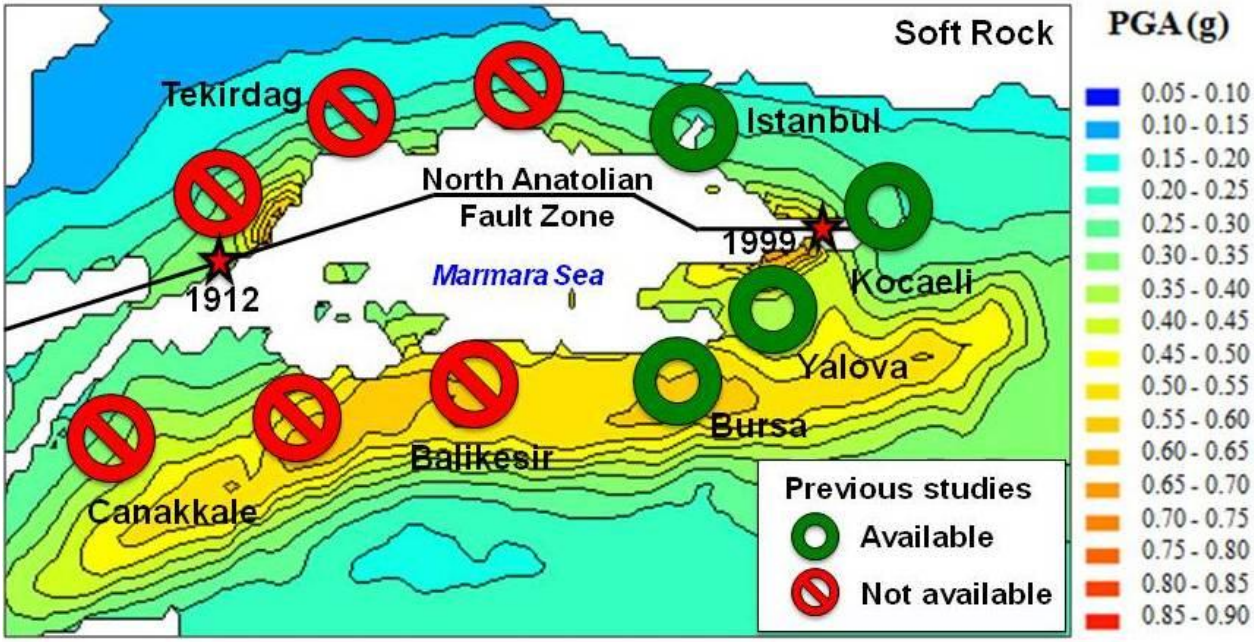

Figure 1.4 PGA map with 10% probability of exceedance in 50 years for soft rock is given by Kuzak (2003). Available and non-available site effect studies are given by green and red circles, respectively. The black line shows the NAFZ.

Figure 1.5 shows the seismic zone maps of the study area prepared by AFAD in 1996 based on the report of Gulkan et al. (1993, *"Turkey Earthquake Regions According to the Latest Data"*). The distance between the NAFZ and Tekirdag city center is about 20 km. For this reason, characteristics of earthquake ground motions in Tekirdag city center and its important districts (Muratlı, Corlu and Marmara Ereglisi) that are located in the 2nd and 3rd degree seismic zones were investigated for future engineering applications. Because of proximity of Ganos segment of NAFZ, Gazikoy, Sarkoy, Enez, Gelibolu and Canakkale city center are in the 1st degrees of

seismic zone maps. The NAFZ passes 30-35 km away from Canakkale city center. All the sites are considered vulnerable to a possible future major earthquake in the region like Istanbul with the PGA value of 0.4 g (~400 cm/s^2) in Figure 1.4.

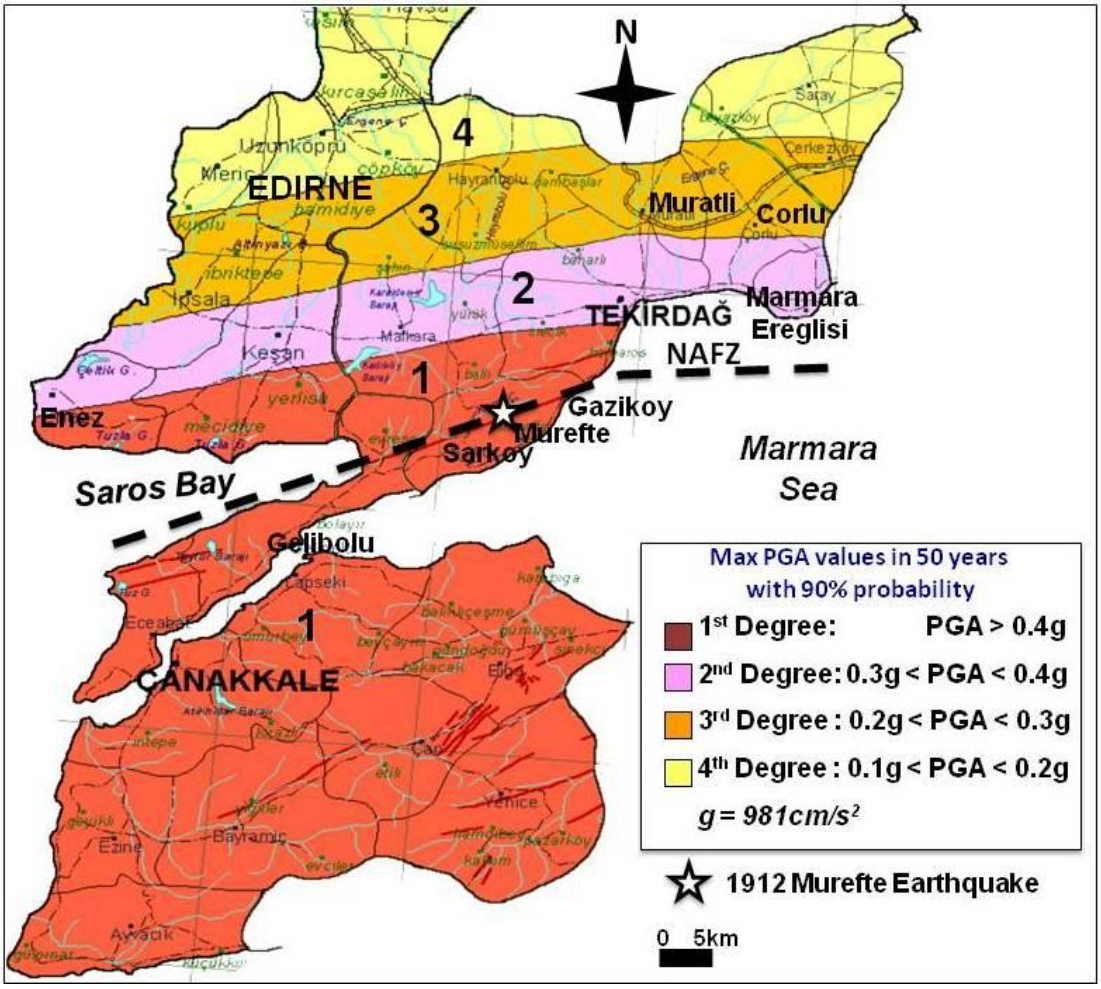

Figure 1.5 Seismic zonation map of Tekirdag and Canakkale prepared by AFAD (http://www.deprem.gov.tr/depbolge/).

Hence the Marmara Region has the smallest area among the seven geographical regions of Turkey (Aegean, Black Sea, Central Anatolia, Mediterranean, Eastern Anatolia and Southeastern Anatolia regions), it covers a rapidly growing part of the country and encompasses the main financial and industrial centers, including Istanbul which is one of the most populated cities in the world. In this study, our main target area was Tekirdag and surrounding area where the second largest province with populations of ~1 million (150 km away from Istanbul). The city is located on the northwestern coastline of the Sea of Marmara with space available for future increases in

urbanization and industrialization. Although Tekirdag is close to Istanbul, there have been no studies to define shallow velocity structures to the engineering bedrock for the city. Canakkale that will be the location of the forth suspension bridge between Asia and Europe in a few years later is another important city in the region.

The last two significant earthquakes, 9 August 1912 Murefte (Mw 7.3) and 24 May 2014 (Mw 6.9) Gokceada, occurred on the Ganos segment and North Aegean Though, respectively in the western Marmara Region (Figure 1.2, 1.3). Therefore, the effect of the sub-surface structures on the broad band ground motions of the 2014 Gokceada earthquake and characteristics of strong ground motions of the 1912 Murefte earthquake must be understood by performing 1D simulation for feature more reliable earthquake hazard estimations.

1.3.3 Previous Studies on the 24 May 2014 Gokceada Earthquake

The Mw 6.9 earthquake occurred on the 24 May 2014 in the west of Gokceada Island, northern Aegean Sea with an epicenter located at the western end of the NAFZ. The mainshock and its three-month aftershocks distribution with magnitude larger than one ($M \geq 1$, May-August 2014) with a depth section are shown in Figure 1.3. It is noted that the mainshock was recorded at the 12 AFAD strong motion stations in the study area.

The 2014 Gokceada earthquake was felt in Turkey, Greece and Bulgaria according to a report of KOERI (Erdik et al. 2014). The earthquake caused moderate damage to about 300 buildings (50 of them in Canakkale city and 200 of them located in Gokceada Island) and slight damage at eight school buildings in the Marmara Region. After the main shock, a low-level aftershock activity was observed along the North Aegean Trough (Saltogianni et al. 2015), and they were non-uniformly distributed mostly out of the ruptured area (Evangelidis 2015). Evangelidis (2015) pointed out that the rupture had a super-shear velocity of ~5.5 km/s and a focal depth of 15 km using a 1D velocity structure of Karabulut (2006). On the other hand, Saltogianni et al. (2015) found a shallow focal depth of 11 km and a rupture velocity of 3.2 km/s from teleseismic P and SH waveforms modeling. Kiratzi et al. (2016) also showed a similar model with a rupture velocity of 3 km/s and a major slip at depths between 12 and 25 km. Pinar (2014) reported a slip distribution from a teleseismic P-wave inversion of a point source having a 100x12.5 km^2 ruptured area (Figure 1.3) at a hypocenter depth of 7.5 km. The previous studies defined the main

source parameters and the focal depths between 10 and 25 km by using existing 1D velocity crustal structures. The previous studies for this earthquake do not include effects of soil layers in deep and shallow sedimentary layers. For this reason, to define more reliable 1D deep velocity structures using the 1D simulation of 2014 Gokceada earthquake one of the goals of this study.

1.3.4 Previous Studies on the 9 August 1912 Murefte Earthquake

The 9 August 1912 Murefte earthquake (Mw 7.3) occurred on the Ganos Fault in the NAFZ in the western Marmara Region (Altunel et al. 2004). A strong aftershock on 13 September 1912 (Mw 6.8) also occurred near Saros Bay (Aksoy et al. 2010). The earthquake killed 2,800 and injured 7,000 people while about 12,600 houses were totally destroyed (Ambraseys and Finkel, 1987). The number of houses beyond repair was 12,100 and about 15,400 houses were seriously damaged (Figure 1.6). The large public buildings, mosques and churches were destroyed totally in Gazikoy, Hoskoy, Murefte, Sarkoy. The mainshock was recorded by the primitive world seismograph at 23 stations Milne pendulum and mechanical seismograms at 29 stations (Ambraseys and Finkel, 1987). The example of the Omori seismograph records at two stations in Japan and Italy are given in Figure 1.7.

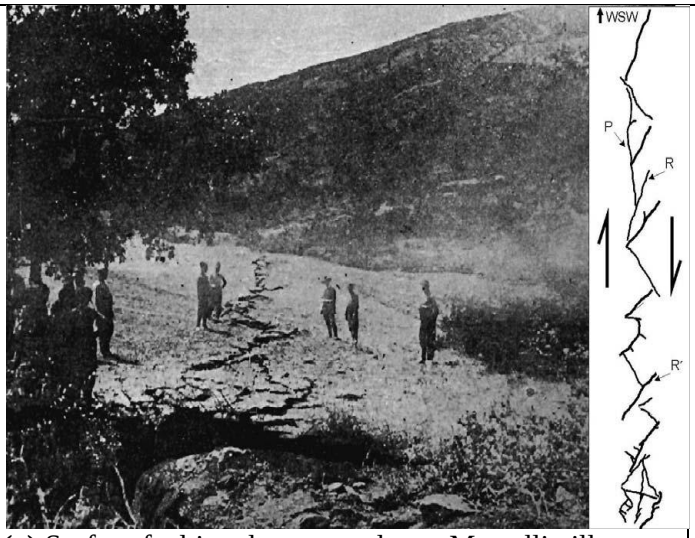

(a) Surface faulting documented near Mursalli village on the north of the Murefte (Mihailovic, 1927; for location see). The sketch map on the right illustrates the rupture zone geometry where the principle displacement zone.

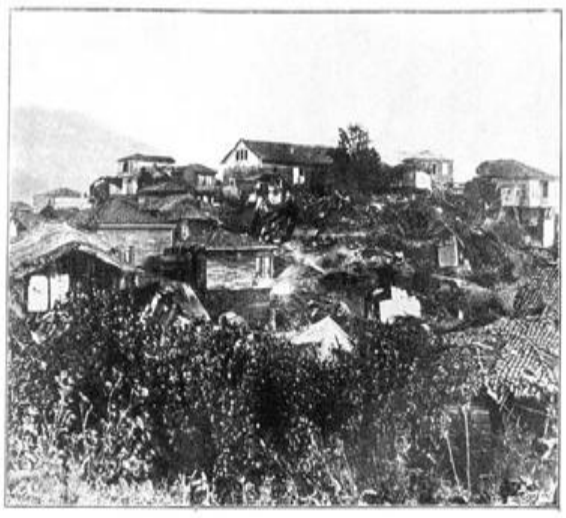

(b) Southern part of the Ganos village (Gazikoy) after earthquake (Macovei, 1912).

(c) A street at Hora (Hoskoy) after the earthquake (Macovei, 1912).

(d) Murefte village.

(e) Collapsed buildings at Sarkoy (Sadi, 1912).

(f) The palace of the Austro-Hungarian Empire consulate was partly damaged (Gelibolu-Canakkale; Mihailovic,1933).

(g) A collapsed house at Tekirdag, build of wood on top of bricks.

(h) Damaged building at Canakkale (Sadi,1912).

Figure 1.6 Observed surface fault (a) and the damage photos of 1912 Murefte earthquake. All photos are taken from Ambraseys and Finkel (1989) and Aksoy (2009, PhD thesis).

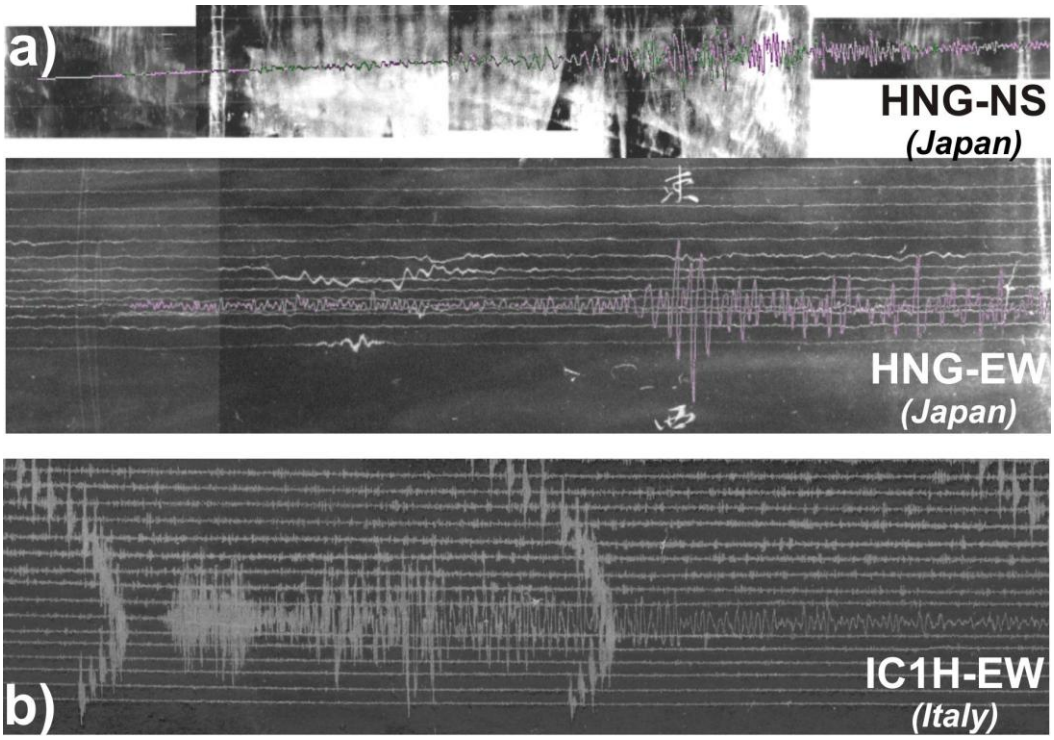

Figure 1.7 Example records of the Omori seismographs of the 1912 earthquake at (a) HNG (Hongo, Japan) and (b) IC1H (Isola D'ischia, Italy) (from Basarir, 2011 Msc Thesis).

Ambraseys and Finkel (1987) indicated that very high damage (intensity IX) was confined within a zone about 20 km wide and 100 km long, extending from SW of Tekirdag to Saros Bay (Figure 1.8). The maximum intensity of the mainshock was X in the Medvedev-Sponheuer-Karnik (MSK-1981) scale around the Ganos Fault. The intensity for Tekirdag and Canakkale cities was between IX and VIII. The rupture length of the mainshock is uncertain. Previous studies suggested a wide range of rupture length from 56 to 150 km (Ambraseys and Jackson 2000; Altinok et al. 2003; Le Pichon et al. 2003; Altunel et al. 2004; Armijo et al. 2005; Aksoy et al. 2010). The rupture was clearly observed on the land with a length of 45-50 km and extended in the Saros Bay in west and the Marmara Sea in east (Figure 1.9). The ruptured part in the sea area is not clear. While Ambraseys and Jackson (2000) calculated the total rupture length as 84 km using the seismic moment of the mainshock, Altınok et al. (2003) found 56 km ruptured fault segment and its 15 km-part was in the Marmara Sea according to the field and multibeam data. However, Aksoy et al. (2010) proposed that the rupture (120±30 km) extended to the center of the Marmara Sea due to the results of the recent submarine studies (Figure 1.9). Coulomb stress change analyses by Cakir et al. (2003) supports that the rupture should not be extent to the central Marmara and stopped south of Tekirdag.

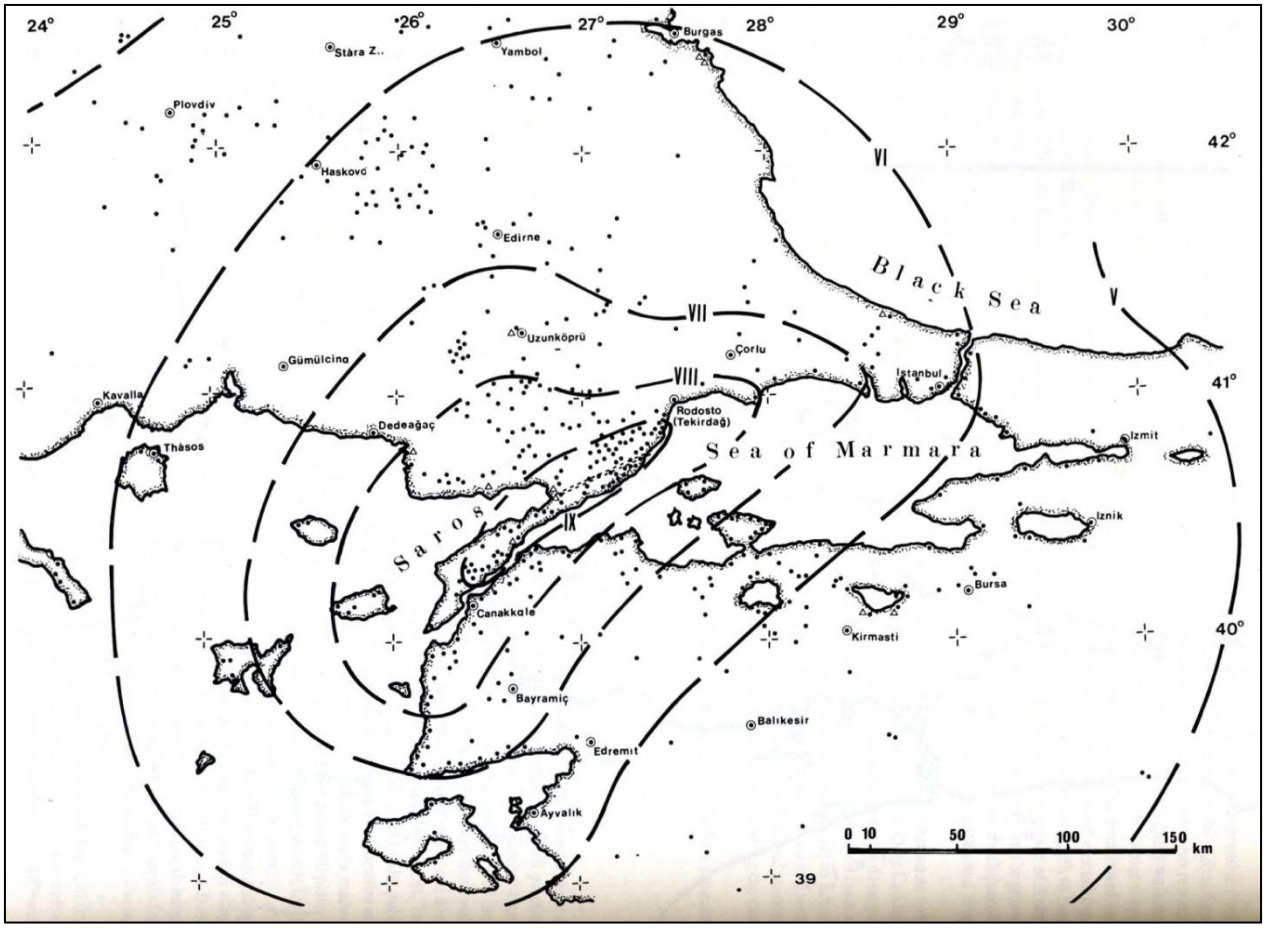

Figure 1.8 Isoseismal map of the 1912 Murefte earthquake by Ambraseys and Finkel (1987). Solid circles shows localities for which it was possible to assign intensities in terms of the MSK scale. Double dashed lines shows location of fault break and associated ground deformations. Open triangle show sites of liquefaction.

There were several displacement measurements along the Ganos Fault. Ambraseys and Finkel (1987) indicate a right-lateral strike slip displacement up to 3 m. However, the most recent studies of Aksoy et al. (2010) combining with previous field data showed that the average slip was 2.5 m (maximum 5.4-5.5 m). They were identified two sub-segments on the Ganos Fault from detail geological and paleoseismological field survey: Yenikoy in west and Guzelkoy in east in Figure 1.9. The average slips on the Yenikoy and Guzelkoy segments were 4.5 and 5 m, respectively. They observed step-over with only one slip measurement (~4m) in the Kavak village where the Ganos Fault enters the Saros Bay. Therefore, they mentioned another possible sub-segment as called the Saros segment in the west that might be the location of the strong aftershock (Mw 6.8).

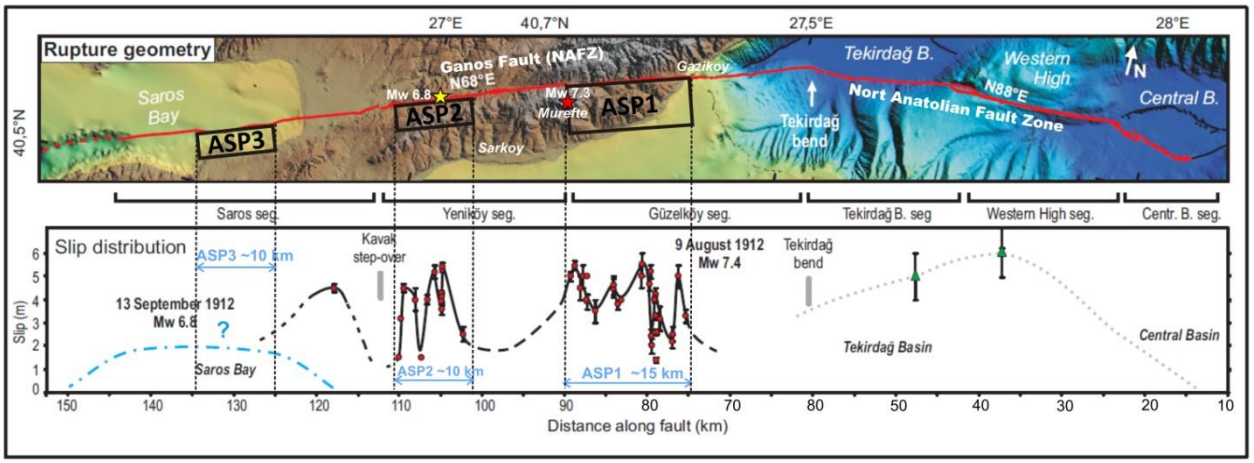

Figure 1.9 The geometry of 150 km-long ruptured fault (red lines on the map) after the1912 mainshock (Mw 7.3) and its strong aftershock (Mw 6.8) given by Aksoy et al (2010). The red and yellow stars show the main shock and aftershock epicenter, respectively. The coseismic slip distribution of the 1912 earthquake defined by detail geological and paleoseismological field surveys on the Ganos Fault (~50 km-length) is given under the map. Possible asperity (ASP) areas used in the 1D simulation are labeled on the map and their possible lengths are given on the slip distribution.

1.4 Objectives of the Research

Characterizing earthquake source, regional wave propagation and site amplification are essential in simulation studies for ground motions in the western Marmara Region. The most important tool is to define the deep and shallow soil structures estimation as accurate as possible. The main goals in this study are listed as below:

- Exploration of S-wave velocity structure of shallow soil to estimate site responses using microtremor array measurements.
- Definition of the 1D deep velocity structures by using earthquake surface wave group velocity dispersion curves analysis of the 2014 Gokceada records in the western Marmara Region (NW Turkey).
- Validation 1D velocity structures and understanding the reason of ground motion amplifications by using deterministic numerical 1D simulation method for the 2014 Gokceada Earthquake.
- Estimation of strong ground motion from source characterization of 1912 historical Murefte earthquake by 1D simulation method utilizing isoseismal map.

1.5 Thesis Organization

This study presents an approach for the first trial 1D velocity structure estimation from the surface to Moho in the western Marmara Region. The site response analysis with defined shear-wave velocity profiles of the shallow soils and the surface wave group velocity dispersion curve analysis for the deep Vs profiles were applied. 1D simulation was applied to validate the shallow and deep velocity structures. The flow chart of the thesis is given in Figure 1.10.

Chapter 1. Background information of this study was presented. General tectonic setting and seismicity of the Marmara Region were given. Previous studies on the topics of this study were summarized. Finally, the objectives of the thesis are given in this chapter.

Chapter 2. A detailed investigation of 1D S-wave soil velocity structures in Tekirdag city center and its districts Muratli, Corlu, Marmara Ereglisi and at locations of AFAD strong motion station sites were performed using microtremor array measurements. Phase velocities curves of Rayleigh waves were estimated in a frequency range from 1 to 30 Hz from vertical components of microtremor array records using the SPAC method. The observed phase velocities were used for an estimation of 1D S-wave velocity structure profiles of shallow soils. The Genetic Algorithm and Simulated Annealing (GASA) that is a hybrid heuristic inversion method was used to find an optimal S-wave velocity model. The results of the microtremor observation were discussed, and the relationships of average S-wave velocities of the upper 30 m (AVs30) with slope and site amplification were also determined.

Chapter 3. 1D deep velocity structures at different azimuths were determined using surface wave group velocity dispersion curve analyses for the ground motion of the 2014 Gokceada earthquake. The velocity waveforms of the 2014 Gokceada earthquake were obtained from an integration of the acceleration records in the frequency domain after applying a baseline correction were analyzed with multiple filter method. The observed dispersion curves at frequencies between 0.07 and 0.80 Hz were used to extract the dispersive feature of the 1D velocity structures. The defined initial models were modified in a try-and-error procedure to get sufficient fitting of the theoretical group velocity to the observed one.

Chapter 4. The 2014 Gokceada earthquake velocity seismograms at the AFAD strong ground motion stations was simulated to validate the deep and shallow soil layers revealed in Chapters 2 and 3. A source model of the main shock was constructed from the previous results. Then, the broadband ground motions were calculated at the engineering bedrock using 1D simulation based on Discrete Wave Number Method (DWNM). The shallow-layers' amplifications were included to obtain the surface motion.

Chapter 5. The 1912 Murefte earthquake ground motions were simulated using the validated 1D velocity structure. The two and three asperity source models were tested to find out a proper source model for the mainshock. The PGV values of the synthetics at the seven AFAD stations were used to calculate intensities. The calculated intensities were compared with the observations to decide the best source model. Finally, strong ground motions were estimated in serious-damaged near-fault area.

Chapter 6. For conclusion and future tasks.

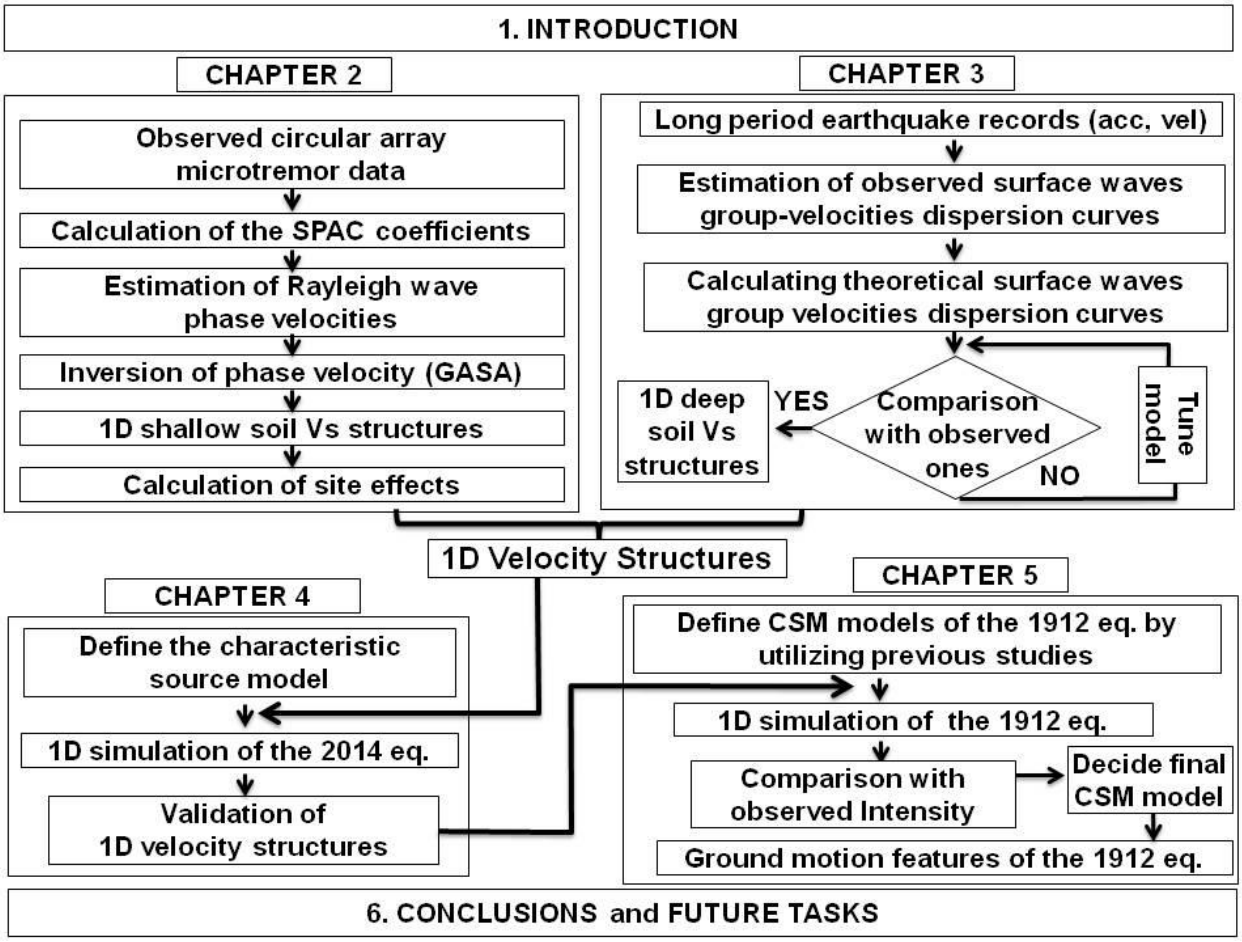

Figure 1.10 Flow chart of the thesis.

Chapter 2

Exploration of Shallow S-Wave Velocity Structure by Using Microtremor Array Measurements

2.1 Overview of Microtremor Measurements Methods

The subsurface velocity structures especially sedimentary layer overlaying on the engineering bedrock or seismic bedrock can be estimated using several methods to find out Vs profiles. The direct methods such as drilling and well logging require geophysical or laboratory testing that impose significant cost and time. However, there are simple, economical and rapid indirect methods to evaluate Vs profiles, like spectral ratios of horizontal-to-vertical components (H/V) and microtremor array data analyses. Microtremor observations have become very popular in the last several decades because they are cost effective and do not need a source to generate a signal. Therefore, it is easy to collect data for site characterization (e.g. Okada 2003, Kudo et al. 2002; Ozel et al. 2004; Zor et al. 2010; Grutas and Yamanaka 2012; Zaineh et al. 2012; Asten et al. 2014; Ozmen et al. 2016; Pramatadie et al. 2016). On the other hand, the method has naturally a few disadvantages such as limited frequency range, a trade-off between Vs and thickness of layers, and assumptions of 1D homogeneous and isotropic horizontal layer model.

Microtremors contain many surface waves. These surface waves are generated randomly by a variety of natural and human-made sources such as traffic, factories, sea waves, atmospheric pressure, natural activities, human activities, and natural ground vibrations, and travel through in geological structures. Microtremors are complex elastic waves and contain not only body and surface waves but also scattered and diffracted waves. There are two array methods to survey microtremor measurements (Figure 2.1). One of them is frequency-wavenumber (f-k) spectral method and the other one is SPAC method. Both approaches are based on theories to detect signals from noise to estimate subsurface velocity structure. For this reason, microtremor survey methods are also an application of the stochastic process. The f-k method uses several sensors without specific array geometry and allows identifying higher modes of surface waves. The SPAC method that requires a circular array combined with a data analysis method is used for understanding the transmission properties of a variety of waves generated by earthquake movement. The theory of the method was developed by Aki (1957). He estimated subsurface structure from microtremor records by assuming that the microtremors are isotropic waves coming from all directions.

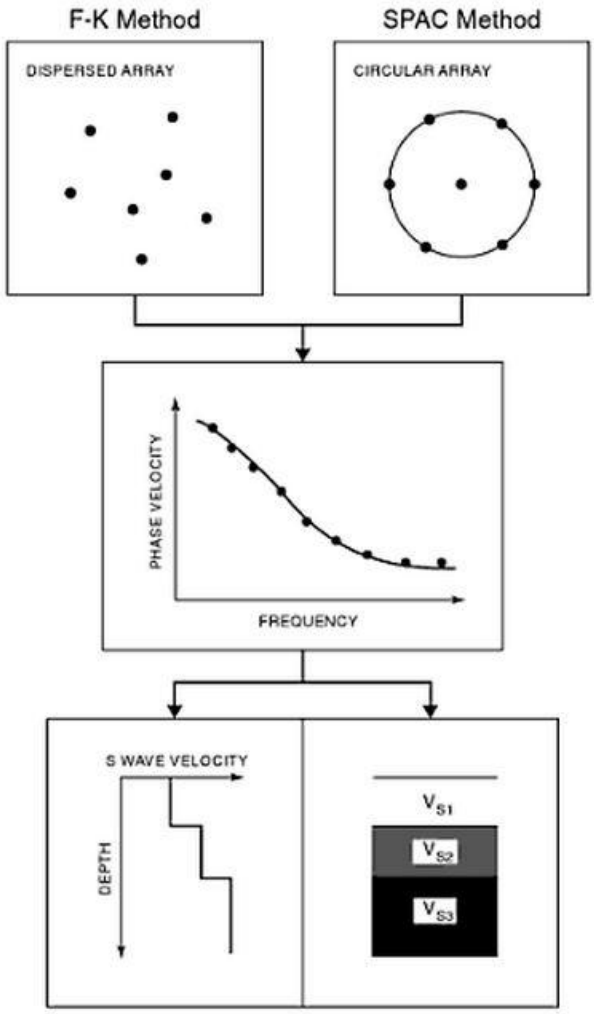

Figure 2.1 Microtremor array measurements methods and their basic procedure (Okada, 2003).

2.2 Geological Settings of Tekirdag

A detailed geology map of Tekirdag is given in Figure 2.2 (Tekirdag Municipality, 2006). Tekirdag city is located in the southern part of the Thrace Basin. The study area is generally covered by Oligocene – Lower Miocene continental clastic rocks (siltstone, claystone, sandstone). There are also wide artificial landfill areas beneath the Tekirdag city center. The coastline between Tekirdag and Marmara Ereglisi consists of Middle – Upper Oligocene aged claystone, sandstone and siltstone units of the Danisment Formation (Figure 2.2). The elevation of topography increases from the coastline to the north as high as 200 m. The younger units are visible at higher elevations. There are also several N-S oriented creek beds filled with Quaternary soil. The alluvial bed of Cevizli Creek is the largest in the west of the city. Landfills were located

in the city center of Tekirdag. The coastline is also covered with artificially filled areas to enlarge the main road and city park. The downtown of the city (around the site T04 in Figure 2.2) is covered by old city landfill on the claystone units.

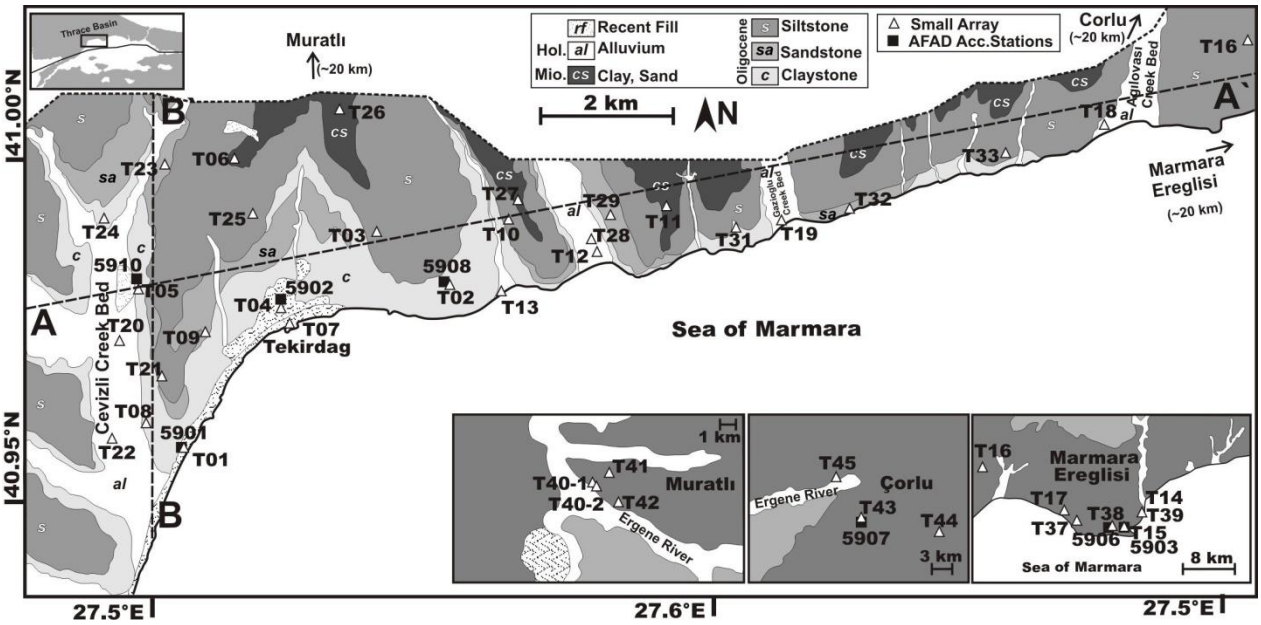

Figure2.2 Detailed geology map of Tekirdag redrawn from the 1:12,000-scaled map of Tekirdag Municipality (2006), Muratli, Corlu and Marmara Ereglisi regions are redrawn from MTA (2003) web page http://www.mta.gov.tr/v2.0/daire-baskanliklari/jed/index.php?id=500bas) 1:500,000 Istanbul Geology Map. White triangles are small array observation sites; black squares are AFAD strong motion stations.

The microtremor array sites were deployed on different geological units as shown in Figure 2.2. T02, T08, T24, T31 were located on claystone, T09, T23, T29, T32 on the sandstone and T21, T25,T03, T10, T33 on the silt stone unit. There are also 3 sites (T04, T07, T01) on the landfill, 4 sites on the clay-sand stone (T06, T11, T26, T27) and 8 sites located on the alluvial units (T05, T20, T22, T13, T12, T28, T19, T18).

There is no detailed geology map for the other three districts of Tekirdag: Muratli, Corlu, Marmara Ereglisi and the six sites that are located close to the AFAD station (Gelibolu, Enez, Gokceada and Canakkale city center). These areas consist of similar continental clastic rocks mainly in Miocene age according to information in the 1:500,000 large scaled geology map of

Turkey from the General Directorate of Mineral Research and Exploration (MTA 2003) web page (Figure 2.2). This geological unit contains 14 microtremor array sites in Tekirdag (e.g. T14, T39, T44, and T41). Muratli and Corlu lie near the Ergene River, which is one of the largest river in Thrace Basin. There are only seven sites in the northern part and 2 sites (Gazikoy, Sarkoy) in the southern part of the Tekrdag city center.

2.3 Array Measurements of Microtremors

The field studies were performed to collect microtremors data in October 2013 and September 2014 under the joint project "Earthquake and Tsunami Disaster Mitigation in the Marmara Region and Disaster Education in Turkey (MarDiM)" between Japan and Turkey in the framework of Science and Technology Research Partnership (SATREPS) (Figure 2.3).

The array measurements were carried out at totally 44 locations in Tekirdag city center, and three districts of Tekirdag: Marmara Ereglisi, Muratli, Corlu (Figure 2.3-top). There were two sites, T46 and T47, located at Gazikoy and Sarkoy (SW Tekirdag), respectively in Figure 2.3-bottom. The results of these two sites that were located ~30 km and ~50 km far from the city center were not used during the interpretations of results, statistical and geological analysis. The locations of the sites with obtained site parameters in this study are given in Table 2.1.

The sites were deployed away from roads with high-traffic, factories, main bus stations and other man-made temporary noise sources in order to record accurate data. We chose strong motion station locations of the AFAD, schools, parks, governmental or private lands for easy deployment of the circular arrays in Tekirdag, Muratli, Corlu and Marmara Ereglisi (Figure 2.3-top). We also applied array measurements at six AFAD stations in Gelibolu, Enez, Gokceada and Canakkale city center shown in Figure 2.3-bottom. The array sites were located very close to the stations. The distance between the center of the array and station were less than 50 m at all AFAD station sites. The array sizes were designed according to available open space near the stations.

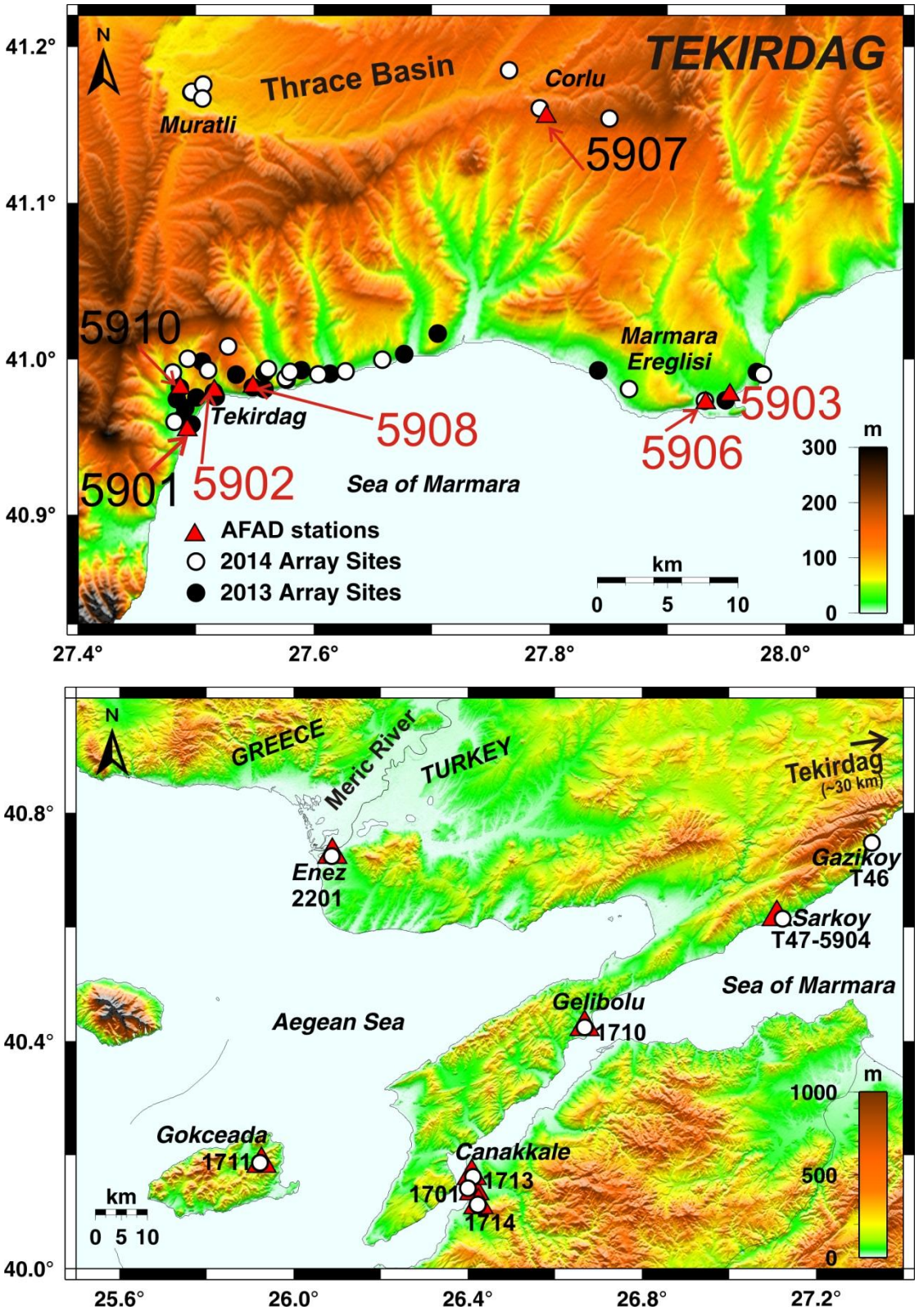

Figure 2.3 Top: Array site locations in Tekirdag city center, Muratli, Corlu and Marmara Ereglisi. Bottom: Sites in Gazikoy, Sarkoy, Enez, Gelibolu, Canakkale city center. The white and black circles show the array sites. Red triangles show the location of AFAD stations. 5901 and 5903 are the removed stations.

The SPAC method, in practice, requires a circular array consisting of three or more circumferential stations and one at the center (Okada 2003, 2006) in Figure 2.1. At least, three sensors located at the edges of the equilateral triangle inscribed in a circle and one sensor at the center are sufficient for SPAC applications to provide phase velocities (Kudo et al. 2002).For this reason, the double equilateral triangular array configuration was used at each site. We temporally deployed six vertical accelerometers at the edges of the two equilateral triangles with different side lengths inscribed in large and small circles; one vertical and one two-component horizontal accelerometer sensors were deployed at the center of the array configuration to obtain simultaneous microtremors records (Figure 2.4a, b). The vertical V243S accelerometers with a flat characteristic frequency range of 0.20 and 30 Hz provided by Mitutoyo Corporation were used in each array (Figure 2.4c). The data were recorded with 24-bit analogue-to-digital (A/D) wireless data loggers Su100 with 100 samples per second manufactured by Hakusan Corporation (Figure 2.4c). The maximum and minimum lengths of the sides of equilateral triangles were 48 m and 1.5 m, respectively as given in Table 2.1. The array size was controlled by the availability of open space at the each site. The maximum array size possible was 48 meter because of the wireless LAN data transmission limitation. The record lengths of the microtremors were at least 15 or 20 minutes for each array (Figure 2.4d).

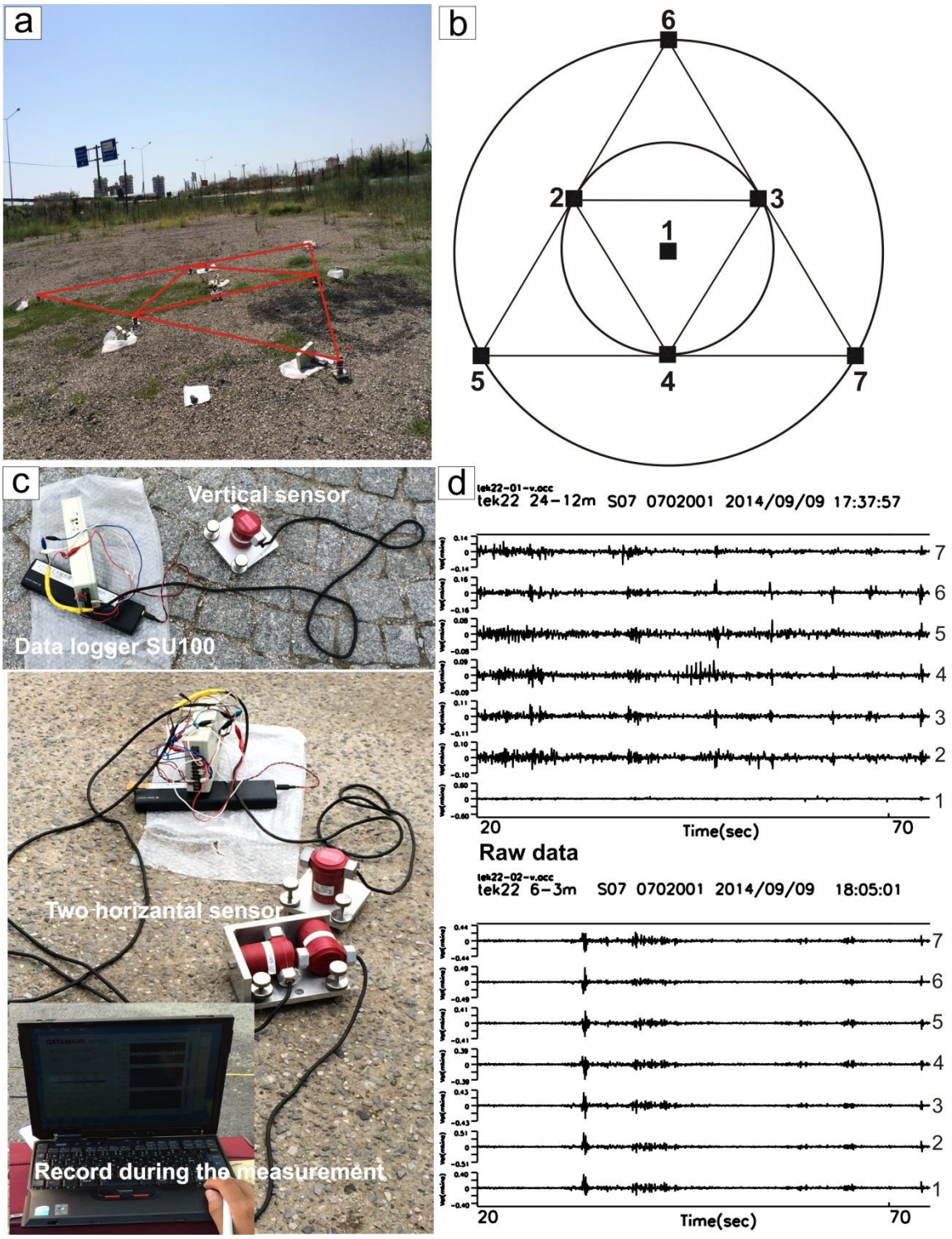

Figure 2.4 a) Example of vertical configuration at T22 (24-12, 6-3 m). b) Circular double triangular array configuration. Numbers show location of accelerometers.c) Vertical, horizontal sensors with data loggers d) Example of simultaneously seven vertical acceleration records of both arrays at site T22.

Table 2.1 Array Site Location Name, AFAD Station Code, Latitude, Longitude, Elevation, Average slope, Surface geology index (GI), Array sizes of microtremor measurements, AVs30 values, NEHRP site class. The average site amplification for a frequency range 0.4 to 10 Hz and fundamental site predominant frequency (Hz) obtained from the theoretical amplification factors. Thickness of layer above the engineering bedrock obtained for 29 sites in Tekirdag. Geology index (GI): al: Alluvium, c: Claystone, sa: Sandstone, s: Siltstone, cs: Clay, Sand rf: Recent Fill, lm: Limestone cr: Continental Clastic Rocks units.

Array Site Location Name	AFAD Station Code	Latitude (°N)	Longitude (°E)	Elev. (m)	Average Slope	GI	Sizes[A] (m)	AVs30 (m/s)	NEHRP Site Class	Average Ampl. (0.4-10 Hz)	Predominant Freq (Hz)	Thickness of layer above the Engineering Bedrock (m)
T01	5901*	40.95818	27.49630	1	0.047	rf	16-8, 4-2	349 (472)[B]	D	3.1	3.6	O (15.2)
T02	5908	40.98201	27.54817	65	0.05	c	16-8, 4-2	334	D	3.1	3.5	O (19.8)
T03		40.99014	27.53412	148	0.005	s	24-12, 6-3	359	C	3.0	9.5	O (17.7)
T04	5902	40.97891	27.51511	30	0.072	rf	20-10, 5-2.5	458 (409)[B]	C	2.6	13.5	O (38.9)
T05	5910	40.98146	27.48625	42	0.04	al	20-10, 5-2.5	427	C	3.1	9.5	O (15.6)
T06		40.99851	27.50511	160	0.052	cs	20-10, 5-2.5	380	C	3.1	11.0	O (13.3)
T07		40.97585	27.51673	3	0.039	rf	16-8, 4-2	326	D	3.4	8.3	X (assumed 15)
T08		40.96151	27.48737	17	0.082	c	20-10, 5-2.5	414	C	2.7	12.6	X (assumed 10)
T09		40.97543	27.50028	52	0.088	sa	20-10, 5-2.5	413	C	2.8	9.2	O (27.1)
T10		40.99137	27.55834	38	0.047	s	20-10, 5-2.5	311	D	3.4	5.9	O (27.0)
T11		40.99297	27.58932	66	0.068	cs	16-8, 4-2	298	D	3.3	3.2	X (assumed 20)
T12		40.98678	27.57682	4	0.015	al	20-10, 5-2.5	334	D	3.5	4.8	O (17.0)
T13		40.98077	27.55812	8	0.068	al	20-10, 5-2.5	325	D	3.4	5.3	O (40.9)
T14		40.99173	27.97571	25	0.045	cr	20-10, 5-2.5	472	C	2.7	14.5	O (15.1)
T15	5903*	40.97365	27.94926	5	0.019	cr	16-8, 4-2	423 (325)[B]	C	3.0	6.1	O (9.3)
T16		41.01641	27.70498	67	0.034	cr	24-12, 6-3	532	C	2.5	13.5	X (assumed 15.6)
T17		40.99273	27.84108	2	0.017	cr	24-12, 6-3	548	C	2.5	7.8	O (10.6)
T18		41.00319	27.67659	1	0.025	al	20-10, 5-2.5	375	C	3.1	9.9	O (27.9)
T19		40.99074	27.61347	2	0.021	al	20-10, 5-2.5	171	E	3.7	1.6	X (assumed 20)
T20		40.97435	27.48372	21	0.015	al	20-10, 5-2.5	246	D	3.5	2.3	O (18.1)
T21		40.96864	27.49088	50	0.11	s	16-8, 4-2	436	C	2.9	8.6	O (42.7)
T22		40.95984	27.48182	11	0.018	al	24-12, 6-3	142	E	3.6	1.0	X (assumed 25)
T23		41.00021	27.4931	64	0.098	sa	24-12, 6-3	428	C	2.9	8.6	O (24.8)
T24		40.99142	27.48049	46	0.085	c	20-10, 5-2.5	531	C	2.5	9.5	O (36.9)
T25		40.99289	27.51033	125	0.123	s	24-12, 6-3	492	C	2.7	6.1	O (20.2)
T26		41.00811	27.52728	158	0.041	cs	32-16, 8-4	478	C	2.8	14.5	O (12.0)
T27		40.99369	27.56093	60	0.046	cs	20-10, 5-2.5	502	C	2.6	13.5	O (14.1)
T28		40.98784	27.57605	5	0.023	al	24-12, 6-3	232	D	3.8	2.4	X (assumed 15)
T29		40.99193	27.57971	19	0.053	sa	24-12, 6-3	407	C	3.1	7.0	O (46.4)

Table 2.1 continue

T31		40.99018	27.60365	31	0.039	c	24-12, 6-3	408	C	3.0	6.8	O (38.2)
T32		40.99212	27.62683	11	0.112	sa	32-16, 8-4	579	C	2.3	5.3	O (25.0)
T33		40.99960	27.65805	13	0.028	s	24-12, 6-3	506	C	3.2	5.5	O (14.7)
T37		40.98072	27.86725	12	0.018	cr	20-10, 5-2.5	519	C	2.6	7.5	O (55.0)
T38	5906	40.97327	27.93165	2	0.013	cr	24-12, 6-3	240	D	3.6	2.0	X (assumed 13)
T39		40.99020	27.98078	27	0.261	cr	20-10, 5-2.5	779	B	2.0	15.5	O (13.6)
T40-1		41.17132	27.49647	82	0.011	cr	16-8, 4-2	366	C	3.1	6.8	X (assumed 20)
T40-2		41.17100	27.49605	82	0.011	cr	24-12, 6-3	490	C	3.0	10.2	X (assumed 15)
T41		41.17580	27.50609	91	0.014	cr	24-12, 6-3	392	C	3.0	4.6	X (assumed 25)
T42		41.16692	27.50545	83	0.009	cr	20-10, 5-2.5	349	D	3.3	5.3	O (54.7)
T43	5907	41.16063	27.79163	163	0.034	cr	20-10, 5-2.5	542	C	3.0	11.7	O (13.3)
T44		41.15412	27.85065	194	0.024	cr	24-12, 6-3	449	C	2.8	5.1	X (assumed 5)
T45		41.18496	27.765558	125	0.031	cr	20-10, 5-2.5	477	C	2.9	10.2	X (assumed 5)
T46		40.74766	27.32757	30	0.208	cr	16-8, 4-2	580	C	2.7	8.6	X (assumed 104.2**)
T47	5904	40.61610	27.12281	11	0.012	cr	12-6, 3-1.5	222 (225)[B]	D	3.4	1.4	X (assumed 10)
Cnk01	1710	40.42435	26.66695	40	0.020	cr	48-24, 12-6, 3-1.5	304 (286)[B]	D	3.4	6.3	O (78.9)
Enez01	2201	40.72416	26.08729	15	0.088	al	24-12, 6-3	321	D	3.1	1.3	X (assumed 25)
Gada01	1711	40.19095	25.90777	81	0.109	cr	24-12, 6-3	335	D	3.0	9.2	X (assumed 20)
Cnk02	1714	40.11344	26.42187	128	0.152	cr	24-12, 6-3	390	C	3.2	5.5	X (assumed 20)
Cnk03	1701	40.14154	26.39978	1	0.041	al	28-14, 7-3.5	195 (192)[B]	D	3.8	0.85	X (assumed 25)
Cnk04	1713	40.16179	26.41186	53	0.035	lm	32-16, 8-4	524	C	2.7	10.6	O (12.0)
MRFT		40.66780	27.244810	11	0.00015	cr	20-10;5-2.5	295	D	3.0	2.6	X (assumed 50)

[A] Length of the triangles.

[B] AVs30 in parentheses by AFAD from Multichannel Analysis of Surface Waves (MASW) analyses.

***** Removed AFAD stations.

****** The assumed thickness of the layer above the engineering bedrock according to Marsite (New Directions in Seismic Hazard Assessment through Focused Earth Observation in the Marmara Supersite) Periodic Report of WP4 at T46-Gazikoy

O: The thickness calculated from hybrid inversion method

X: Engineering bedrock velocity is not available. The assumed thicknesses were given in the parentheses.

2.4 Estimation of Phase Velocities

Phase velocities curves of Rayleigh waves were estimated in frequency range from 1 to 30 Hz from vertical components of microtremor array records using the SPAC method proposed by Okada (2003). The SPAC method computes cross-correlations between station pairs in the array with the SPAC coefficients for calculation of phase velocity at different frequencies. Each vertical-component record was divided into 81.92 s time segments. Then, the transient and artificial noises generated by local conditions such as pedestrians and cars near the sensors during the measurements were removed. The Parzen window with a band width of 0.2 Hz was chosen for smoothing in the data processing except T39. The bandwidth was 0.8 Hz for the site T39. We used the 6-14 segments (average 10) for averaging to get the phase velocity at each frequency. SPAC coefficients were obtained from all the segments for analysis and were averaged to get the phase velocities at the each frequency. Phase velocities of Rayleigh waves can be calculated by using SPAC covariance function $(\rho(r,\omega))$ between the center and one point on the circumference of the circular array at the angular frequency (ω) calculated for a distance r. The spatial covariance function can be defined by averaged over all azimuthal directions (θ). Assuming stationary of microtremors, Aki (1957) showed that

$$\rho(r,\omega) = \frac{1}{2\pi\phi(r=0,\omega)} \int_0^{2\pi} \phi(r,\theta,\omega)\, d\theta \qquad (1)$$

where $\phi(r=0,\omega)$ is an average autocorrelation function at a center of array, $\phi(r,\theta,\omega)$ is the cross-correlation function between the records obtained coordinates (r, θ) and the record obtained at the circle. Equation (1) can be generalized after the integration along θ with Bessel function (J_0) of first kind and the order zero and normalization, obtained

$$\rho(r,\omega) = J_0\left(\frac{r(\omega)}{c(\omega)}\right) \qquad (2)$$

where is $c(\omega)$ is the phase velocity at frequency (ω) at the site.

Equation 2 is called SPAC coefficient at the angular frequency (ω) as the power of spectra of microtremors at one station within array space (the circle center, i.e., origin) (Okada, 2003). The simple SPAC coefficient $\rho(f,r)$ from various combinations of station distances (r) as a function

of frequency *(f)* is related to phase velocity *c(f)* via the Bessel function of the first kind of zero order in Equation3.

$$\rho(f,r) = J_0(2\pi fr / c(f)) \qquad (3)$$

In Equation 3, *c(f)* is velocity of a certain frequency can be calculated SPAC coefficient of the microtremor wave that is recorded with a circular array.

Figure 2.5a shows an example of the SPAC coefficients obtained from the microtremor data recorded at site T22. Depending on the array configuration, the five SPAC coefficients corresponding to the five sensor pair distances were calculated. The calculated SPAC coefficients are high enough at a frequency up to 1.5 Hz (Figure 2.5a). Different distances between the sensor pair help us to get phase velocity information from different frequency ranges. While the low frequency information is from the SPAC coefficients of large distance (24 m), high frequency information can be observed from the small distance (6.92 m). Therefore, it is possible to obtain phase velocity corresponding to different depths (Figure 2.5b). Further details of the SPAC method can be found in the literature (e.g., Okada et al., 1987, 1989, 2003; Asten, 2001; Kudo et al., 2002; Morikawa et al., 2004; Chavez-Garcia et al. 2005). The observed phase velocity dispersion curves were obtained by choosing dispersion points by eye at each frequency (Figure 2.5b).

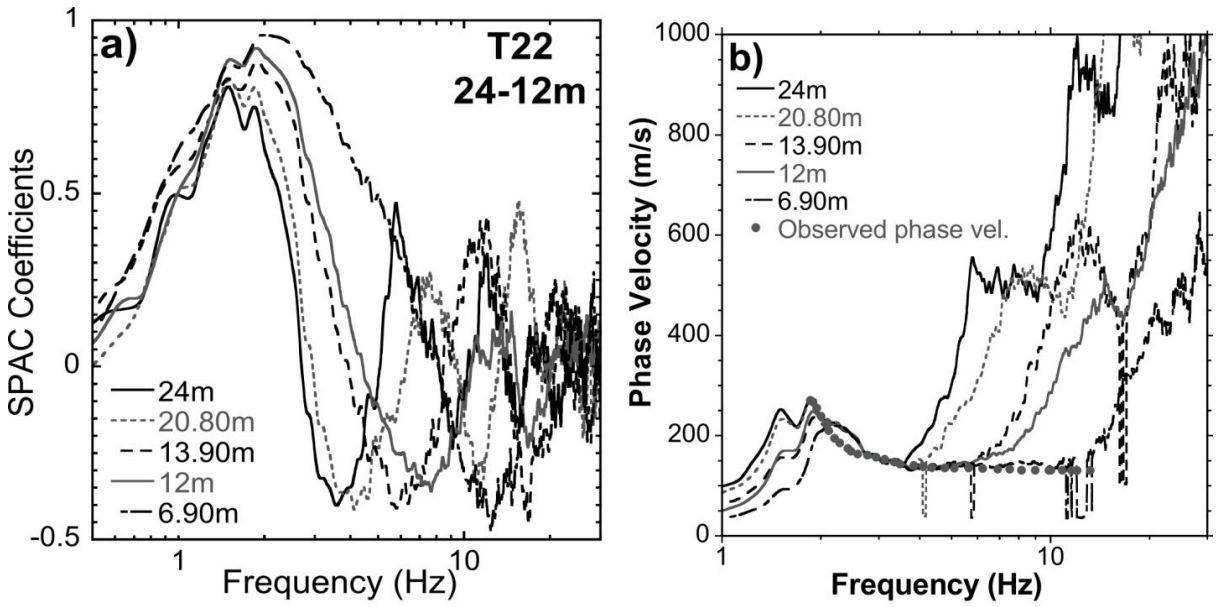

Figure 2.5 a) Example of the SPAC coefficients as a function of frequency for different station distances at the site T22.The maximum side length is 24 m. b) The calculated phase velocities for each distance.

The observed Rayleigh wave phase velocities categorizing is important to understand the similarities and differences between the sites. The observed phase velocities dispersion curves were classified at the sites according to the geological units in Figure 2.2. The eight *groups (a-h)* are shown in Figure 2.6. *Group a* contained sites located on the alluvial areas. Sites T22 and T19 had low phase velocities (~400 m/s) at lower frequencies that represent deep parts of the sediment layer. The dispersion curve of T05 was very steep with respect to the other sites and the highest velocity (~625 m/s) at low frequencies was observed there. *Group a* showed wide frequency ranges of the phase velocities (2-30 Hz). T22, T20 and T05 were on the alluvial bed of the Cevizli Creek in Tekirdag city, and it can be clearly seen that their dispersion curves showed steep variations with increasing frequency, suggesting the variation in thickness of the alluvial bed from the coast (T22) to the upriver (T05) (see Figure 2.2). There are several small alluvial creek beds in the east of Tekirdag. The dispersion curves of T12, T13, T18, T19 and T28 changed due to the differing thickness of the alluvial sediments. The lowest velocity was ~90 m/s (T18) and the velocities increase up to 625 m/s at lower frequencies at these sites.

The three sites in *group b* in the area covered by landfill had phase velocities between 165 m/s and 600 m/s. The frequency band was narrow (6-30 Hz). The dispersion curve of T04 was steep at high frequencies because the site was located on a hillside. The others were on the landfill along the coastline of Tekirdag city center (see Figure 2.2).

Group c represents the phase velocities at the sites deployed on claystone. The phase velocities were between 230 and 700 m/s in frequency ranges larger than 5 Hz. T02, T08, T31 had similar phase velocities at high frequency. T02 and T31 had the same velocities at low frequencies, while T08 located on the border of alluvium unit, had lower phase velocity. T24 had high velocities at all frequencies because it was located on a hill while the other sites in the *group* were located on a lowland area.

The sites measured on sandstone were designated *group d*. Their observed phase velocities ranged from 225 m/s to 750 m/s at frequencies between 2.5 Hz and 30 Hz. The three sites had consistent dispersion curves except T32. The T32 site showed a very high phase velocity (>500 m/s) at high frequencies.

The sites in *groups e* and *f* were deployed on Oligocene siltstone and Miocene clay-sandstone units, respectively. The dispersive features of both *groups* were similar, with phase velocities between 180 m/s and 750 m/s on average. The geological unit of *group f* is younger than *group e,* with the former located in the northern part of the city center. T03 and T25, with higher velocities at high frequencies, were located at a high elevation (~150 m) with respect to the other sites in *group e*. In *group f*, T27 had a high phase velocity at high frequency like T25.

There were four and three observation sites in Muratli and Corlu towns, respectively, in *group g*. The phase velocities were between 210 m/s and 630 m/s at frequencies between 3 Hz and 30 Hz. Both towns are located in a flat area and there is no significant elevation difference in Muratli. T44 was located at the highest elevation (~200 m) among the other sites in Corlu. It had a high velocity at a high frequency. On the other hand, the Ergene River, which built Quaternary alluvial beds, cuts both towns (see Figure 2.2). The similar dispersion curves may reflect the similar geological and geomorphologic structures.

There were six sites in Marmara Ereglisi (*group h*). The observed phase velocities showed a wide variation from 160 m/s to 850 m/s at frequencies between 4 and 30 Hz. Site T39 showed a very high velocity (650-900 m/s). The dispersion curve of T38 was very similar to those sites located on alluvial areas.

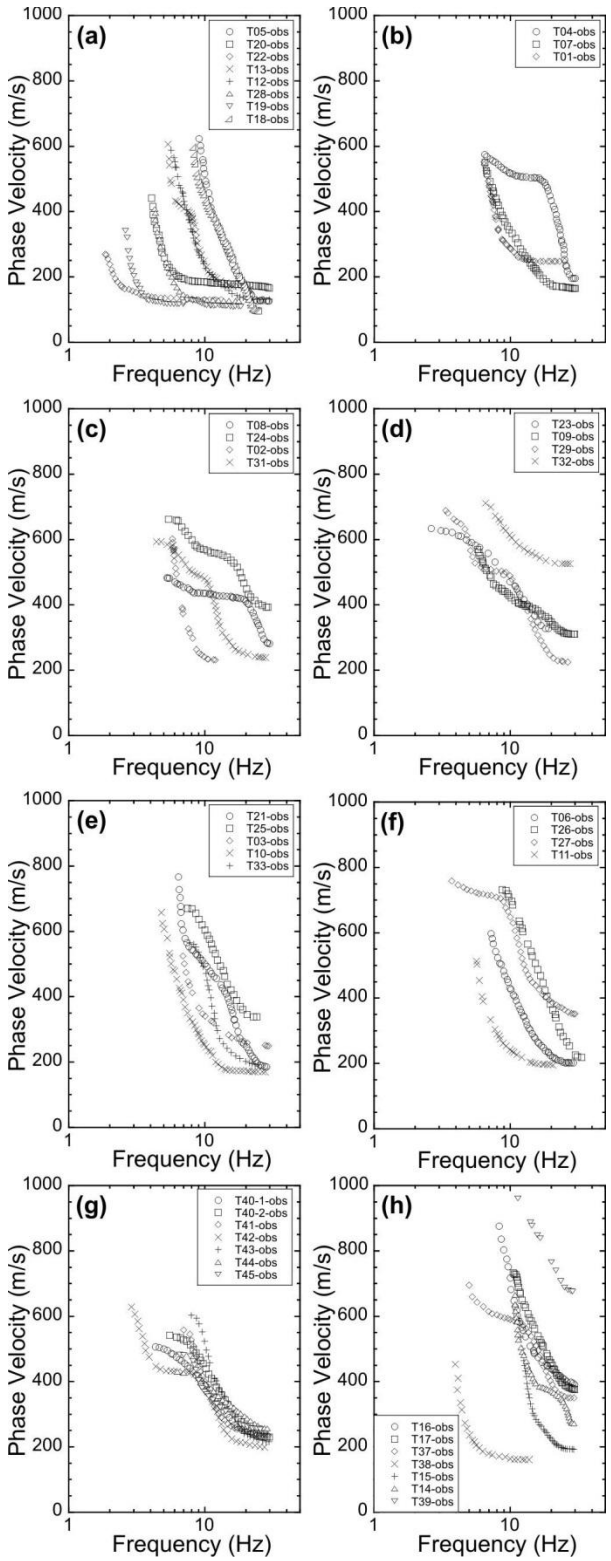

Figure 2.6 Observed Rayleigh wave phase velocities dispersion curves of 42 sites in Tekirdag obtained by the SPAC method. The sites are grouped according to their geological units in Figure 2.2: a) alluvial; b) resent landfill; c) claystone; d) sandstone; e) siltstone; f) clay-sand stone, continental clastic rocks, carbonates Muratli, Corlu (g) and Marmara Ereglisi (h).

2.5 Inversion of Phase Velocities

The observed phase velocities were used for an estimation of 1D S-wave velocity structure profiles. The Genetic Algorithm and Simulated Annealing (GASA) that is a hybrid heuristic inversion method introduced by Yamanaka (2007) as a global optimizing method was used to find an optimal S-wave velocity model. This method searches a 1D soil profile by minimizing the misfit function that is defined as a sum of squared differences between the observed and calculated phase velocities. The misfit function, *E,* can be expressed by

$$E_i = \frac{1}{N}\sum_{i=1}^{N}\left[v_i^o - v_i^c\right]^2$$

where v_i^o and v_i^c are the observed and calculated phase velocities of the Rayleigh wave respectively, and *N* is the number of data. The method used for theoretical dispersion curves of the fundamental mode of Rayleigh waves is based on Haskell (1953). A horizontally layered, isotropic and homogenous model was assumed. The layer model is characterized by four parameters; thickness *(h),* density *(ρ),* P-wave velocity *(Vp)* and S-wave velocity *(Vs)* for each layer. Thicknesses and shear-wave velocities are the unknown parameters in the inversion. The density values were given as 1.7, 1.9 and 2.1 gr/cm^3 for the layer model. P-wave velocity is not inverted but derived from S-wave velocity by using the empirical relation by Kitsunezaki et al. (1990), defined as

$$\mathrm{Vp} = 1.29 + 1.11 * \mathrm{Vs}$$

where the units of *Vp* and *Vs* are expressed in km/s.

The two or three-layers models generally were used in the inversion. I applied 50 inversions with 100 generations using different seeds of random number generators, such that a good model with smaller misfit survives to a greater extent in the next generation, while bad models are replaced by newly generated models (Yamanaka and Ishida 1996; Yamanaka 2007). The final model was selected as an acceptable solution if its average misfit was less than 10% (Lomax and Snieder 1994). Appropriate search limits were decided after several trial runs of the inversion algorithm. The narrow search limits were used for some sites for an easy convergence of the misfit. I had difficulties finding common search limits for the observed data at all sites. Table 2.2 shows the

lower and upper search limits of the unknown parameters and an optimal final model for three selected sites as examples. Figure 2.7 shows examples for the comparison between the observed and inverted phase velocities, and Figure 2.8 shows 1D S-wave profiles for each *group* given in Figure 2.6. We found good fits between the observed and calculated velocities for all sites. It is clear that the final models represent the observed data well at most frequencies.

Table 2.2 Example of search limits and optimal final models for the sites T22, T33, T41.

Sites	**Search Limits**		**Final Optimal Model**	
	Vs (m/s)	H(m)	Vs (m/s)	H(m)
T22	100-200	5-50	142	32
	200-500	10-20	349	---
	100-200	5-10	182	6
T33	200-600	10-50	442	15
	600-800	---	708	---
	200-300	6-10	248	7
T41	300-400	10-80	378	12
	500-800	---	665	---

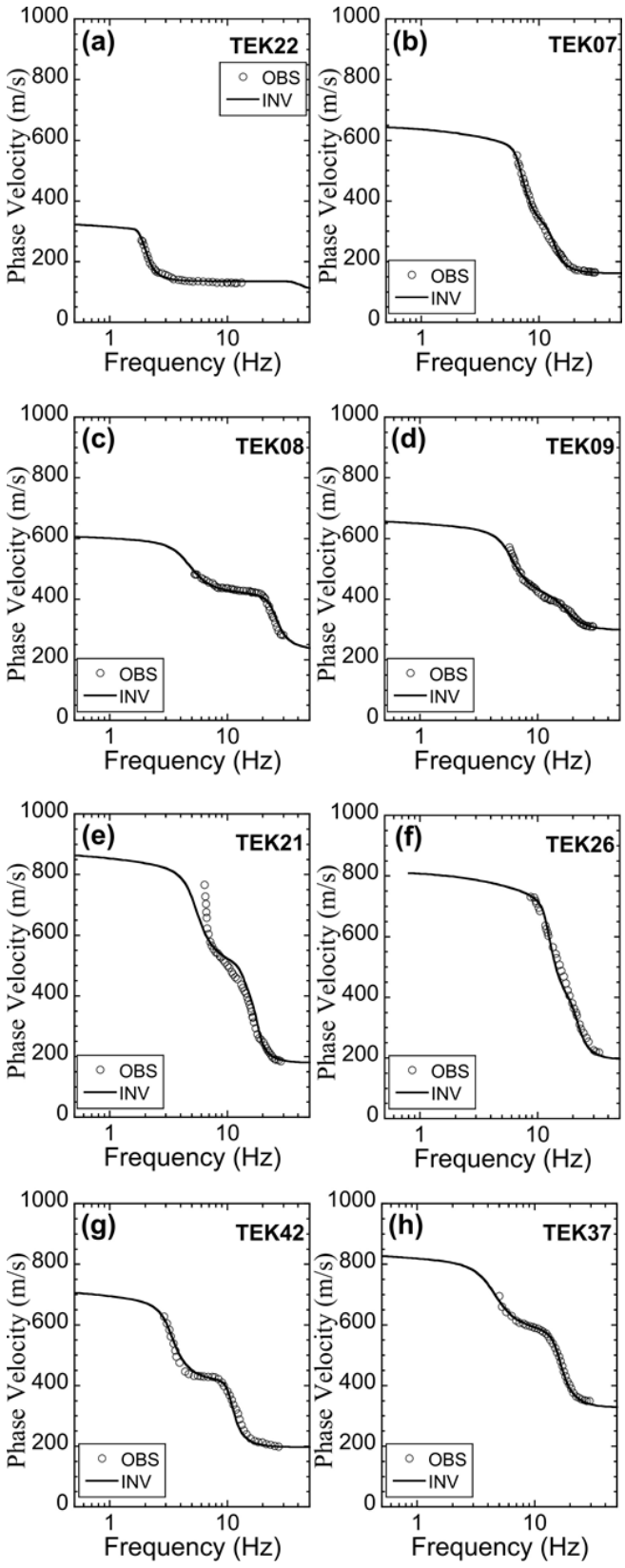

Figure 2.7 Example comparisons between the observed (open circle) and calculated (solid line) phase velocities from each groups given in Figure 2.6.

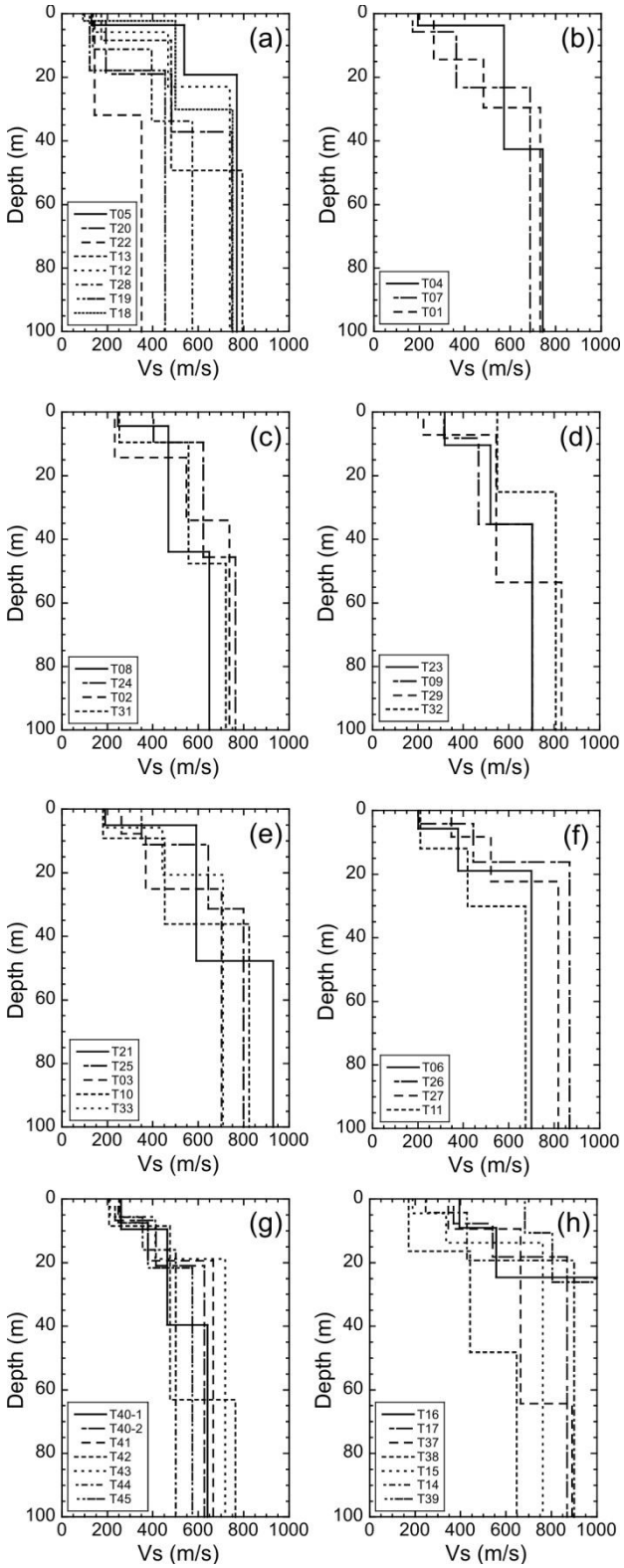

Figure 2.8 Comparison of the Vs profile derived from GASA inversion method for each *group* given in Figure 2.6.

2.6 Results for Tekirdag, Muratlı, Corlu and Marmara Ereglisi

2.6.1 Interpretation of the 1D S-wave Velocity Structure Profiles

The Vs profiles of the sites in *group a* clearly indicate the variation in thickness of the alluvial sediments (Figure 2.8a). The inversion results show that Cevizli Creek (west of Tekirdag city center) has much thick alluvial sediment (Vs=~140 m/s) at its mouth (~30 m) with respect to up river parts (~20 m). The Agilovasi Creek alluvial bed (east of the city center) had the lowest S-wave velocity (T18=90 m/s) in the study area. The sites deployed on other alluvial creek beds showed similar velocities in the top layer (120-140 m/s). The S-wave velocities of the deepest parts beneath the thick sediments are low (350-600 m/s), while the sites on thin sediments have high velocities (~800 m/s) as engineering bedrock (T05,T12,T13,T18).

The uppermost layers of sites in *groups b* to *f* had an S-wave velocity between 200 and 400 m/s. These velocities represent the landfill, claystone, sandstone and siltstone geological units observed on the surface (Figure 2.2). Distinctively, only one site (T32 in *group d*) deployed near the seaside had the highest S-wave velocity (~550 m/s) for its first layer. The S-wave velocity of the engineering bedrock was between 750 and 930 m/s. The engineering bedrock was not revealed at T08 and T11 in *group c* and *f*, respectively.

The Vs profiles in Corlu and Muratli (*group g*) were highly consistent, especially for shallow layers. The S-wave velocity of the first layers was 210 to 260 m/s. Only two sites (T42, T43) showed the engineering bedrock (~740 m/s) in this *group*.

The sites in *group h* in the town of Marmara Ereglisi are located along the coastline (see Figure 2.2). The S-wave velocity of the top layer and the engineering bedrock were 200-370 m/s and 760-900 m/s, respectively. In addition, we estimated the deep structure velocities at two sites at 1050-1200 m/s (T16, T39).

In general, the 1D Vs profiles indicate that the Tekirdag city center and coastal areas have different S-wave shallow structures. The top layers of the sites located on stiff soil had a velocity of ~200 m/s. On the contrary, consistent velocity values were observed in Marmara Ereglisi, Muratli and Corlu towns. The engineering bedrock velocities ranged from 700 m/s to 930 m/s. The sites in Marmara Ereglisi indicated the highest velocity for the deeper structure. On the other

hand, the engineering bedrock beneath the sites in Corlu and Muratli could not be revealed due to the thick upper sediment layers in the Thrace Basin. The depth of the engineering bedrock is 20-50 m in Tekirdag city center and its eastern part, and 10-65 m for Marmara Ereglisi (see Appendix Table A.1)

The inversion results indicate that the S-wave profiles can be grouped with four layers for Tekirdag region (Figure 2.9a-b). 34 sites had the first layer velocity ($90 < Vs < 320$ m/s). The highest velocity of the first layer was ~320 m/s (T09, T23). 33 sites had the second layer with an S-wave velocity of $320 \leq Vs < 500$ m/s. T19, T22 and T32 had only two layers. 25 sites contain the third layer with a Vs velocity from 500 to 700 m/s. 29 sites had the fourth layer with a velocity of $700 \leq Vs < 930$ m/s. T16 and T39 had high velocities for the deep parts which may be interpreted as the fifth layer. The average shear wave velocities of the layers were 210, 415, 600 and 780 m/s from the top to the bottom. The thicknesses of all layers changed from 2 to 55 m as given in Figure 2.9c.

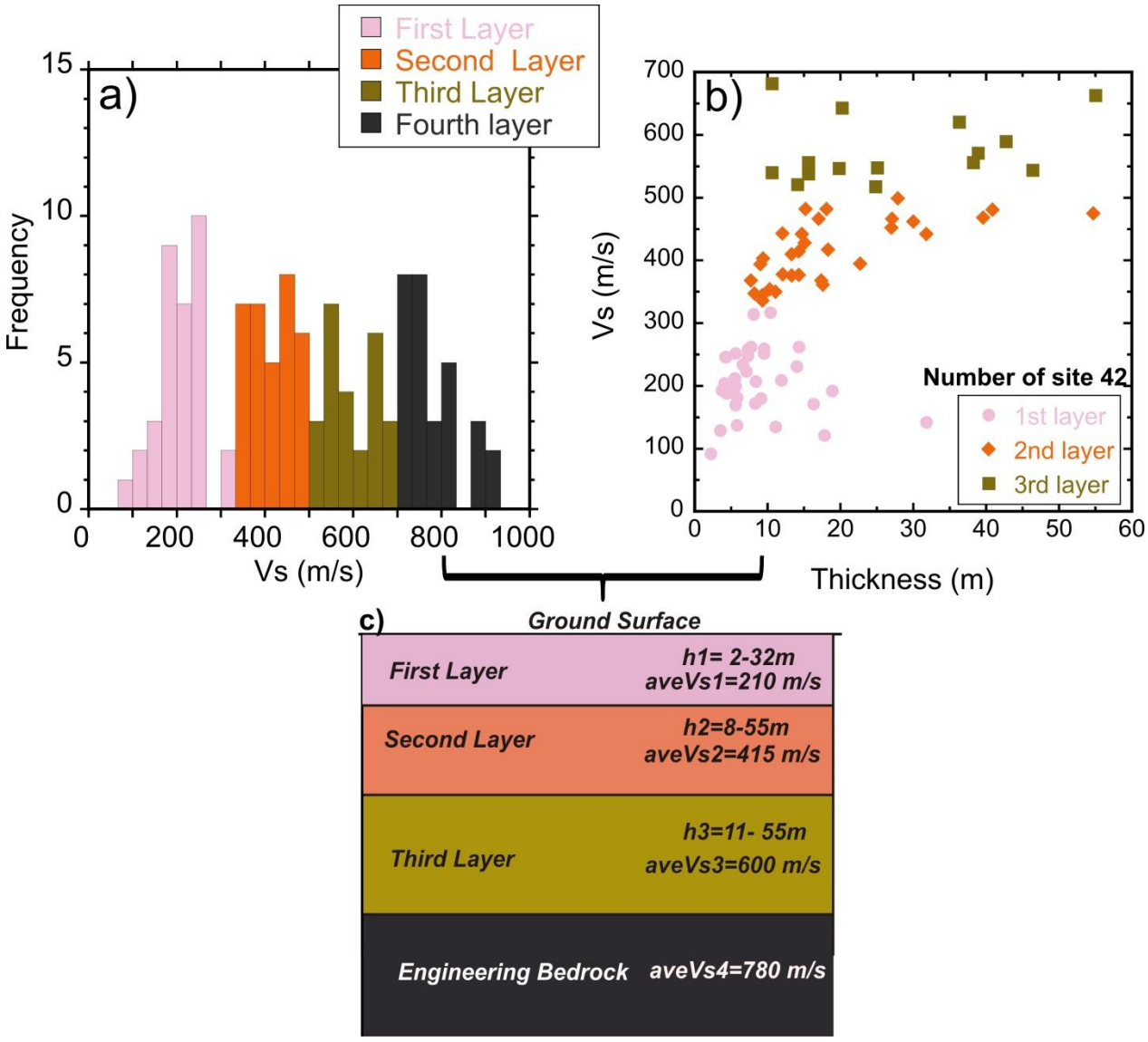

Figure 2.9 a) Histogram distribution of S-wave velocity of the layers b) Thickness and Vs distribution of the first three layers at 42 sites in Tekirdag, Muratli, Corlu and Marmara Ereglisi c) Four layer-model according to average S-wave velocities from the inversion results.

Figure 2.10 shows the velocity cross-section with elevation along the AA' profile in Figure 2.2. The cross section was selected roughly in an east-west direction to identify the velocity variation along the coastline, effects of the topography and alluvial creek beds. Most of the sites had the first layer with low velocities except for T24, T25, T32, and T16. These sites were generally located on lowland areas covered by alluvial sediments (i.e. T20, T19 and T28). The sites on the top of hills had thin or no low velocity layers (i.e. T03, T25). It is clear that the high velocity

layers are dominant at the sites along the eastern coastline of Tekirdag (T32, T33). The engineering bedrock (Vs ~ 780 m/s) cannot be observed in the first 30 m from the surface (T07, T28, T11, T19). We could not determine the velocity in the engineering bedrock at sites on the alluvial basin because of the thick first and second layers. Distinctively, T16 has a high velocity layer at the bottom (Vs >1000 m/s).

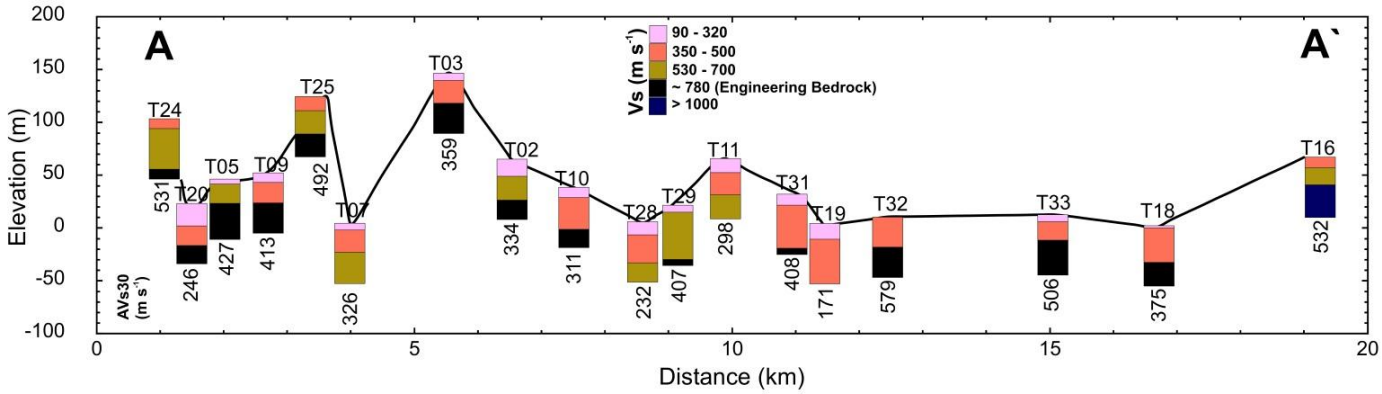

Figure 2.10 The AA' profile in Figure 2.2 parallel to the coastline of Tekirdag, showing inferred shallow subsurface structures. The average S-wave velocities of the upper 30 m are given below the layer structures, to show the variation of the soft sediments from south-west to north-east.

Figure 2.11 shows the velocity cross sections of both A-A´ and B-B´ according to common surface without considering the topography. The sites where the engineering bedrock was observed were plotted for A-A´ profile. The B-B´ profile clearly shows the thickness variation of the Cevizli creek bed in Tekirdag city. It is thick beneath T22 in south and becomes thin at around T20 and T05 in the North.

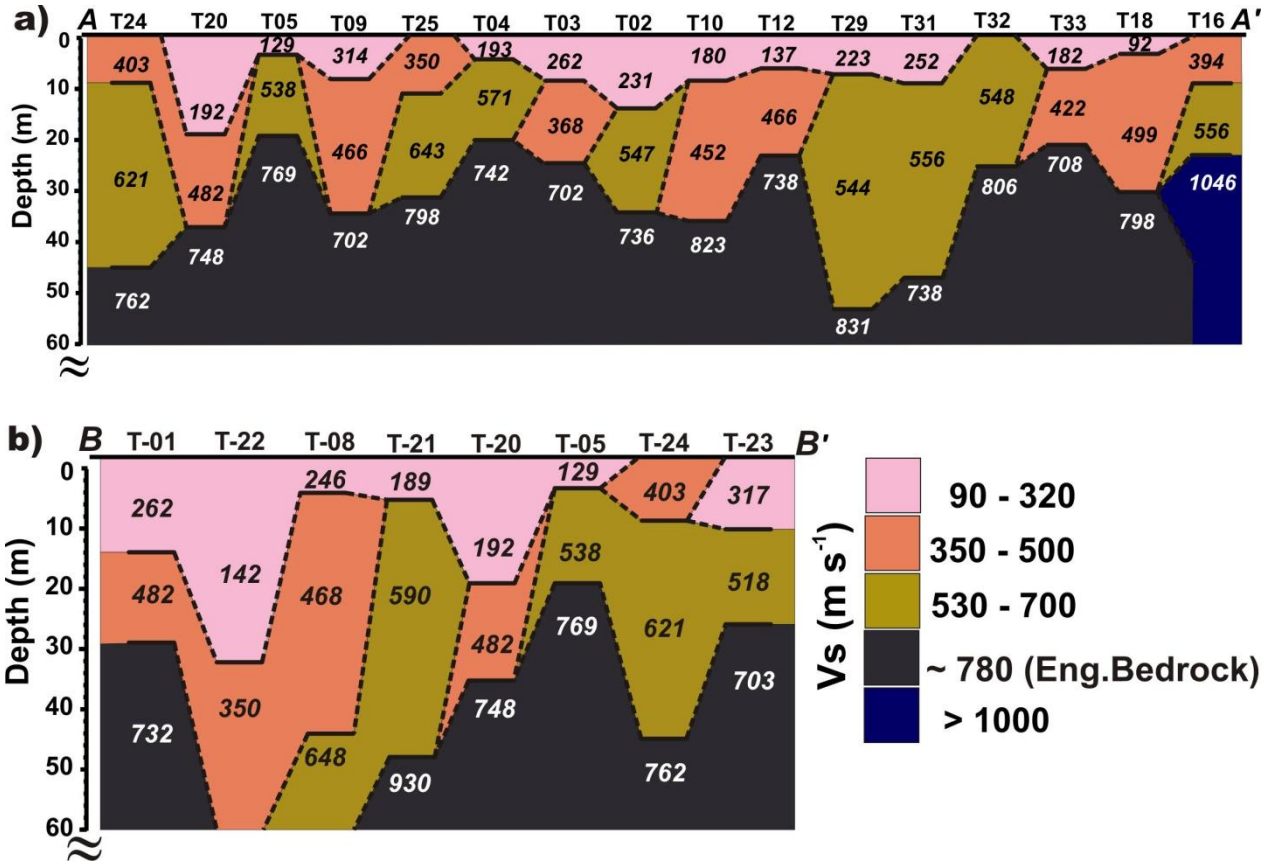

Figure 2.11 The 1D velocity cross sections for A-A´ (a) and B-B´ (b) profiles in Figure 2.2 without considering the topography. The layers are colored according to their Vs intervals in Figure 2.9.

2.6.2 Horizontal-to-Vertical Spectral Ratios

The spectral ratios between the horizontal and vertical components of the observed microtremor data were compared with the computed ellipticity of fundamental-mode Rayleigh-waves for the inverted 1D soil profiles in Figure 2.8. Aim of the comparison was to confirm the appropriateness of the inversion. Comparisons for two selected sites from each *group (a-h)* are shown in Figure 2.12. I followed the steps described by Zanieh et al. (2012) for the spectral ratio calculation. The Fourier amplitude spectra were calculated using 81.92 sec time segments and then smoothed using the Parzen window with a bandwidth of 0.1 Hz.

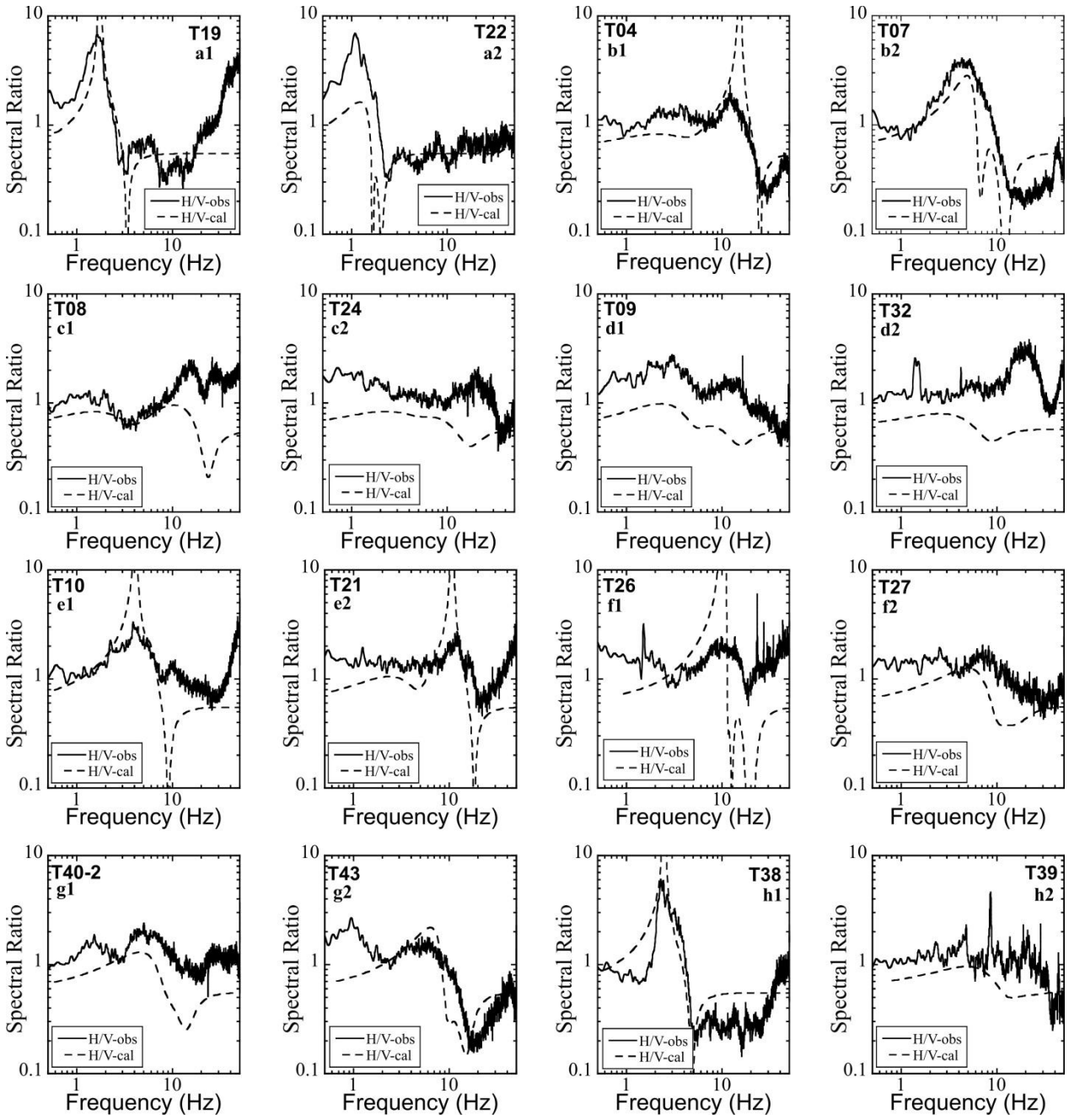

Figure 2.12 Spectral ratio (H/V) of the observed microtermor data (solid line) with computed ellipticity of the fundamental-mode Rayleigh waves (dashed lines) for selected sites from each *groups* in Figure 2.6.

Generally the sites that had a thin first layer with low velocities exhibited a dominant peak at high frequencies (~10 Hz) due to high velocity contrast (i.e. T04, T21, T26). On the other hand, the observed peak values at low frequencies (~1-3 Hz) for much thicker first layers with low velocities (~150 m/s) (i.e. alluvial at T19, T22, T38). The sites with no significant velocity contrast between the layers had almost flat characteristics in the frequency range of 0.4-10 Hz (i.e.

T24, T27, T32, and T39). The sites in Muratli and Corlu town had similar flat characteristics at a frequency up to ~6 Hz (T40-2, T43).

Comparison between the observed and calculated H/V ratios shows that the observed peak frequency characteristics are in good agreement with the ellipticity at frequencies between 1 and 20 Hz. All the observed and calculated peak frequencies of the H/Vs were compared in logarithmic graphs as shown in Figure 2.13.

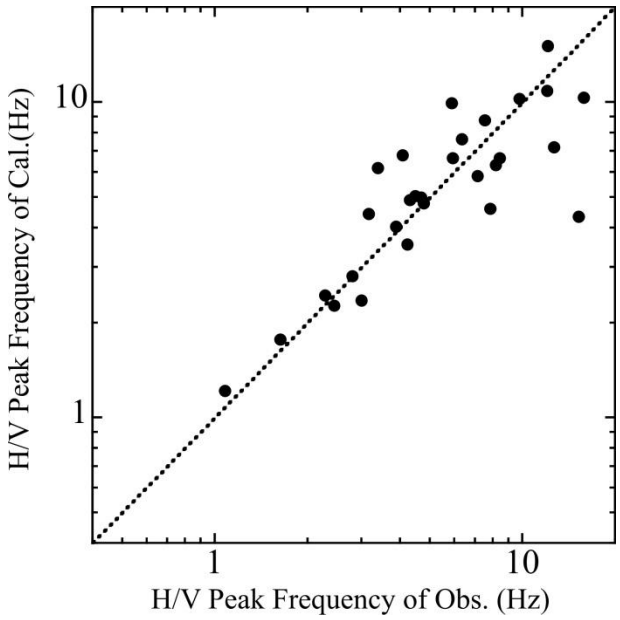

Figure 2.13 Comparison between observed and calculated peak frequencies of H/V results.

2.6.3 AVs30 Distribution

The average shear wave velocity values for the upper most 30 m (AVs30) were calculated according to the following CEN (2004) equation,

$$AVs_{30} = \frac{30}{\sum_{i=1}^{N} \frac{h_i}{V_i}}$$

where h_i and V_i denote the thickness (in meters) and the shear-wave velocity of the *i-th* layer, in a total of *N*, existing in the top 30 m. The AVs30 histogram is given in Figure 2.14 and indicates a

normal distribution with an average value of 410 m/s. AVs30 for most of the sites were distributed from 300 to 500 m/s in Tekirdag.

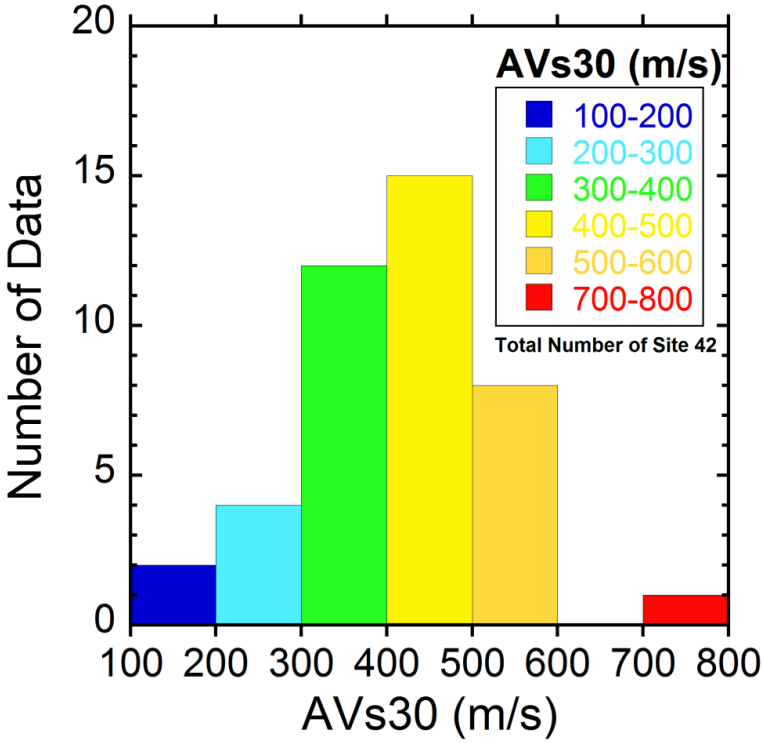

Figure2.14 The AVs30 distribution of Tekirdag.

The average AVs30 values along the AA' profile is shown in Figure 2.10. While the AVs30 values were higher in the west and the north (~530 m/s), they decreased in the city center. However, the AVs30 increased for sites to the east of T28. Low values were observed at sites having thick low velocity stiff soil layers (i.e. T11, T19, T29).

According to the National Earthquake Hazards Reduction Program (NEHRP) site classification (A-E), 2 sites are on soft soil (E), 11 sites on stiff soil (D), 28 sites on very dense soil/soft rock (C), and 1 site on rock (B) (Table 2.1). The sites in the northern part of the city center and the east part along the coastline are on soft rock (C). Marmara Ereglisi is also located on the soft rock except for T39 and T38 that are on rock (B) and stiff soil (D), respectively. The sites T01, T07, T12 and T13 close to the sea are on stiff soil (D). T20 and T28 were also located on the alluvial creek bed and are classified as stiff soil (D). However, at T02, T10 and T11 located in stone units the AVs30 was around 310 m/s (stiff soil). Although the sites located near the seaside in Tekirdag

showed low AVs30 values (E-D), we found high values (C-B) in Marmara Ereglisi (Figure 2.18 a). T38 had a similarly low value (240 m/s) at an alluvial site. The AVs30 velocities in Corlu (C) were higher than Muratli (D). The only site in Muratli, T42, is on soft rock (490 m/s). It is located on the border between alluvial and continental clastic rocks and carbonates units.

2.6.4 1D Site Amplifications in Tekirdag

Site amplification factors were computed to understand the seismic motion behavior on the different geological units in the study area. Since we determined the depth to the engineering bedrock at 29 sites, a common half-space layer for each site as the engineering bedrock with the average Vs of ~780 m/s was used. We did not observe engineering bedrock beneath the other 13 sites. The thickness of layer above the engineering bedrock was assumed utilizing average engineering bedrock depth of neighboring sites in the amplification calculations for those sites (Table 2.1).

We used 1D wave propagation theory for vertically propagating S-waves to calculate site amplifications. The site amplifications were calculated with the assumption of 1D reverberations of vertical incident SH-wave in shallow soil over the engineering bedrock at the sites. Because of lack of the quality factor information (Q) for Tekirdag and surroundings, it was assumed to be constant at 1/15 of the S-wave velocity in m/s ($Q=Vs/15$) in this study (Iida et al. 2005).

Figure 2.15 shows the theoretical amplification factors for the 31 sites according to the NEHRP classification. There was only one site T39 on B class (rock) with a predominant frequency of 15.5 Hz and an amplification value of 2. T22 was located in the Cevizli River with a sediment layer thickness of 32 m. T19 was located in Gazioglu Creek (see Figure 2.11b) with a low velocity (120 m/s) thick first layer. The engineering bedrock could not be detected at these sites. T19 and T22 in E class had predominant frequencies of 1.6 and 1.0 Hz, respectively, with similar amplifications of ~9.

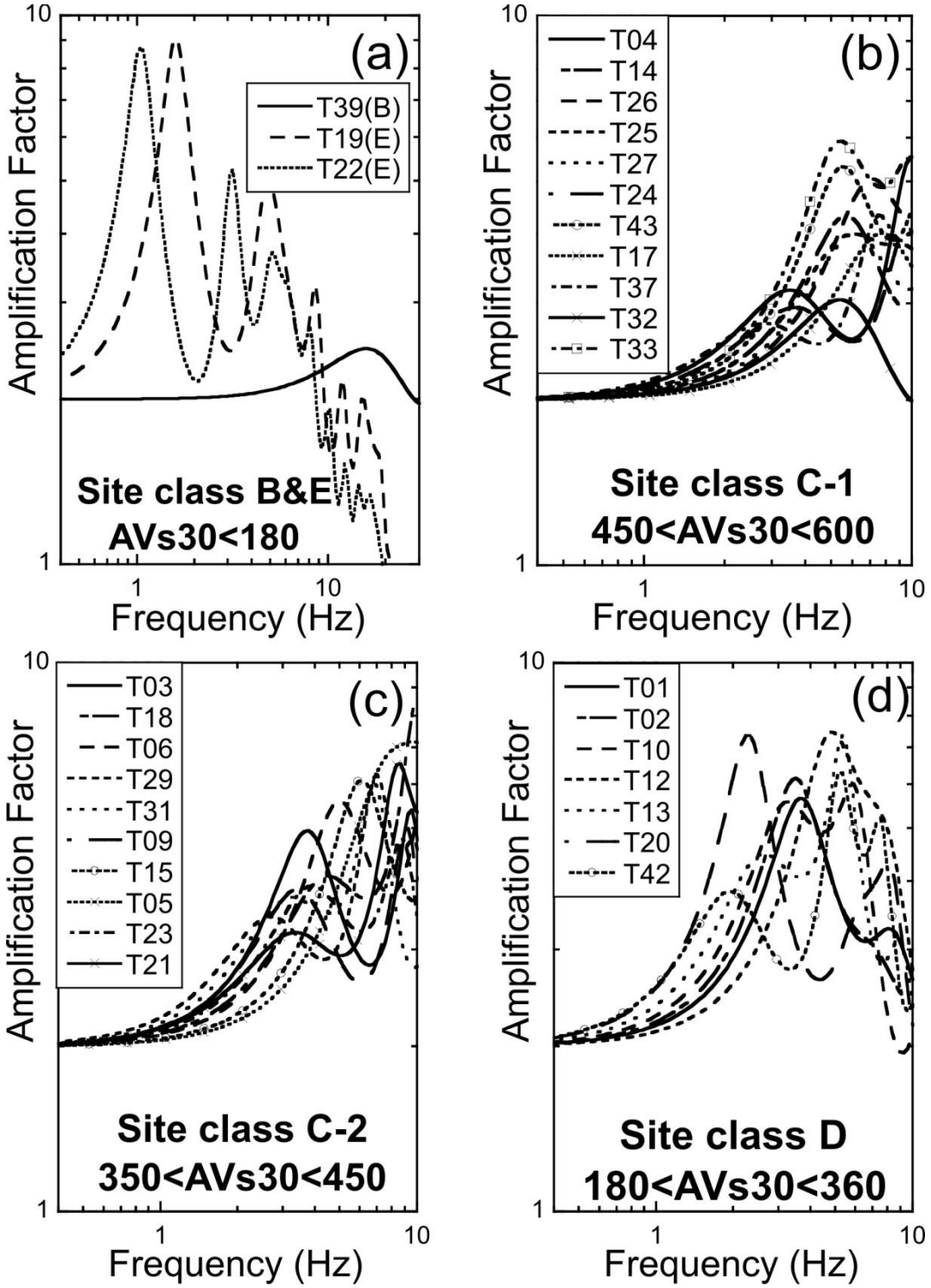

Figure 2.15 Comparison of the theoretical amplification for 32 sites according the NEHRP site classifications. The amplification values are computed using 1D transfer functions for vertically incident SH waves. The engineering bedrock S-wave velocity is Vs=780m/s. The Q value is assumed to be 1/15 of *Vs* (*Q*=*Vs*/15). Site class C divided into two subgroups according to velocity ranges C1: 450 <AVs30 < 600m/s, C2: 350 < AVs30 <450 m/s.

The sites in class C were divided into two subgroups according to their AVs30 velocity ranges: C-1 for 450-650 m/s and C-2 for 350-450 m/s. 11 sites in C-1 showed that the predominant frequencies ranged from 5 Hz to 15 Hz. The minimum amplification in the group was approximately 4, while the maximum amplification (~6.5) observed at T04 at a frequency of 13.5 Hz was similar at T27, both these sites being located on the youngest geological units. T14 had similar properties to T04 but the maximum frequency was 14.5 Hz, the same as T26. Although the predominant frequencies were similar (~5 Hz), amplification at T32 was half that at T33. The effect of the low velocity (~180 m/s) layer on the amplification at site T33 is clear.

C-2 contained 10 sites having dominant frequencies between 6 and 11 Hz. The minimum predominant frequency (~6 Hz) in the group was observed at site T15 located in the downtown of Marmara Ereglisi. T18 shows maximum amplification (~9) at 10 Hz due to a 2 m thin first layer and very low S-wave velocity (~90 m/s) of the alluvial material. We found that the predominant frequencies range for all sites in NEHRP class C were 5 – 15 Hz and the amplification values were observed to be between 3 and 9.

The sites in class D according to their AVs30 values (250-350 m/s) showed predominant frequencies between 2 and 6 Hz. The most significant amplification was found at T20 located on the alluvial of Cevizli Creek (see Figure 2.11b), with a minimum frequency of 2.3 Hz and an amplification factor of 7. A thick sediment layer affects both the frequency and amplification properties at this site. T12 and T13 also showed the same amplification values at ~5 Hz as at T20.

T02 had very similar velocity structure to T04. Both sites were located in crowded urban areas and indicated the same amplification (~6.5) with different predominant frequencies. While T04 had a peak value at 13.5 Hz, T02 had a frequency of 3.5 Hz due to the much thicker (17 m) first layer. On the other hand, T01 has the same predominant frequency as T02. It is clear from the results that the thickness and velocity of the first layer significantly affect site amplification.

The distributions of fundamental and predominant frequencies are shown in Figure 2.16. The results indicate that the fundamental frequency in the Tekirdag region were higher than all previous results as mentioned in 2.2 in Marmara Region. Only two sites located on the alluvial creek bed showed maximum amplification at less than 2 Hz. Most of the sites located on claystone, sandstone and siltstone units in Tekirdag had predominant frequencies higher than 2

Hz. The fundamental frequency range in Tekirdag was 1-10 Hz. However, the predominant frequency range was 1-16 Hz. As a result, Tekirdag city center and the northern parts have amplifications from 3 to 6 with fundamental frequency range of 2-3 and 4-6 Hz, respectively.

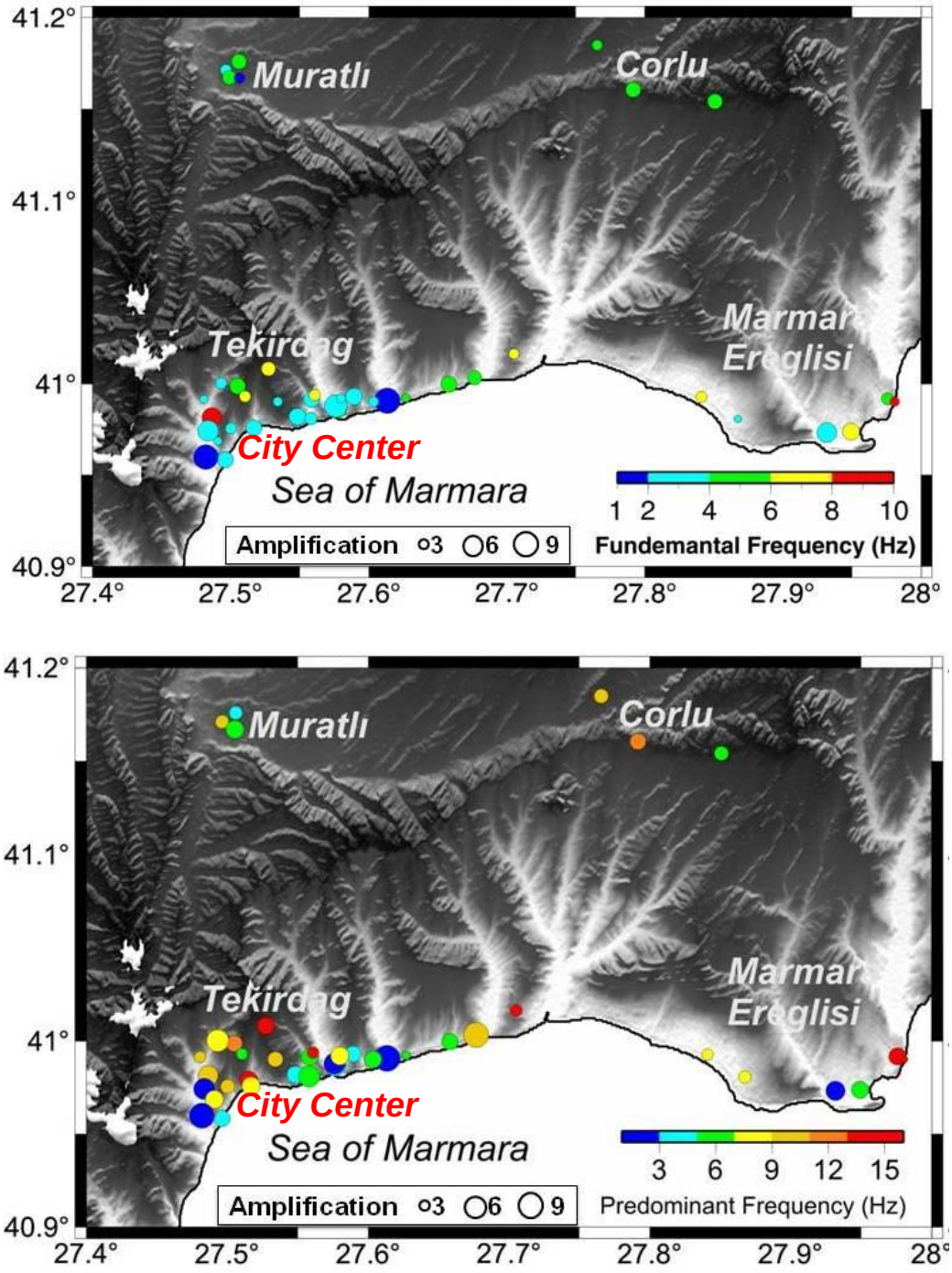

Figure 2.16 Fundamental (top) and predominant (bottom) frequency distribution in Tekirdag, Muratli, Corlu and Marmara Ereglisi. The size of the circles indicates amplification value at the site.

2.7 Results of AFAD station Microtremor Measurements

The S-wave velocity structures of the shallow soil part beneath the six AFAD strong ground motion stations (5902, 5906, 5907, 5908, 5910) in Tekirdag and the other six sites in Gokceada (1711), Enez (2201), Gelibolu (1710), Sarkoy (5904)and Canakkale city center (1701, 1713, 1714) (Figure 2.3) were determined. The parameters of these sites are detailed in Table 2.1

The results of observed the phase velocities, 1D S-wave velocity profiles and site amplifications according to azimuthal grouping are shown in Figure 2.17. The lowest and highest observed phase velocities are in the range of 100-200 m/s and 400-800 m/s, respectively. Enez, Sarkoy and Gelibolu stations have almost flat phase velocities around 200m/s. The lowest frequency limit is 2 Hz for 2201, 1710, and 5904, 1.5 Hz at Canakkale city center and 4 Hz at Tekirdag stations.

The observed phase velocity at each site was inverted to obtain the 1D S-wave velocity profiles. The S-wave velocity profiles indicate that the stations are located on the NEHRP site class of C and D with low AVs30 given in Table 2.1. The S-wave velocity of the engineering bedrock was taken as presumption of 0.78 km/s at all sites according to Tekirdag results. The engineering bedrock depth and its velocity were not available for the sites 2201, 1711, 1701, 1714, 5904 and 5906. The thicknesses of the layers lying on the engineering bedrock for these sites were assumed as given in Table 2.1 by utilizing profiles at neighborhood sites in the previous microtremor surveys, surface geology and drilling report for Canakkale city center by Buyuksarac et al. (2013).

The site amplifications were calculated following method for Tekirdag. The fundamental frequencies that are the lowest peak in the soil amplifications are easily identified only for 1711, 1713, 1714, 1710, 5902 and 5907. On the other hand, the predominant frequencies with the maximum peak are higher than 1 Hz except for 1701 with amplification factors between 3 and 7 in Figure 2.17. The site amplifications due to shallow soil effects were used in 1D simulation studies introduced in Chapter 4 and 5.

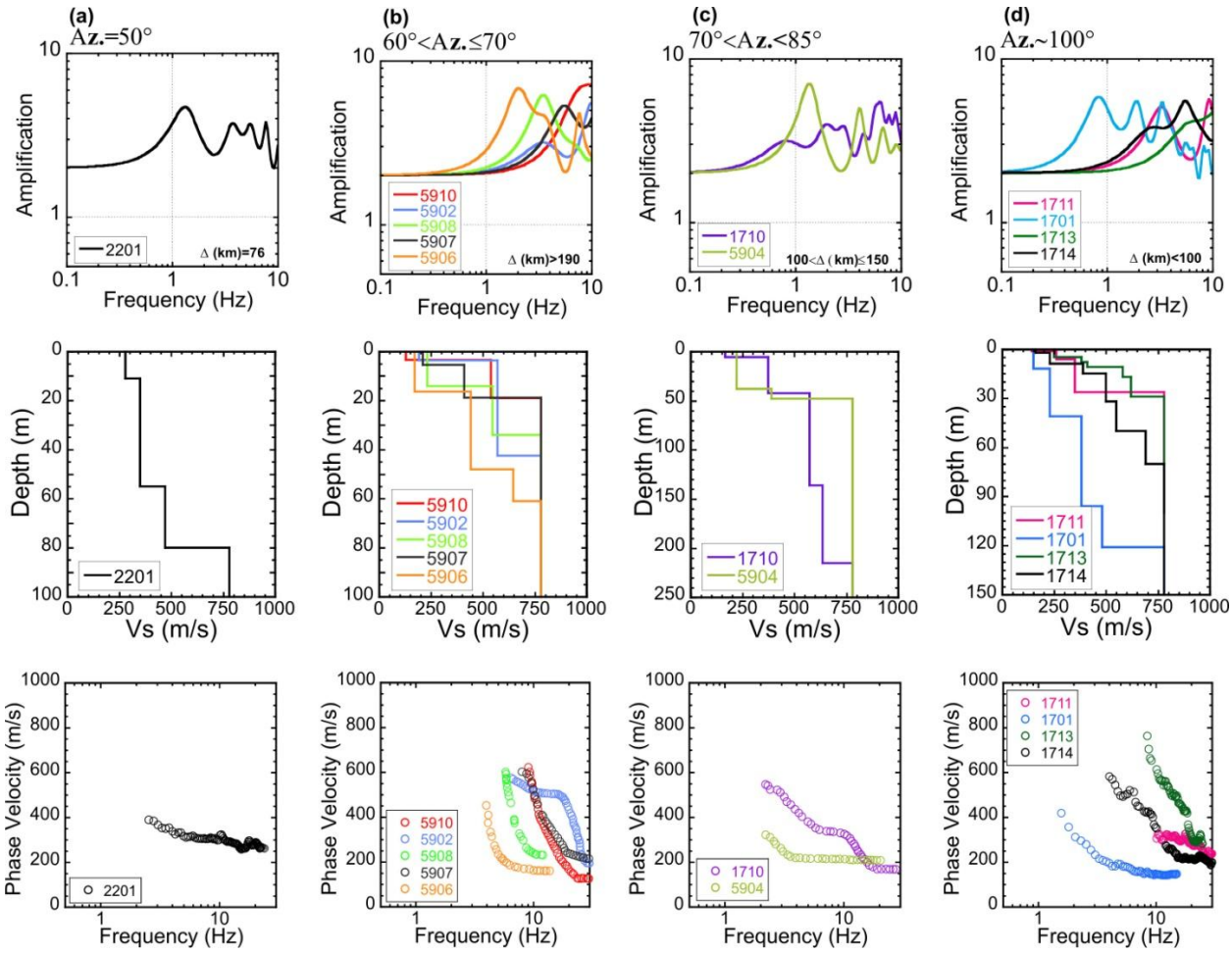

Figure 2.17 The phase velocities (bottom), 1D S-wave velocity structures (middle) and soil amplifications (top) at the microtremor sites that are close to the AFAD stations used in the 2014 Gokceada earthquake simulation. The sites were grouped according to their azimuthal distributions for the mainshock. Δ shows the epicentral distance. (a) Enez (b) Tekirdag city center, Corlu and Marmara Ereglisi, (c) Gelibolu and Sarkoy (d) Gokceada and Canakkale city center.

2.8 Discussion

2.8.1 AVs30 and Site Amplification Relationship

The relationship between the site amplification and AVs30 was examined. The average amplification factors were used at frequencies between 0.4 and 10 Hz (Figure 2.18). A good correlation between AVs30s and amplification values using a linear regression was found. Average amplifications on the alluvial sites showed slightly higher values than those predicted from the regression line. On the other hand, the value at a site on sandstone (T32) had smaller amplification than the empiric equation in general.

The alluvial units had higher amplification values than that of the other geological units. Sandstone sites designated as a soft rock (C) and rock sites (B) according to NEHRP showed the lowest amplification value with high AVs30 (T32 and T39) among the all site (Figure 2.18).

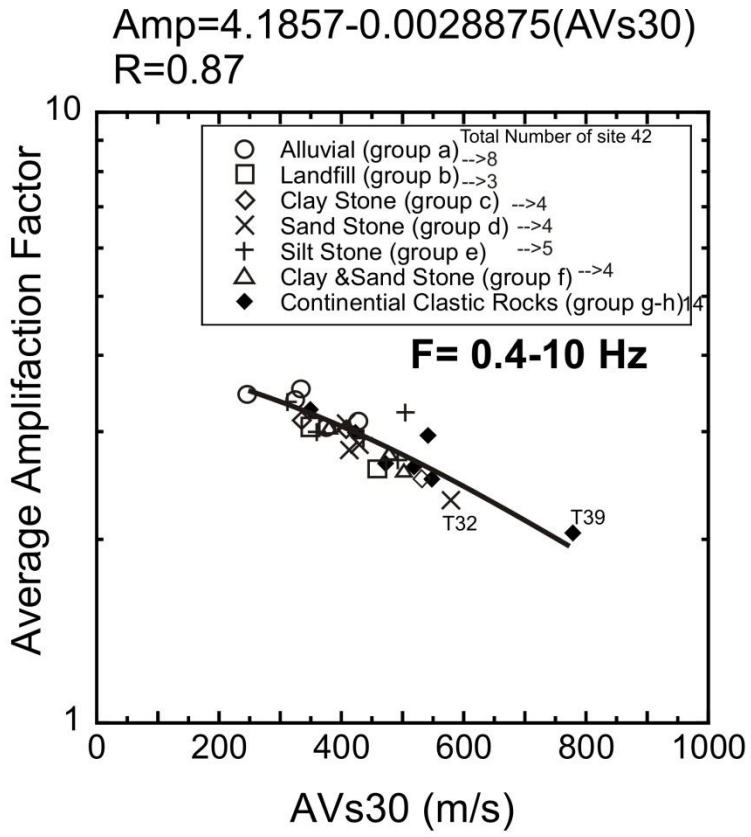

Figure 2.18 Relationship between average amplification factor and AVs30 values for 29 sites with respect to engineering bedrock (Vs=780m/s).The amplification factors are calculated in the frequency band of 0.4 - 10 Hz.

2.8.2 AVs30 and Slope Relationship

The average S-wave velocity in the upper 30 m is one of the principle parameters for further studies such as microzonation, ground motion prediction equations (GMPEs) etc. (i.e. Stewart et al. 2012). Recent studies have shown good correlation between AVs30 and the slope of topography (e.g., Matsuoka et al. 2006; Allen and Wald 2007; Lemoine et al. 2012; Stewart et al. 2012).

The NASA Shuttle Radar Topography Mission (SRTM) 3-seconds (90 m) topography data was used to generate a slope map of Tekirdag and surrounding region. The Generic Mapping Tools (GMT; Wessel and Smith 1998) routines were used to analyze the data. First, elevation data was resampled at 30 m for a smooth transition between the grid points and the derivatives (amplitude of slope). The average slope of each site was calculating using the neighboring grids (in 8 directions). Figure 2.19a shows the slope variation and AVs30 values for the sites in the Tekirdag. The Creek beds (alluvial areas) that had low slope and steep hills around the valleys had high slope amplitude. It is clear in Figure 2.19b that there is a linear relationship between AVs30 and slope. The correlation coefficient (R) was calculated 0.55. AVs30 in the city center were between 300-400 m/s, and were 400-500m/s in the west part of the city center. The maximum velocity was observed at T39 in Marmara Ereglisi. The AVs30 and slope values in Muratli were smaller than that of Corlu (Figure 2.19a).

The different geological units are also represented with different symbols according to the NEHRP site class range in Figure 19b. The sites on alluvial areas indicated low slope and velocities. The landfill areas had much high slope values because they are in the city center that settled on the hills. The sites on the siltstone, sandstone, claystone units were sparsely distributed. Continental clastic rocks that actually consist of silt/clay/sandstone units as mentioned before showed low average slope values because these units cover the flat areas of Corlu and Muratli towns. The highest slope values were observed in Marmara Ereglisi. Unlike the other sites, T39 in Marmara Ereglisi had highest velocity and slope value among the all sites. The results of the AVs30-slope are in good agreement with the study of worldwide study results of Allen and Wald (2007) (Figure 19b). The empirical AVs30 distribution was obtained in the area by using the AVs30-slope relationship is given in Figure 2.20. The empirical AVs30 values are higher than 500 m/s for the hillsides. Contrary, the creek beds with low slope show AVs30 with less than 350 m/s. The relationships for different geological rock groups are given in Figure 2.21. The correlation coefficient of all site-relationship (R=0.55) is similar with the relationship of group (a) and (b) (R=~0.43). Contrary continental clastic rock group (c) shows better correlation relationship (R=0.77).

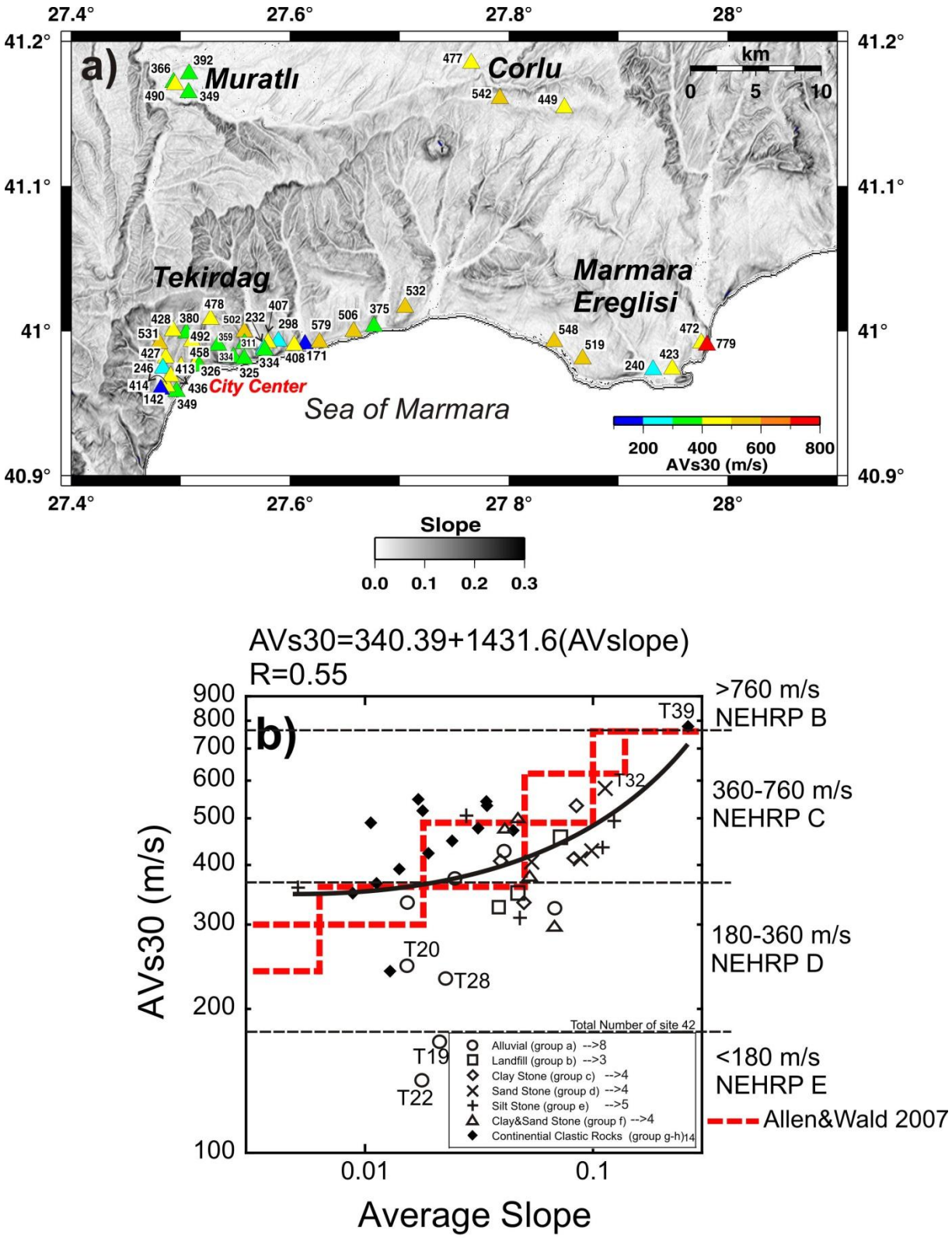

Figure 2.19 a) AVs30 value of the sites on the slope map of the study area. b) Relationship between average slope and AVs30 values for 42 sites. Slope ranges within NEHRP site class. The red dashed lines are AVs30-slope range by Wald and Allen (2007).

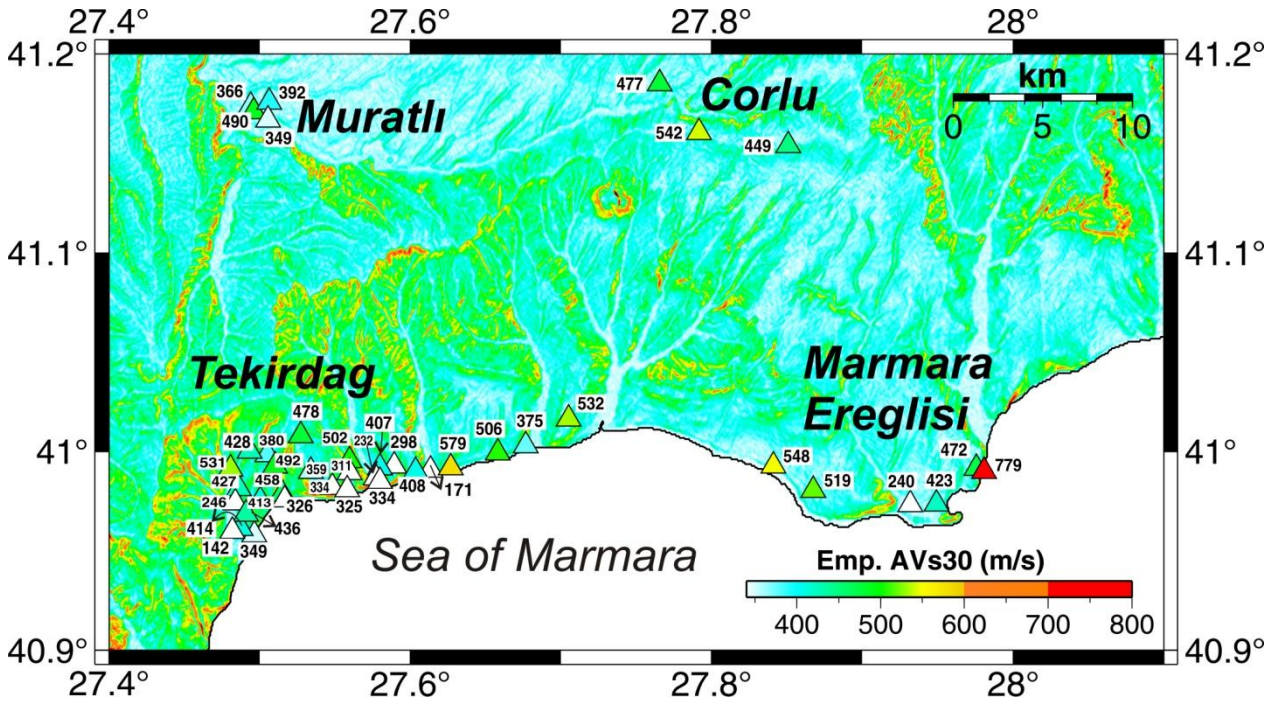

Figure 2.20 Distribution of empirical AVs30 according to slope. The calculated AVs30 from microtremor array studies were written on the sites.

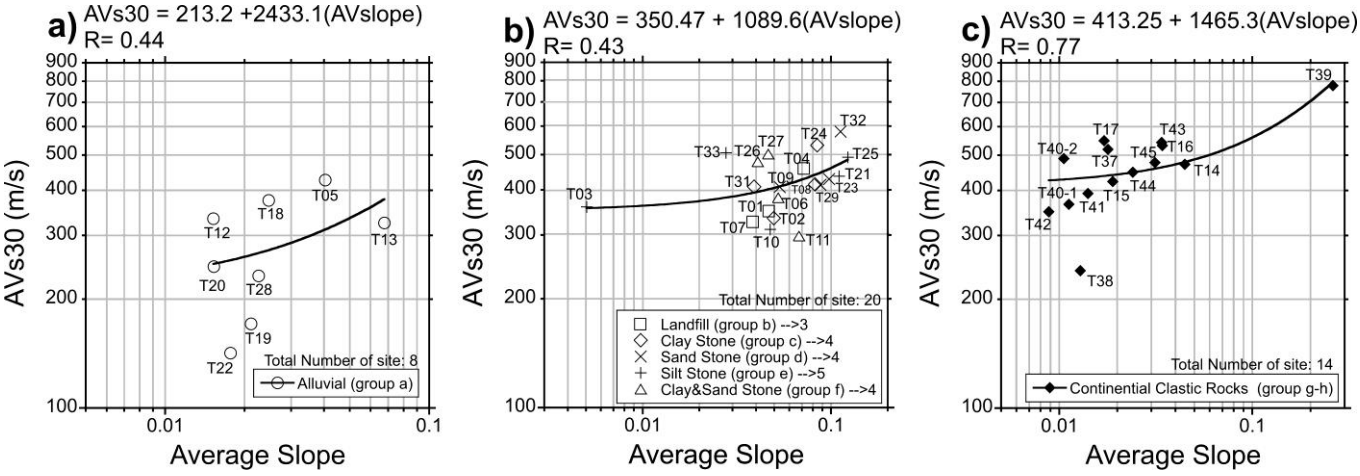

Figure 2.21 Relationship between average slope and AVs30 values for alluvial (a), group of landfill, claystone, sandstone, siltstone and clay&sand stone (b), continental-clastic rocks (c).

2.8.3 Comparison with previous MASW results at AFAD stations

There are seven strong motion stations operated by AFAD in Tekirdag, Corlu, Marmara Ereglisi (Figure 2.2). The S-wave velocity structure beneath three of them (5901, 5902, 5903) was determined by Multichannel Analysis of Surface Waves (MASW) method and their results were correlated with geotechnical boreholes (Akkar 2010). Figure 2.22 shows the comparison of 1D Vs soil profiles and site amplifications obtained with the MASW method at the AFAD stations and our array sites (T01, T04 and T15) that located nearby station.

AFAD-5901 strong ground motion station is located at the Meteorology Department. MASW and SPAC array measurements were done at almost the same place (distance ~5m) on the landfill area. The length of the seismic profile was 94 m in MASW method and SPAC method equivalent triangles lengths were 16-2 m (see Table 2.1). The results show that both methods observed until ~30 m (Figure 2.22a). The both measurement was performed on soil ground. The seven-layered MASW results are in good agreement with the 11.5 m long borehole. According to the borehole sampling, the thickness of the landfill is 0.6 m and they are clay and sand layers beneath it. The weak claystone unit was determined at the bottom of the borehole. However, we found three layer model from the SPAC method. The layer boundaries determined from both methods fit well (Figure 2.22a). The combination of three or four layers in the results of the MASW method corresponded to a layer at our SPAC 1D Vs profile (Figure 2.22a). MASW and SPAC analyzes indicate the AVs30 velocities as 472 and 349 m/s, respectively.

The AFAD-5902 station is located at the Governor House in Tekirdag city center. While the MASW was applied behind of the Governor House (on asphalt in the garden), T04 is located open public place in front of the Governor House and the area covered with paving-stone. The array size of SPAC is 20-2.5 m and the length of MASW seismic profile is 48 m. The distance between the two methods is about 60m. According to 10 m borehole observation at this site, the thickness of the artificial landfill is 0.9 m and sandy clay, weak sandstone and claystone were also reported in 9 m. The SPAC results show the uppermost layer has 4 m thick, and has lower velocity respect to MASW indicates a low velocity layer at shallow depth. It is difficult to interpret the low velocity zone for this site. The S-wave velocity about 8 m from MASW and of the first layer obtained from array measurement is the same. We determined second layer with

thickness of 16 m and its velocity is higher than that of MASW result. The AVs30 obtained from SPAC and MASW are 458 m/s and 409 m/s, respectively.

AFAD-5903 station was located in the District Governor Office in Marmara Ereglisi. The MASW method applied behind the office building with 94 m length of seismic profile. The borehole observation sampled the first 12 m of subsoil and uppermost ~4 m was denoted as artificial fill that over lie on weak sandstone and claystone layers. We applied 16-2 m array measurements (T15) in front of the office building. The average distance 100 m between the two locations. We obtained 4 m thickness for first layer from SPAC method while the MASW gave the thickness as 1 m (Figure 2.22a). The three layers SPAC 1D Vs profile matches well with the seven-layer model of MASW in average. AVs30 values are 423 m/s and 325 m/s SPAC and MASW, respectively.

Figure 2.22b shows the comparison of the site amplification between the SPAC and MASW results. The engineering bedrock velocity is accepted 780 m/s for both methods. The amplification of SPAC and MASW results show similar shapes and amplitude values, in general because of the similar S-wave velocity structure in average. However, it is clearly seen that there is a shift on frequency. The MASW (T04, T15) predominant frequencies are smaller than the SPAC frequency values. This may be caused by the low S-wave velocity profile obtained from MASW except first layer. On the contrary, T01 has smaller predominant frequency than that of AFAD-5901, because its velocity values are smaller than the results of MASW observation.

The main difference between MASW and SPAC results is the number of the estimated layers. The Vs velocities are in good agreement in means of average especially for T01 and T15. The results show that assumption of two-three-layer models for inversion was sufficient to determinate 1D shallow velocity profile in the study area.

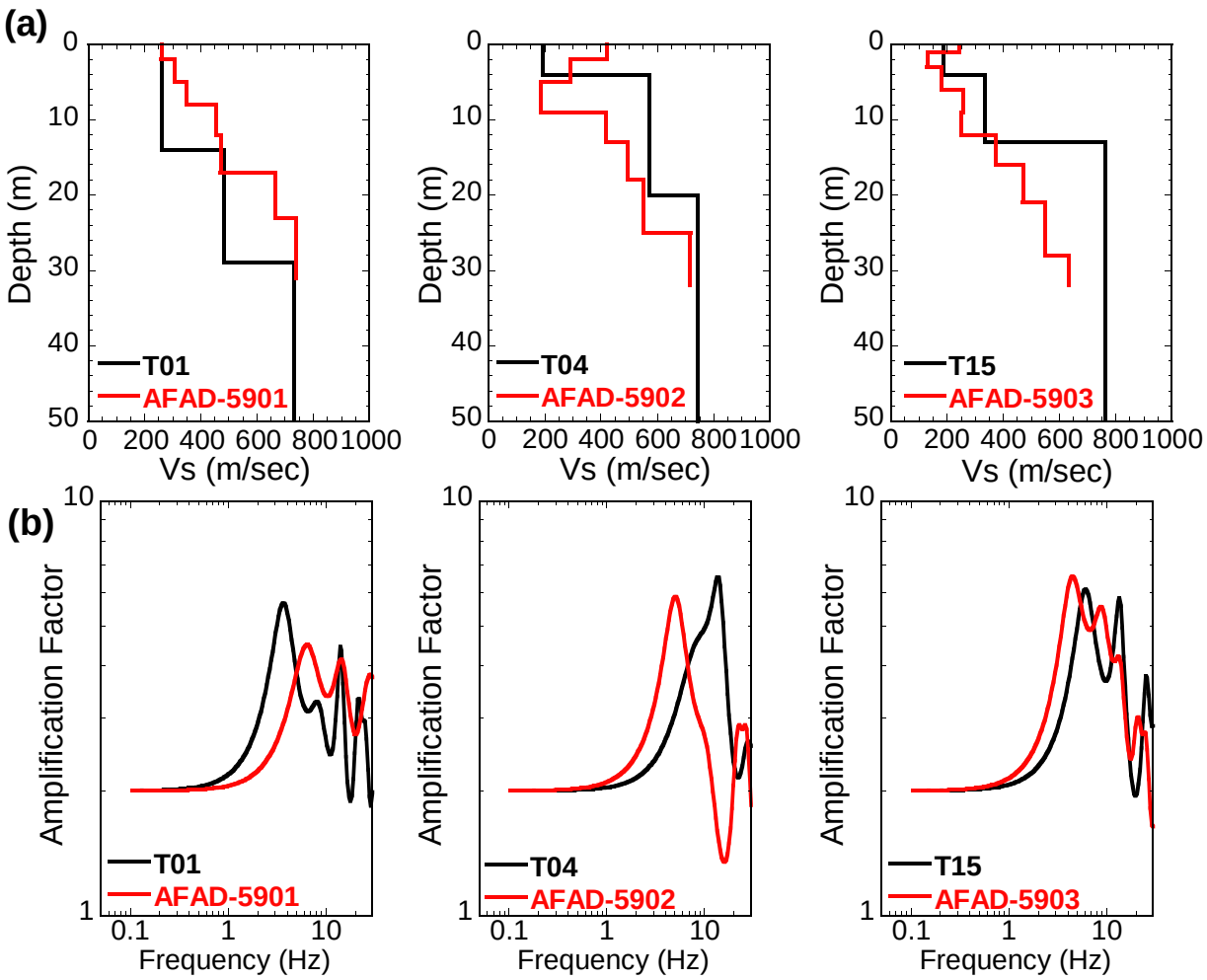

Figure 2.22 Comparison of the 1D Vs soil profiles (a) and site amplifications (b) at the AFAD stations (red) and at the microtremor array sites (black).

Chapter 3

Determination of 1D Deep Velocity Structure Using Surface Wave Group Velocity Dispersion Curves

3.1 Velocity Waveforms of the 2014 Gokceada Earthquake

3.2 Group Velocity Dispersion Curve Analyses of Surface Waves

3.3 Estimation of 1D Deep Velocity Structures

3.1 Velocity Waveforms of the 2014 Gokceada Earthquake

The velocity waveforms of the 2014 Gokceada mainshock given in Figure 3.1 were obtained with an integration of the observed acceleration records in the frequency domain after applying a baseline correction and a filter in a frequency range of 0.1-10 Hz. The station locations are given in Figure 3.2.

The station 2201 contains low frequency phases in the coda part (60-80 s) in particular on the NS component (Figure 3.1). Similarly, surface waves with high amplitudes are significant especially in the NS component of 5907. The stations in Canakkale (1713 and 1714) also contain surface waves with small amplitudes. The 5904 Sarkoy station has low frequency waves after 80 s in EW component.

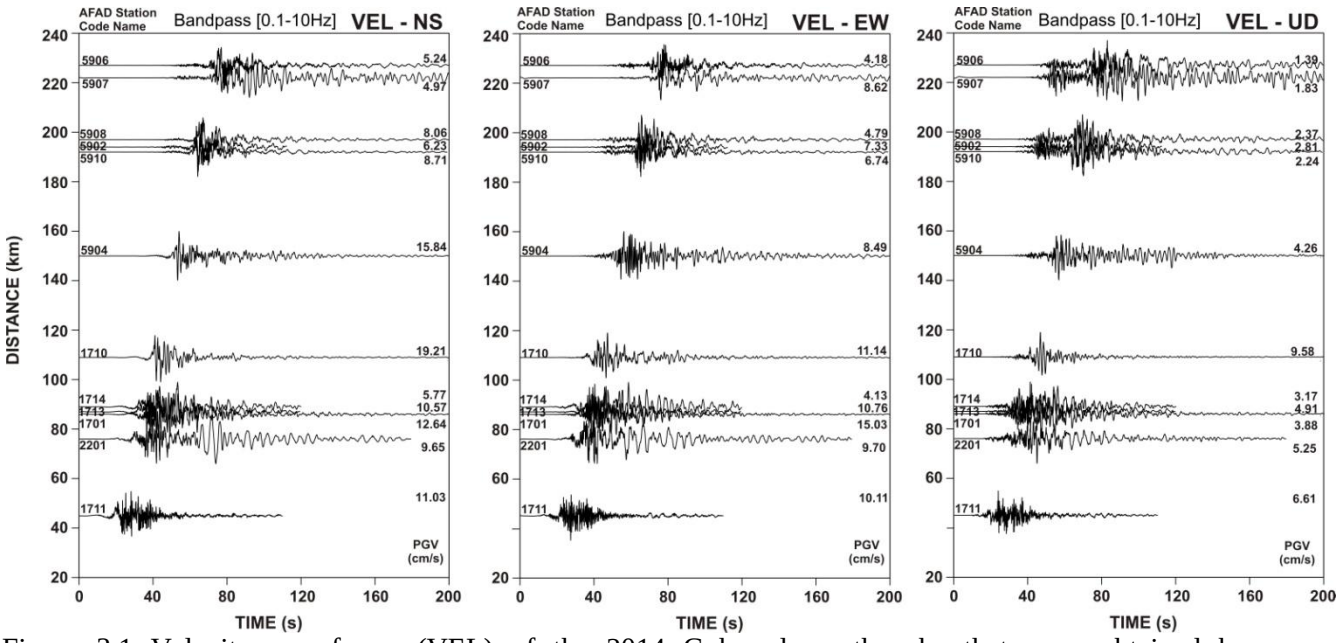

Figure 3.1 Velocity waveforms (VEL) of the 2014 Gokceada earthquake that were obtained by integration of the accelerograms in the frequency domain and were filtered in the range of 0.1 to 10 Hz. Each waveform is normalized by its maximum value. The waveforms are plotted according to the epicentral distance. The peak values are given on the right side of the seismograms.

3.2 Group Velocity Dispersion Curve Analyses of Surface Waves

It is well known that 3D velocity structural models are required for ground motion simulations, in particularly in a large basin. However, an approximation to a 1D velocity structure is still useful to generate synthetic ground motions at a site with no available structural data. We determined 1D velocity structures in different azimuthal directions by comparing theoretical surface wave group velocity dispersion curves with the observed records. Such a 1D velocity structures can be appropriate for modeling the low- frequency surface waves seen in observed records.

For this aim, surface wave group velocity dispersion curves from the ground motion of the 2014 Gokceada earthquake were used to determine the horizontal 1D velocity structures for deep sediment and earth's crust from focal layer to the engineering bedrock beneath the stations in the different azimuthal directions in Figure 3.2. The epicentral distances of the AFAD stations are between 45 and 227 km as listed in Table 3.1.

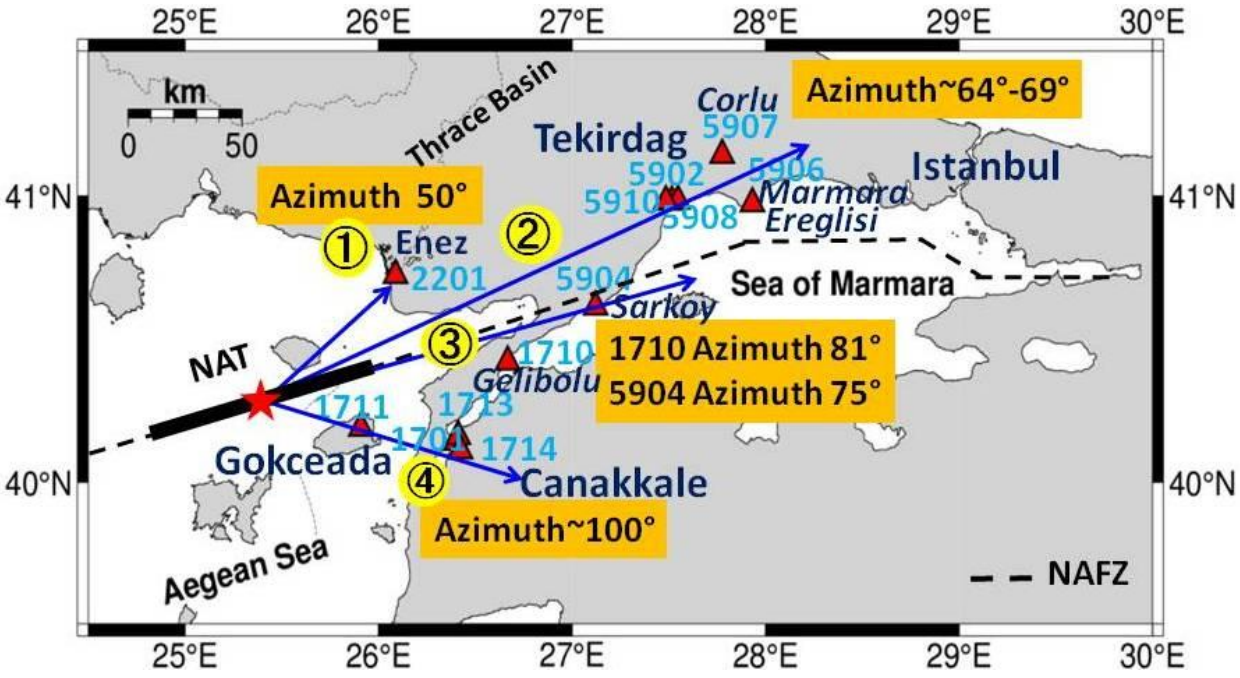

Figure 3.2 The four station groups (yellow numbers) according to their azimuthal directions. The strong ground motion stations are shown with red triangles and their codes are given with blue numbers. Red star and thick black line are the epicenter and fault line of the 2014 Gokceada earthquake in the North Aegean Though (NAT), respectively. Dashed black line is the NAFZ.

Table 3.1 Parameters of strong ground motion stations for the 2014 Gokceada earthquake.

Station Code	Latitude (°N)	Longitude (°E)	Epicentral Distance (km)	Station Azimuth (°)
1711	40.19082	25.90783	45	103
2201	40.72448	26.08731	76	50
1701	40.14114	26.39948	86	100
1713	40.16216	26.41160	87	98
1714	40.11291	26.42205	89	102
1710	40.42334	26.66715	109	81
5904	40.61485	27.12256	150	75
5910	40.98109	27.48608	192	65
5902	40.97928	27.51504	194	66
5908	40.98205	27.54794	197	66
5907	41.14180	27.77633	222	64
5906	40.97338	27.93164	227	69

Seismic waves are affected by surface and subsurface irregularities. In the general case, a wave field is separated into two wave fields: P-SV and SH. Rayleigh waves can appear in the P/SV-wave field, while Love waves can appear only in the SH-wave field with a layered structure (AIJ, 1993). Sometimes it is difficult or impossible to identify the wave types on the seismograms. During the analyses of the velocity seismograms of the mainshock, it was assumed that Rayleigh and Love waves are observed on vertical/radial (V/R) and transverse (T) components, respectively. Therefore, the NS and EW components were converted to radial and transverse components using the back-azimuth angle (α) in the transformation equation given below.

$$\begin{pmatrix} R \\ T \end{pmatrix} = \begin{pmatrix} \cos(\alpha) & \sin(\alpha) \\ \sin(\alpha) & -\cos(\alpha) \end{pmatrix} \begin{pmatrix} NS \\ EW \end{pmatrix}$$

The flow chart of the surface wave group velocity procedure is given Figure 1.10 (in Chapter1). Dispersive features of the vertical/radial and transverse waveforms were extracted from the multiple filter method (Dziewonski 1969). Envelopes of the waveforms at selected frequencies between 0.07 and 1 Hz were calculated and arrival times of dispersive surface waves were estimated from the envelope waves as the group delay times. Then, epicentral distance (Δ km) was divided by the group delay times to calculate observed group velocities at each frequency.

A common initial deep velocity model that consists of seven horizontal layers beneath the engineering bedrock was established from the previous studies (Bécel et al. 2009; Karabulut et al. 2006, 2011; Chimoto et al. 2015) for theoretical group velocities (Figure 3.3). The first layer

corresponds to the engineering bedrock with an S-wave velocity of 0.78 km/s defined in Tekirdag microtremor studies (Chapter 2). The S-wave velocities and thicknesses of the second and third layers were determined from previous microtremor exploration with large arrays by Chimoto et al. (2015). The P-wave velocities for the first three layers are estimated from S-wave velocities using an empirical relation by Kitsunezaki et al. (1990). P-wave velocities and thicknesses of deep layers from the 4th layer to the Moho were estimated from the results of previous studies (Bécel et al. 2009; Karabulut et al. 2006, 2011). These three studies have common discontinuities for layers' interfaces with the velocities of about 5.7-5.9, 6.3-6.4, 6.7-6.8 and 8 km/s at depths of about 4-5, 20-22, 24-26 and 34 km, respectively (Figure 3.3). S-wave velocities of these layers were estimated assuming the ratio between P-wave and S-wave of 1.73. The densities of the layers were given as 2.1 to 3.3 g/cm^3.

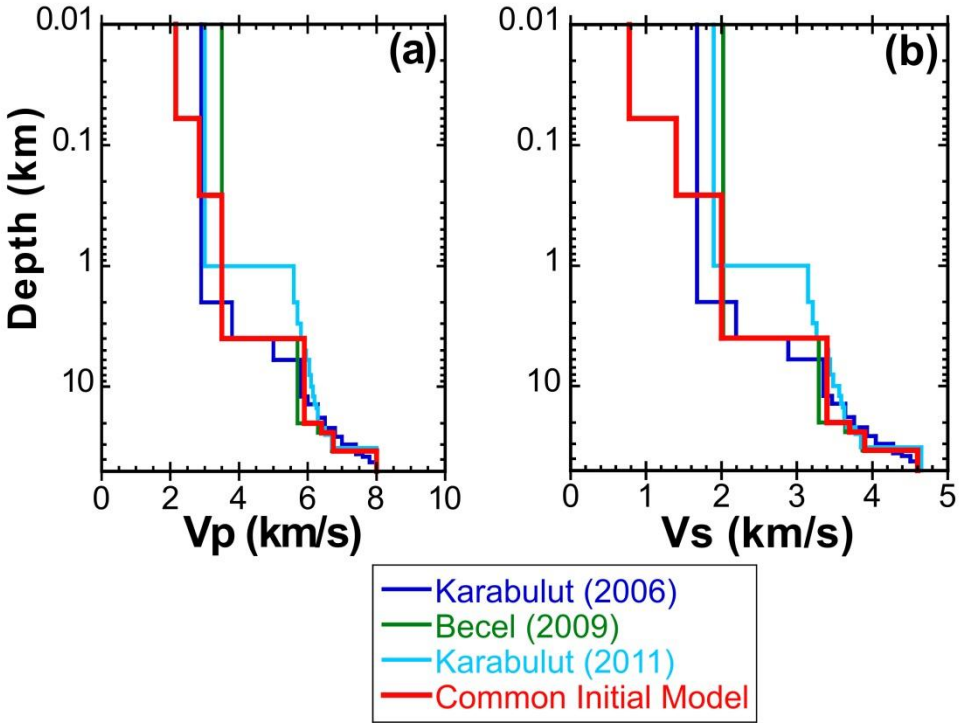

Figure 3.3 Previous velocity models for the study area proposed by Bécel et al. (2009) and Karabulut et al. (2006, 2011). The common initial velocity model used in the group velocity tuning is shown with red line.

The S-wave velocities and thicknesses of layers between the focal layer and engineering bedrock in the initial model were tuned at the stations in azimuthal groups by a try-and-error fitting the theoretical group velocity dispersion curves for fundamental Rayleigh and Love waves with observed ones as given in the flow chart (Figure 1.10 in Chapter 1).

3.3 Estimation of 1D Deep Velocity Structures

The multiple filter analyses were applied to the radial/vertical and transverse components at the stations in each azimuthal direction and their results are given in Figure 3.4. The closest station (1711) to the epicenter has no dispersion characteristics of the surface waves. The arrival times of the surface waves were observed between 50 and 80s for the four azimuthal directions. The group delay time picked as times of phases with peak amplitudes of the Rayleigh and Love waves are shown on the envelopes at different frequencies on the left panels in Figure 3.4. The observed group delay times and group velocities of the velocity waveforms at the stations are given in Table 3.2. The initial models are modified in a try-and-error procedure to get sufficient fitting of the theoretical group velocity to the observed one assuming fundamental mode.

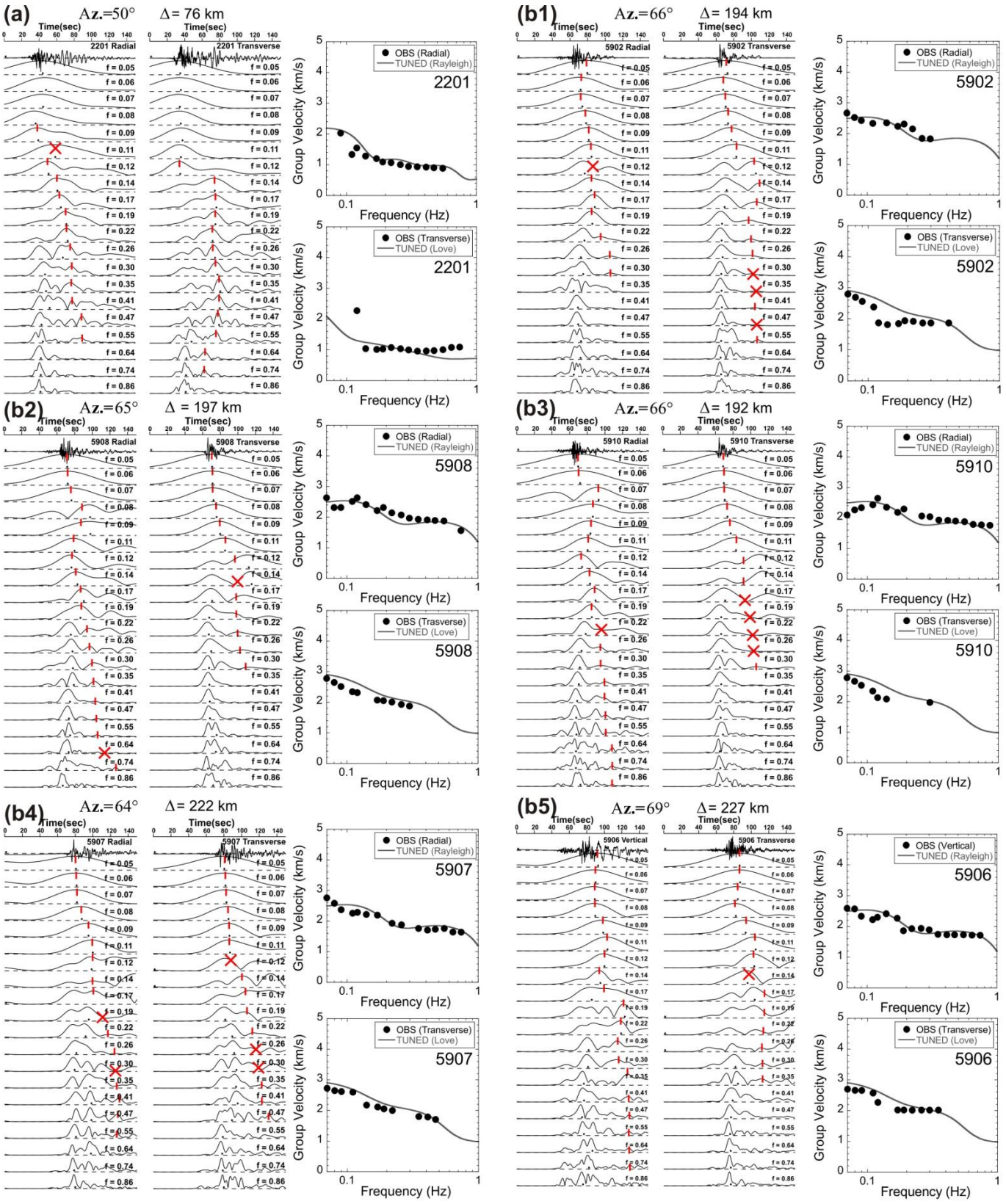

Continue on next page

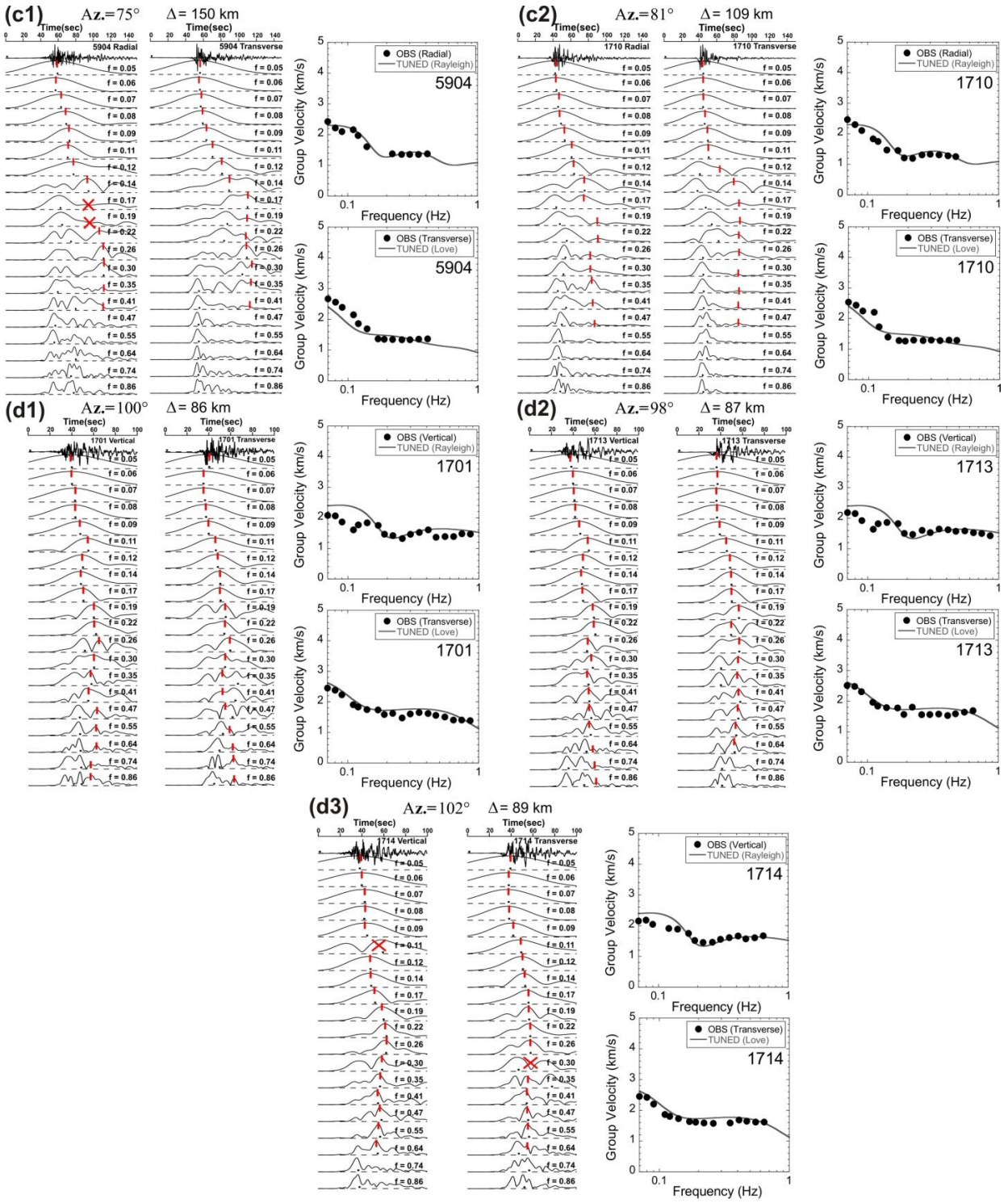

Figure 3.4 Result of multiple filter analysis for the radial or vertical (most left) and transverse (second from left) components at the stations in each azimuthal direction: 2201 (a), 5902, 5910, 5908, 5907, 5906 (b), 1710, 5904 (c), and 1701, 1713, 1714 (d). The envelopes of seismograms are given for the frequency range between 0.05 and 0.86 Hz. Red line shows the group delay time of surface waves at each frequency. Red cross shows the failure in reading the group delay time. The comparison between the group velocities of observed and tuned models for Rayleigh (top) and Love (bottom) waves are given on the right hand side of the seismograms.

Table 3.2 Observed Group Time (GT) and Group Velocity (GV) for the radial (a) and transverse (b) components of the stations.

a)

f (Hz)	2201-Radial		5902-Radial		5908-Radial		5910-Radial		5907-Radial		5906-Vertical	
	GT (s)	GV (m/s)	GT (s)	GV (m/s)	GT (s)	GV (m/s)	GT (s)	GV (m/s)	GT (s)	GV (m/s)	GT (s)	GV (m/s)
0.05	X	X	78.24	2.48	70.05	2.81	68.14	2.82	79.24	2.80	91.40	2.48
0.06	X	X	70.65	2.75	70.63	2.79	70.39	2.73	80.06	2.77	88.47	2.57
0.07	X	X	72.63	2.67	74.81	2.63	91.39	2.10	80.41	2.76	87.62	2.59
0.08	X	X	76.89	2.52	85.00	2.32	84.80	2.26	85.89	2.58	88.16	2.57
0.09	37.43	2.03	79.90	2.43	85.00	2.32	82.10	2.34	93.47	2.38	97.17	2.34
0.11	56.90	1.34	83.05	2.34	78.28	2.52	78.94	2.43	98.34	2.26	102.05	2.22
0.12	49.16	1.55	X	X	74.79	2.63	72.57	2.65	97.02	2.29	98.57	2.30
0.14	59.38	1.28	82.48	2.35	81.63	2.41	81.63	2.35	100.00	2.22	94.02	2.41
0.17	63.31	1.20	86.69	2.24	88.88	2.22	87.87	2.19	101.00	2.20	100.00	2.27
0.19	69.60	1.09	83.92	2.31	85.01	2.32	83.67	2.29	X	X	121.87	1.86
0.22	71.11	1.07	90.00	2.16	92.00	2.14	X	X	115.00	1.93	117.64	1.93
0.26	75.60	1.01	105.00	1.85	95.00	2.07	93.00	2.06	118.00	1.88	117.00	1.94
0.30	80.15	0.95	106.00	1.83	100.00	1.97	94.00	2.04	X	X	118.00	1.89
0.35	81.37	0.93	X	X	102.00	1.93	99.20	1.94	126.00	1.76	130.00	1.75
0.41	82.42	0.92	X	X	103.00	1.91	99.80	1.92	130.00	1.71	131.00	1.73
0.47	84.13	0.90	X	X	104.00	1.89	101.00	1.90	128.00	1.73	131.10	1.73
0.55	85.76	0.89	X	X	105.00	1.88	102.00	1.88	126.00	1.76	131.15	1.73
0.64	X	X	X	X	X	X	107.00	1.79	X	X	132.00	1.72
0.74	X	X	X	X	126.00	1.56	108.00	1.78	135.00	1.64	132.20	1.72
0.86	X	X	X	X	X	X	109.00	1.76	135.50	1.64	X	X

f (Hz)	1710-Radial		5904-Radial		1701-Verical		1713-Vertical		1714-Verical	
	GT (s)	GV (m/s)	GT (s)	GV (m/s)	GT (s)	GV (m/s)	GT (s)	GV (m/s)	GT (s)	GV (m/s)
0.05	40.90	2.67	X	X	38.32	2.24	36.87	2.36	36.68	2.43
0.06	42.27	2.58	55.44	2.71	38.47	2.24	38.51	2.26	38.53	2.31
0.07	44.19	2.47	61.74	2.43	41.34	2.08	39.83	2.18	41.30	2.16
0.08	47.41	2.30	67.58	2.22	41.60	2.07	40.35	2.16	40.79	2.18
0.09	51.66	2.11	71.41	2.10	46.11	1.87	45.19	1.93	43.48	2.05
0.11	59.45	1.83	69.34	2.16	53.54	1.61	53.11	1.64	X	X
0.12	62.27	1.75	75.99	1.97	48.61	1.77	47.77	1.82	46.52	1.91
0.14	74.11	1.47	93.14	1.61	46.77	1.84	46.73	1.86	47.15	1.89
0.17	75.00	1.45	X	X	49.04	1.75	47.75	1.82	50.78	1.75
0.19	90.00	1.21	X	X	58.67	1.47	57.79	1.51	58.54	1.52
0.22	91.00	1.20	109.02	1.38	60.64	1.42	59.17	1.47	61.24	1.45
0.26	83.00	1.31	110.38	1.36	65.00	1.32	54.19	1.61	60.86	1.46
0.30	82.00	1.33	110.40	1.36	58.84	1.46	56.78	1.53	57.13	1.56
0.35	83.00	1.31	110.48	1.36	56.44	1.52	52.82	1.65	55.23	1.61
0.41	85.00	1.28	108.86	1.38	53.44	1.61	53.65	1.62	53.39	1.67
0.47	87.00	1.25	X	X	63.00	1.37	55.31	1.57	56.60	1.57
0.55	X	X	X	X	62.00	1.39	54.83	1.59	X	X
0.64	X	X	X	X	62.00	1.39	57.00	1.53	55.31	1.61
0.74	X	X	X	X	58.00	1.48	58.00	1.50	53.16	1.67
0.86	X	X	X	X	58.50	1.47	61.00	1.43	X	X

b)

f (Hz)	2201-Transverse		5902-Transverse		5908-Transverse		5910-Transverse		5907-Transverse		5906-Transverse	
	GT (s)	GV (m/s)	GT (s)	GV (m/s)	GT (s)	GV (m/s)	GT (s)	GV (m/s)	GT (s)	GV (m/s)	GT (s)	GV (m/s)
0.05	X	X	71.40	2.72	69.23	2.85	67.10	2.86	78.90	2.81	80.72	2.81
0.06	X	X	66.42	2.92	69.74	2.82	67.95	2.83	80.25	2.77	82.39	2.76
0.07	X	X	69.38	2.80	70.82	2.78	68.99	2.78	81.38	2.73	84.04	2.70
0.08	X	X	72.04	2.69	74.31	2.65	72.07	2.66	83.75	2.65	85.32	2.66
0.09	X	X	75.78	2.56	78.35	2.51	75.70	2.54	84.73	2.62	85.36	2.66
0.11	X	X	81.44	2.38	83.90	2.35	81.75	2.35	85.34	2.60	88.25	2.57
0.12	33.39	2.28	103.67	1.87	85.00	2.32	90.00	2.13	X	X	100.00	2.27
0.14	72.91	1.04	107.00	1.81	X	X	92.00	2.09	102.00	2.18	X	X
0.17	74.72	1.02	105.00	1.85	95.00	2.07	X	X	105.00	2.11	112.08	2.03
0.19	73.65	1.03	100.00	1.94	96.00	2.05	X	X	108.00	2.06	112.21	2.02
0.22	70.48	1.08	101.00	1.92	98.00	2.01	X	X	111.00	2.00	112.64	2.02
0.26	73.19	1.04	104.00	1.87	102.00	1.93	X	X	X	X	112.50	2.02
0.30	75.91	1.00	104.00	1.87	105.00	1.88	97.00	1.98	X	X	112.42	2.02
0.35	79.15	0.96	X	X	X	X	X	X	123.00	1.80	112.40	2.02
0.41	78.57	0.97	104.00	1.87	X	X	X	X	124.00	1.79	130.00	1.75
0.47	77.75	0.98	X	X	X	X	X	X	130.00	1.71	130.20	1.74
0.55	75.26	1.01	X	X	X	X	X	X	X	X	X	X
0.64	70.37	1.08	X	X	X	X	X	X	X	X	X	X
0.74	69.56	1.09	X	X	X	X	X	X	X	X	X	X
0.86	X	X	X	X	X	X	X	X	X	X	X	X

f (Hz)	1710-Transverse		5904-Transverse		1701-Transverse		1713-Transverse		1714-Transverse	
	GT (s)	GV (m/s)	GT (s)	GV (m/s)	GT (s)	GV (m/s)	GT (s)	GV (m/s)	GT (s)	GV (m/s)
0.05	43.25	2.52	X	X	39.02	2.20	34.69	2.51	37.77	2.36
0.06	43.07	2.53	55.29	2.71	33.68	2.55	35.55	2.45	36.30	2.45
0.07	42.94	2.54	56.15	2.67	35.07	2.45	34.59	2.52	36.25	2.46
0.08	44.71	2.44	58.54	2.56	36.04	2.39	35.03	2.48	36.70	2.43
0.09	48.43	2.25	62.74	2.39	38.48	2.23	37.64	2.31	40.38	2.20
0.11	49.38	2.21	69.69	2.15	45.08	1.91	44.22	1.97	47.69	1.87
0.12	63.00	1.73	80.53	1.86	46.87	1.83	47.18	1.84	49.31	1.80
0.14	78.00	1.40	88.67	1.69	49.16	1.75	48.49	1.79	51.42	1.73
0.17	85.00	1.28	109.66	1.37	49.45	1.74	48.79	1.78	54.41	1.64
0.19	86.00	1.27	110.65	1.36	54.14	1.59	55.43	1.57	55.06	1.62
0.22	84.00	1.30	111.31	1.35	52.85	1.63	48.10	1.81	56.05	1.59
0.26	85.00	1.28	111.98	1.34	58.26	1.48	55.68	1.56	56.36	1.58
0.30	84.00	1.30	112.06	1.34	53.52	1.61	55.50	1.57	X	X
0.35	85.00	1.28	110.60	1.36	52.00	1.65	55.00	1.58	56.01	1.59
0.41	84.00	1.30	109.77	1.37	53.00	1.62	56.60	1.54	52.75	1.69
0.47	84.50	1.29	X	X	55.00	1.56	54.79	1.59	54.10	1.65
0.55	X	X	X	X	57.00	1.51	52.91	1.64	54.92	1.62
0.64	X	X	X	X	61.00	1.41	51.41	1.69	55.00	1.62
0.74	X	X	X	X	61.00	1.41	X	X	X	X
0.86	X	X	X	X	62.00	1.39	X	X	X	X

The tuned 1D deep velocity models in the four azimuthal directions are given in Table 3.3. We determined the velocities and thicknesses of the layers especially shallower than 4-5 km. The models represent average 1D deep velocity structures between the epicenter and each station. The results show that the observed dispersion curves at frequencies between 0.07 and 0.80 Hz are affected from the layers above 4-5 km while the layers deeper than 4-5 km control the group velocity at the frequencies lower than 0.07 Hz. The comparison of the group velocity dispersion curves for the observed and theoretical ones for Rayleigh and Love waves in the tuned models are given on the right panels in Figure 3.4. The tuned 1D deep velocity structures provide a good fit for observed and calculated Rayleigh wave group velocity dispersion curves especially at frequencies higher than 0.15 Hz in the four azimuthal directions in Figure 3.4. Generally, they are slightly higher than the observed ones between 0.07 and 0.15 Hz. Theoretical Love wave group velocities for the tuned 1D deep velocity models fit well with the observed ones at frequencies larger than 0.15 Hz as shown in Figure 3.4. Since the theoretical group velocity of Love wave at 2201 is low at frequencies higher than 0.15 Hz, the model has the thick first layer in Table 3.3. The tuned Love wave group velocity dispersion curve at azimuth between 70° and 85° lower than the observed one compare to the other azimuthal directions. The tuned surface wave group velocity dispersion curves are generally in good agreement with the observed data for the frequencies between 0.15 and 0.8 Hz. Contrary to the other stations in the study area, the tuned model is the best model for Rayleigh and Love wave group velocities dispersions at Gokceada and Canakkale stations (i.e. 1714).

The Q values in the each layer are given in Table 3.3. The Q values of P-wave (Qp) were used twice of that of S-wave (Qs) from the previous studies in the Marmara Region (Mindevalli and Mitchell 1989; Sekiguchi and Iwata 2002; Horasan et al. 2002). The Q values will be used in the next chapter for the 1D simulation.

Table 3.3. Common initial model and final tuned 1D crustal velocity models for the four different azimuthal directions (A-D) between the epicenter of the 2014 Gokceada earthquake and the AFAD stations.

Layer No	Vp (km/s)	Vs (km/s)	Density (g/cm³)	Depth to the top of layer (km)	Qp	Qs
Common initial model for tuning						
1	2.16	0.78	2.1	0.00	300	150
2	2.84	1.40	2.2	0.06	400	200
3	3.50	2.00	2.3	0.26	600	300
*4	5.90	3.40	2.5	4.00	600	300
5	6.40	3.70	2.7	20.00	800	400
6	6.75	3.90	2.8	24.00	1000	500
7	8.00	4.60	3.3	34.00	1000	500
Model A: 2201 (Azimuth ~50°)						
1	2.16	0.78	2.1	0.00	300	150
2	2.84	1.40	2.2	0.40	400	200
3	3.50	2.00	2.3	1.70	600	300
*4	5.90	3.40	2.5	5.00	600	300
5	6.40	3.70	2.7	20.00	800	400
6	6.75	3.90	2.8	24.00	1000	500
7	8.00	4.60	3.3	34.00	1000	500
Model B: 5902 - 5908 - 5910 - 5907 - 5906 (Azimuth 64°-69°)						
1	2.16	0.78	2.1	0.00	300	150
2	2.84	1.40	2.2	0.10	400	200
3	4.06	2.50	2.3	0.50	600	300
*4	5.90	3.40	2.5	4.00	600	300
5	6.40	3.70	2.7	20.00	800	400
6	6.75	3.90	2.8	24.00	1000	500
7	8.00	4.60	3.3	34.00	1000	500
Model C: 1710 - 5904 (Azimuth 75°-81°)						
1	2.16	0.78	2.1	0.00	300	150
2	2.84	1.40	2.2	0.15	400	200
3	3.50	2.00	2.3	1.00	600	300
*4	5.90	3.40	2.5	4.50	600	300
5	6.40	3.70	2.7	20.00	800	400
6	6.75	3.90	2.8	24.00	1000	500
7	8.00	4.60	3.3	34.00	1000	500
Model D: 1711-1701-1713-1714 (Azimuth ~100°)						
1	2.16	0.78	2.1	0.00	300	150
2	2.84	1.40	2.2	0.10	400	200
3	3.50	2.00	2.3	0.30	600	300
*4	5.90	3.40	2.5	4.00	600	300
5	6.40	3.70	2.7	20.00	800	400
6	6.75	3.90	2.8	24.00	1000	500
7	8.00	4.60	3.3	34.00	1000	500

*: The focal layer where the rupture starting point exist.

The comparison of the common 1D initial model for all azimuthal directions with the final tuned models are given in Figure 3.5. The engineering bedrock thicknesses are thicker than the initial model (0.06 km) at each azimuthal direction 0.4 km (a), 0.1 km (b), 0.15 km (c) and 0.1 km (d). The second layer thicknesses of the models are 1.1 km (a), 0.4 km (b), 0.85 km (c). Only Canakkale stations have the similar thickness with the common initial model (0.2 km).

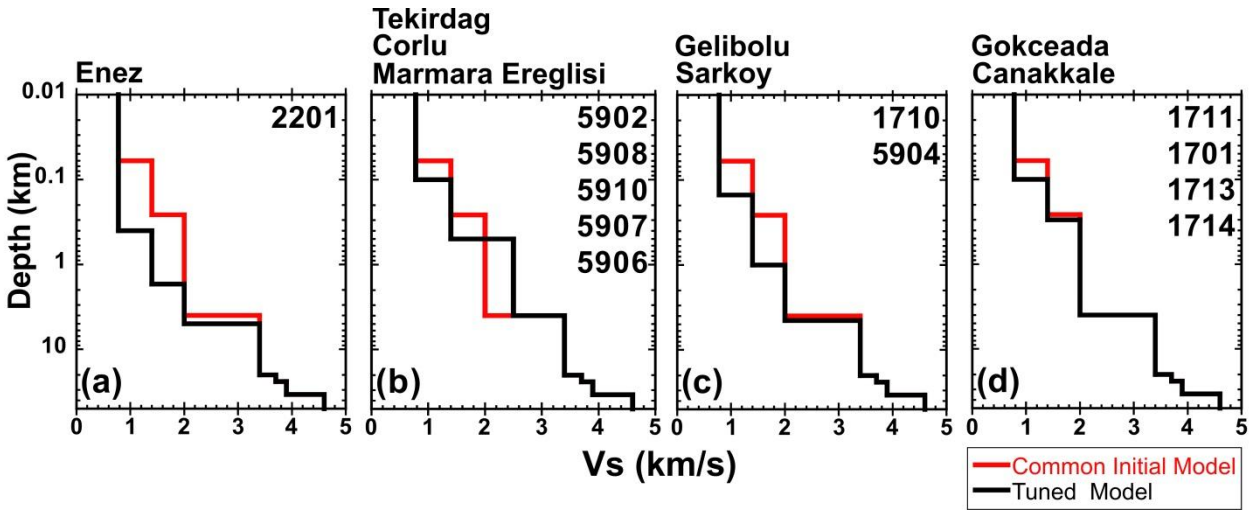

Figure 3.5 Common 1D initial velocity model (red) and tuned 1D velocity models (black) for the four different azimuthal groups.

Chapter 4

Ground Motion 1D Simulation of the 24 May 2014 Gokceada Earthquake

4.1 Characteristics of Observed Data

4.2 Discrete Wave Number Method

4.3 1D Simulation

4.4 Characterized Source Model

4.5 Comparison between Synthetic and Observed Seismograms

4.6 Discussion

4.1 Characteristics of Observed Data

The 2014 Gokceada mainshock was recorded with a sampling interval of 0.01 s at the 12 AFAD strong motion stations in the study area shown in Figure 4.1. The observed peak ground motion parameters are tabulated in Table 4.1. The acceleration records have high-frequency contents, and high peak ground acceleration (PGA) at 2201, 1701, 1713, 1710, 5904 and 5910 stations because of the possible local site effects as shown in Figure 4.1a. The significant duration defined as a time interval between 5% and 95% of an integral of a square of ground acceleration is estimated to be between 10 and 40 s for the stations except 5907.

Table 4.1 Significant duration and peak values of the observed and calculated acceleration waveforms. Remarks about approximation of 1D velocity model is given at the last column.

Station	Significant Duration (s)		Observed PGA (cm/s^2)		Observed PGV (cm/s)		Simulated PGV (cm/s)		Remarks for 1D velocity model
Code	NS	EW	NS	EW	NS	EW	NS	EW	
1711	18.6	19.1	171.4	176.6	11.0	10.1	22.8	23.1	Average
2201*	40.1	26.5	96.6	111.7	9.6	9.7	18.6	11.5	Bad
1701	27.4	30.4	141.0	121.3	12.6	15.0	5.8	8.8	Good
1713	23.9	22.5	94.4	97.5	10.6	10.8	3.6	6.8	Good
1714	29.8	32.3	45.3	51.1	5.8	4.1	4.1	6.7	Good
1710	19.0	25.9	123.2	94.4	19.2	11.1	12.9	6.5	Good
5904*	36.8	31.9	75.3	86.3	15.8	8.5	12.2	4.1	Average
5910*	14.3	15.2	77.9	107.3	8.7	6.7	6.1	2.4	Bad
5902*	12.8	14.2	68.8	64.0	6.2	7.3	6.0	2.2	Bad
5908*	17.1	18.7	45.9	39.6	8.1	4.8	6.1	2.3	Bad
5907*	87.0	73.5	25.7	25.9	4.9	8.6	5.4	2.8	Average
5906	23.3	23.8	36.4	46.9	5.2	4.2	5.5	2.3	Bad

*: Stations located on the Thrace Basin

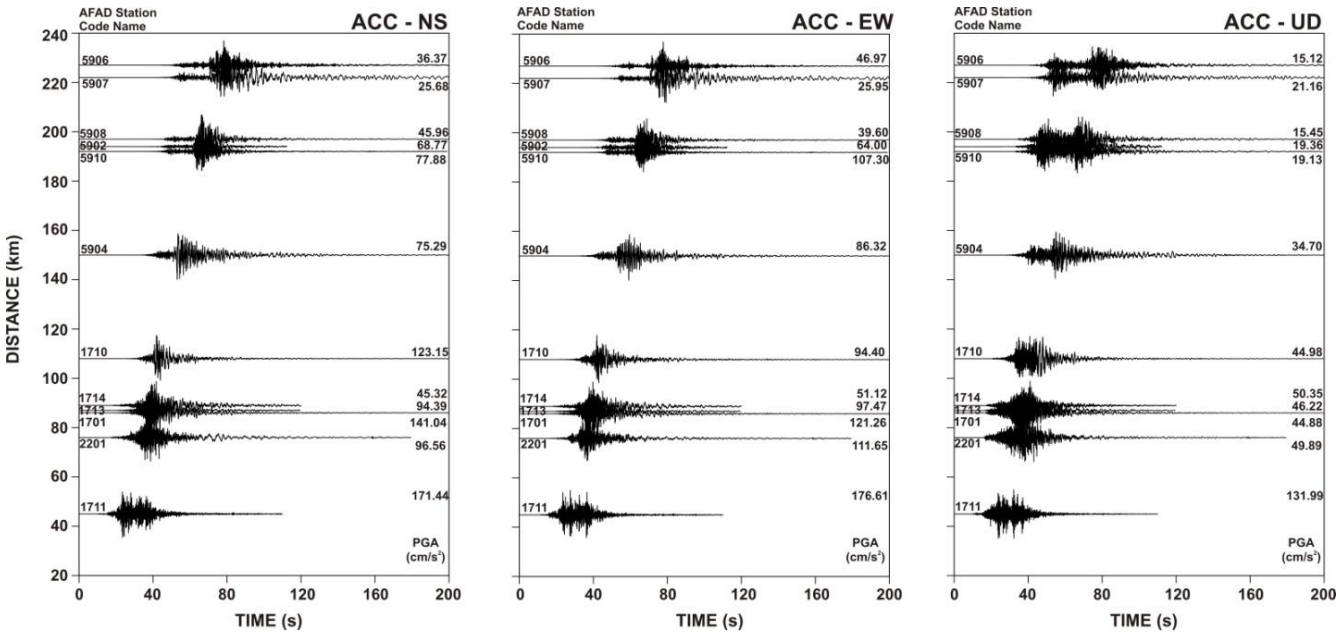

Figure 4.1 Observed acceleration records (ACC) of the 2014 Gokceada mainshock at the AFAD stations. Each waveform is normalized by its maximum value. The waveforms are plotted according to the epicentral distance. The peak values are given on the right side of the seismograms.

The acceleration spectra were smoothed with a Parzen window with a bandwidth of 0.1 Hz are given in Figure 4.2. The spectra are almost flat in a frequency range between 0.2 and 6 Hz, and spectral amplitudes decrease at frequencies more than 6 Hz. Corner frequency that is related to the source time function and source dimension is seen in the spectra at frequencies of 0.2 Hz at stations of 1711 in Gokceada, 1701, 1713, and 1714 in Canakkale city center, 2201 in Enez, 1710 in Gelibolu, 5904 in Sarkoy, 5906 in Marmara Ereglisi and at a frequency of 0.3 Hz for 5902, 5908, 5910 in Tekirdag city center and 5907 in Corlu in Figure 4.2.

The closest station of 1711 to the epicenter is located in Gokceada Island. The arrival time of P-wave is 10 s with a significant duration of the acceleration record of about 19 s. Although the spectral shapes of the stations at azimuths about 100° in Figure 4.2d are similar to each other, the station 1711 has large amplitudes at a frequency of above 2 Hz on the two horizontal components. However, its spectral amplitudes at frequencies between 0.2 and 2 Hz are lower than those at the other stations. The similar features are seen at the station of 5906 in Marmara Ereglisi in Figure 4.2b. The PGA was observed at a time of 40 s at the S-wave part while the peak ground velocity (PGV) is identified on long-period waves at a time of 75s on the NS component at 2201. This indicates the importance of long-period motion in characterizing ground motion in the area.

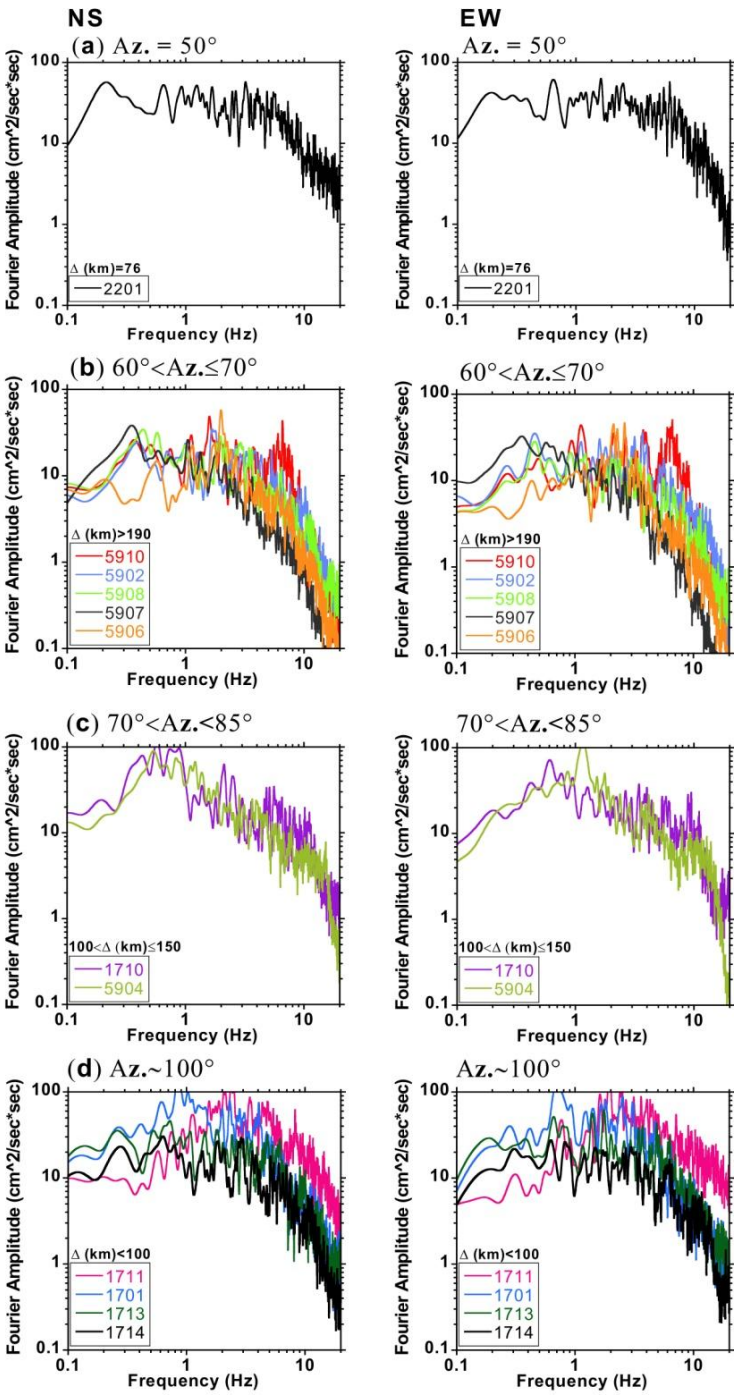

Figure 4.2 Fourier amplitude spectra of the observed acceleration waveforms. A Parzen window with a bandwidth of 0.1 Hz was chosen for smoothing. Both NS and EW components are grouped according to the azimuthal distributions of the stations. Epicentral distances of the station are given above the legends. (a) Enez (b) Tekirdag city center, Corlu and Marmara Ereglisi, (c) Gelibolu and Sarkoy (d) Gokceada and Canakkale city center.

The two stations (1710 and 5904) in the similar azimuth have dominant high amplitudes at frequencies between 0.3 and 1 Hz. These spectral characteristics at the two stations might have been caused by S-wave radiation dominant in this azimuth that is close to the strike of the fault (75°). The clear peaks at 5904 are very dominant at a frequency of 1.4 Hz in the spectra of the two components.

The acceleration record of 5907 shows significant durations for the NS and EW components as 87 and 74 s, respectively, because the low frequency phases are clearly seen on both acceleration (Figure 4.1) and velocity seismograms (Figure 3.1 in Chapter 3). The spectral amplitudes at high frequencies are low as compared to the other stations due to strong attenuation in thick sediments of Thrace Basin in Corlu near the station (Siyako and Huvaz, 2007).

The acceleration record at 5910 in Tekirdag city has large and distinct amplitudes at a frequency of 6-7 Hz, which is different from the other stations in this azimuthal group. Therefore, it can be suggested that the high amplitudes at frequencies between 3 and 10 Hz are caused by shallow soil amplification because this feature can be seen only at this station (Figure 2.17 in Chapter 2).

In order to simulate these features, surface wave group velocity dispersion analysis for 1D deep structural modeling in Chapter 3 was conducted and the 1D S-wave amplifications at the AFAD stations given in Chapter 2.

4.2 Discrete Wave Number Method

The ground velocity seismograms in this study were obtained using wavenumber-frequency integration code that is a combination of wave propagation and elastic crustal velocity model for simulation, developed by Takeo (1985) and slightly modified by Kikuchi (2005). The method includes three-dimensional seismic wavefield of Aki and Richards (1980), the reflection and transmission properties of elastic media of Kennet and Kerry (1979) and discrete wave number integration of Bouchon (1981) (Dhakal et al., 2009). The DWNM was firstly introduced by Bouchon and Aki (1977), and later Bouchon (1979, 1981). It is one of the most powerful methods to represents a wave field composed of a stack of irregular layers (if there is no strong heterogeneities) that is radiated from the seismic source and travels in layered media (AIJ, 1993,

Part III, at p: 346). The method uses spatial periodicity of sources to discretize the radiated wave field in the complex frequency domain and Fourier transform to calculate Green's functions for a horizontally layered 1D velocity structure due to a double-couple point source with particular focal mechanism and source time function at a given distance and azimuth (Bouchon and Aki 1977).

Determination of Green's function for a real crustal medium is difficult because of complications and heterogeneous structure of the Earth. It is defined as the response of the medium to a unit impulsive force (double couple) in space and time domain. Green's functions behave as a propagator of the effects of seismic force acting on the fault plane to determine elastic displacement at any point in the medium. The most accurate results for the response of medium can be obtained by the DWNM (AIJ, 1993, Part III, at p: 245) that computes Green's functions for a layered 1D crustal structure using vertical SH waves as an input motion. The simplest case, vertical SH-wave is incidence because the SH-wave field has only one degree of freedom at one point, and no mode conversion takes places (this means direct, reflected, transmitted and diffracted waves same).

The DWNM is based on the seismic wave equation solution in length space and frequency domains for assumed elastic, isotropic, and homogeneous 1D multilayered crustal structure. Seismic waves propagate spherically and symmetrical from source. Wave number integration can be represented exactly discrete summation for any time zone. This discretization can be obtained by adding the set of infinite circular source that scattered equal radial distance according to a designated source. The choice of this distance is up to designed time point source response and it defined the discrete horizontal wavenumber. Definition of maximum and minimum wavenumber related to the highest and lowest phase velocities in the medium.

Definition of the maximum wavelength (L) using in the DWNM is one of the most important points. This is also called Bouchon's criteria and defined as follows,

$$L / 2 > r$$

$$(L - r)^2 + h^2 \geq (Vp * t)^2$$

where *r* and *h* is the epicentral distance (km) and source depth (km), respectively. *Vp* is the maximum P-wave velocity (km/s) in the source region and *t* is the seismogram length in seconds. Both criteria must be ensured. If the *L* is chosen smaller than that the given criteria, numerical errors occur and may not be clearly seen in the seismograms. Another important point is the discretization segment number (spatial periodic sources) between the source and station. Although a high numbers of segments cause to generate more accurate seismograms, the calculations take much time. Therefore, a proper segment number should be chosen for effective calculation.

There are several advantages of the DWNM. It is widely used in crustal studies because body and surface waveforms can be fully generated. Waveforms are obtained in wave number domain and converted to time series using inverse Fourier transformation. Using complex frequency values in calculations eliminates aliasing in the time domain generated by using discrete Fourier transformation with infinite source array (Bouchon, 1979). Therefore, the method gives complete solution with high accuracy for numerical wave number integration for response of the medium with a minimum amount of mathematics and less calculation time compare to the other methods (i.e. finite element or finite difference methods).

On the other hand, there are also disadvantages of the method. The maximum wavelength and number of calculation segments between the source and station must be determined carefully. The Bouchon's (1981) criteria are must be strictly applied.

4.3 1D Simulation

The numerical procedure of the ground motion simulation is given by flow-chart in Figure 4.3. An appropriate 1D velocity structure and a characterized source model (CSM) are necessary inputs for the 1D simulation. The source parameters of the mainshock were estimated in following ways based on previous studies about the 2014 Gokceada earthquake and the strong motion simulation recipe by Irikura and Miyake (2011). The DWNM was used to obtain the response of the 1D deep velocity models that are given in Chapter 3.

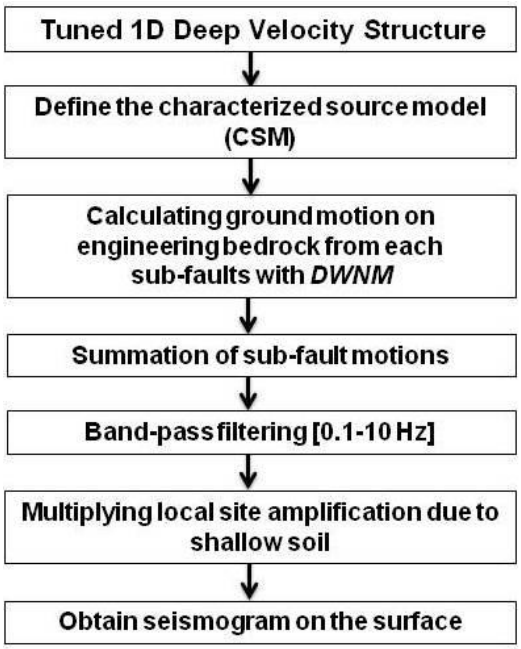

Figure 4.3 Flow chart of the 1D simulation of the 2014 Gokceada earthquake.

In this study, it is assumed that the fault area consists of several sub-faults, which are treated as point sources to generate rupture propagation effects. A seismogram on the engineering bedrock of each sub-fault was calculated with the DWNM using the CSM and the tuned 1D deep velocity structure with pre-defined Q values in Chapter 3. The sampling rate of the each synthetic seismogram was chosen as 0.05 s and the Nyquist frequency of 10 Hz considering the interested frequency range. After generating seismograms for all the sub-faults, the point source summation technique with rupture times defined from rupture velocity was performed to get the synthetic waveform on the engineering bedrock in the time domain. Zaineh et al. (2013) examined that the sample spacing between sub-faults was chosen as small as possible to improve accuracy until synthetic motions converged to a stable value in the point source summation procedure.

1D linear amplifications of the shallow soil models are given in Chapter 2 were used to estimate the surface motions from the engineering bedrock motions at the 12 AFAD stations. The engineering bedrock motions were filtered between 0.1 and 10 Hz, and their amplitude spectra were divided by two to omit free-stress effect for input waves to the shallow soil models. Then,

they were multiplied by the 1D site amplification in the frequency domain. Finally, the inverse fast Fourier transform was applied to obtain the surface motion in the time domain.

4.4 Characterized Source Model

The assumed fault parameters are given in Table 4.2 from the following considerations. Pinar (2014; pers. Comm.) determined the focal mechanism solution and slip distribution of the Gokceada earthquake using teleseismic waveform inversion method by Kikuchi and Kanamori (1991). He used teleseismic broad-band P waveforms at 30 stations with epicentral distance (Δ) change between $30° \leq \Delta \leq 90°$ obtained from the Global Digital Seismograph Network (GDSN). He estimated seismic moment of each sub-fault distributed along the strike and dip of the ruptured fault plane (Figure 4.4a). The best inversion solution shows the strike, dip and rake angels are 75°, 73° and -143°, respectively. The solution implies a right lateral faulting with normal component (Figure 4.4a; Table 4.2). The depth of the earthquake was found as 7.5 km, and the total seismic moment (M_0) was calculated as 2.87×10^{26} dyne.cm (Mw 6.9). The average slip (Dave) on the fault is 0.83 m. The finite source modeling of the teleseismic waveforms yields a rupture area of 100x12.5 km^2 size for the 2014 Gokceada mainshock. This area is matched with the observed aftershock distribution M $\geq$1 within 3 months (see Figure 1.3 in Chapter 1). To obtain the slip distribution, the sub-faults size was chosen as 10 km along the strike and 5 km along the dip of the fault plane. The rupture of the each sub-fault was modeled using a source time function that contains 9 triangles with 8 s of rise time (Figure 4.4a). The rupture initiation time of each sub-fault was calculated according to the starting point that located at the center of the fault area with a slow rupture velocity of 2.0 km/s. The source rupture duration was approximately 30s. The final slip distribution with 0.2 m interval counters is given in Figure 4.4a. The maximum displacement is about 1.8 m on the fault area. According to the slip distribution, there are three areas with high slip value. Two of them have the largest seismic moment release and are located NE part of the fault area. The third one is close to the rupture initiation point with relatively small slip value.

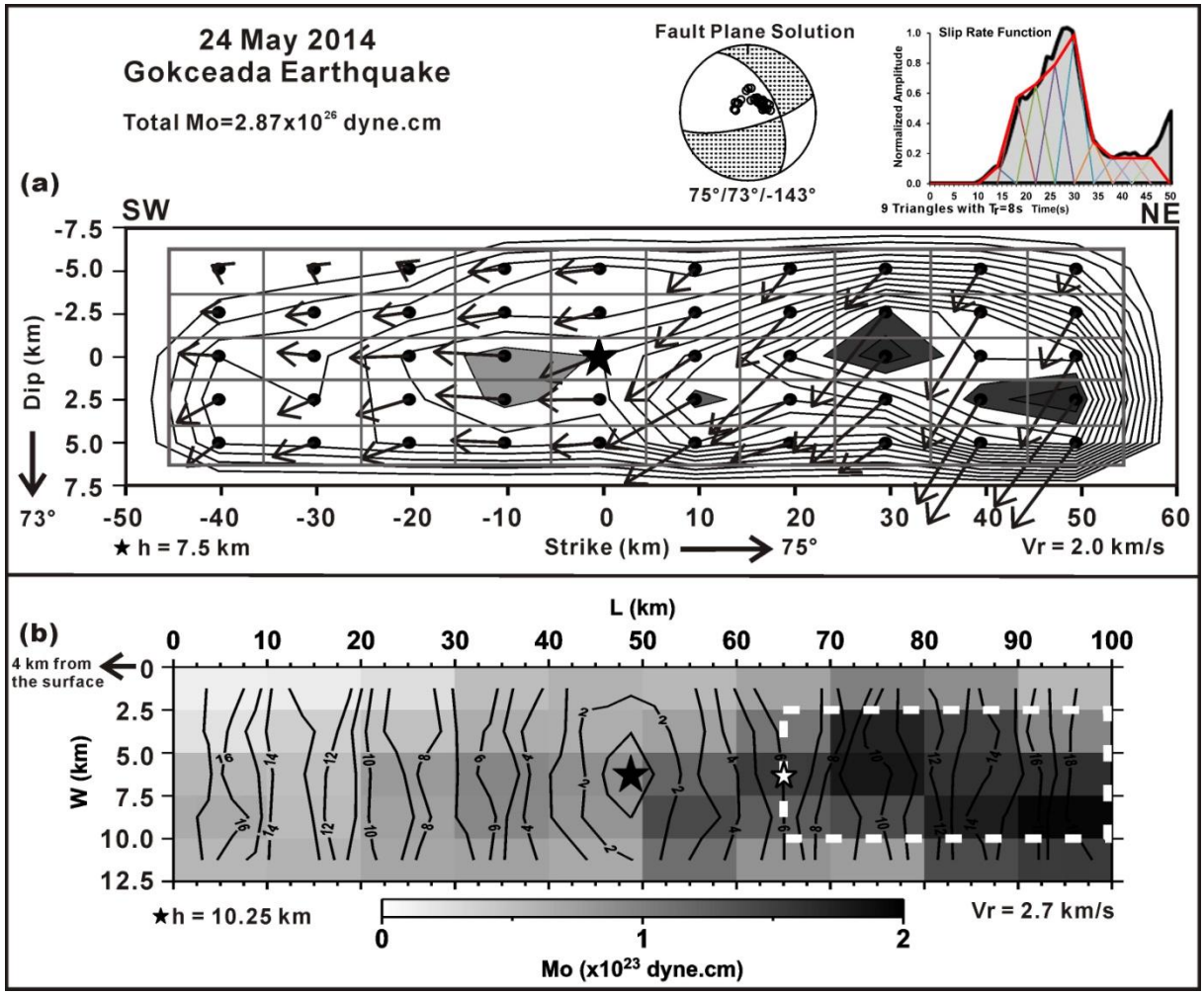

Figure 4.4 a) Focal mechanism solution and source time function are shown on the top right, slip distribution of the 2014 Gokceada earthquake obtained using finite fault modeling by Pinar (2014). Slip distribution counter intervals are shown by 2 cm and maximum displacement is about 1.8 m. The focal depth shown with black start is 7.5 km. b) Characterized source model for the 2014 Gokceada earthquake in this study. The seismic moment distribution of Pinar (2014) is shown with the shaded background. The black star shows the hypocenter proposed in Pinar's (2014) slip model and locates at the depth of 10.25 km. The top of the fault area is 4 km from the surface. The white dashed rectangle is the asperity area. The small white star indicates the rupture starting point for the asperity. The black contours are rupture front times (seconds) for the background.

Table 4.2 Source parameters of the 2014 Gokceada earthquake. Pinar: Slip distribution model is given by Pinar (2014, and per. comm.), 1-ASP Model: Characterized source model with one asperity. N and M describe the number of sub-faults along strike and dip on the ruptured fault area, respectively. No and Mo represent the sub-fault number that rupture starts.

Fault Parameters	**Pinar's Model**	**1-ASP Model**	
		Background (BG)	**Asperity (ASP)**
Fault size (L (km) x W (km))	100x12.5	100x12.5	35x7.5
Number of Sub-faults (N x M)	10 x 5	40x5	56x12
Rupture start sub-fault no (No x Mo)	5x 3	20 x 3	1x6
Sub-fault Size (km x km)	10 x 2.5	2.5x2.5	0.625x0.625
Fault top (km) from surface	1.25	4	6.5
Seismic Moment (dyn.cm)	$2.87x10^{26}$	$1.83x10^{26}$	$1.04x10^{26}$
Rigidity (dyn/cm²)	3.0×10^{11}	2.77×10^{11}	
Source Time Function Type	9 Triangle	Smoothed ramp velocity	Kostrov-like slip-velocity
Rise Time (s)	8	1.34	1.39
Average Slip (Dave) (m)	0.83	0.53	1.43
Average Stress Drop (MPa)	1.58	1	5.96
Sample rate (Δt)(s)	1	0.05	0.05
Rupture Velocity (km/s)	2.0	2.7	
Slip Ratio (Dave/Dbg)	-	1.7	
Focal depth (km)	7.5 (centroid)	10.25 (focal depth)	
Strike/Dip/Rake (°)	75°/73°/-143°	75°/73°/-143°	
Epicenter (°N/°E)	40.32°/25.47° (KOERI)	40.29°/25.39° (USGS)	

The slip distribution by Pinar's (2014) with using a smoothed ramp function as source time function (STF hereafter) by using the 1D simulation method has been tested. It turned out that the slip distribution obtained from the low frequency teleseismic waveforms was inadequate to generate high frequency ground motions with only fault area. Therefore, we needed to define strong motion generation area that characterizes the rupture with large slips on the fault. A characterized source model was proposed utilizing a method of Irikura and Miyake's recipe (2011) and the slip distribution model of Pinar (2014) to increase ground motions at high frequencies. The fault model consisted of one asperity (ASP) area with the high slips and background (BG) area with the low slips by a white broken line as shown in Figure 4.4. The details of the source parameters are given in Table 4.2. The epicenter coordinates by USGS were used for the rupture starting point at the center of the fault area, because it was calculated by using more stations than that of a local network in the area. The depth of the top of the BG area was set to be 4 km to obtain the focal depth as 10.25 km as reported by USGS (11 km) as shown in Figure 4.4.

It is known that defining a point source for a large earthquake that ruptures hundreds of kilometer-square fault area does not give enough resolution for calculation of near-field ground motion records. Therefore, parameterization of the fault area with several point sources (sub-faults) located on a grid is one of the widely used methods in ground motion simulation studies (i.e. Heaton and Helmberger 1979; Archuleta and Hartzell 1981). Therefore, the BG and ASP areas were divided into several sub-faults that were assumed as double-couple point sources at their centers. The BG area was 1250 km^2 and is divided into 200 equal sub-faults areas with sizes of 2.5 x 2.5 km^2. The seismic moment of each sub-fault was calculated from the corresponding slip value from Pınar's (2014) model. A smoothed-ramp velocity STF was used for the BG. The rise time (T_R) for the STF of each sub-fault in the BG area was calculated with the empirical equation given by Somerville et al. (1999):

$$T_R=2.03x10^{-9}xM_o^{1/3}$$

where M_o is the total seismic moment of the earthquake in dyne.cm.

The location and size of the ASP area were determined by principally considering the sub-faults with the high seismic moment release in Figure 4.4. The ratio of the area of the ASP to the BG areas was also taken into account to be 22% (Somerville et al. 1999; Dalguer et al.

2004; Irikura and Miyake 2011). The seismic moment of the ASP area was calculated from the moment summation of the corresponding sub-faults. Therefore, the BG and the ASP have ~64% and ~36% of the total seismic moment. The average slip ratio of the BG to the ASP areas was 1.7, smaller than the empirical ratio (2.3 for one ASP model) given by Dalguer et al. (2004). The average stress drops on the BG and the ASP areas were set to 1.0 and 5.96 MPa, respectively, using the circular fault crack formulation by Eshelby (1957) and Brune (1970, 1971).

The ASP area was divided into the sub-faults with the size of 0.625 km. The size of the sub-faults was determined considering the results of the simulation by Zaineh et al. (2013). To generate high frequency motions in the seismograms, the Kostrov-like slip-velocity function was used with the targeted maximum frequency (*fmax*= 6 Hz) that was identified in the spectra of the acceleration records in Figure 4.2. The rise time of the STF in the segments of the ASP area was calculated by an empirical relationship given by $T_R=Wa/2V_r$ where *Wa* is the width of the ASP and V_r is the rupture velocity (Nakamura and Miyatake, 2000). The constant rupture velocity over the fault area was taken as 2.7 km/s assuming 80% of the S-wave velocity in the focal layer. The circular rupture front was assumed according to the hypocenter location. Additionally, incoherent random fluctuation (Δt_r) was added to the homogeneous circular rupture front time (t_r) to increase high frequency amplitudes of synthetic seismogram (i.e. Das and Aki 1977).

The incoherent random fluctuation was calculated using uniformly distributed random numbers (*rnd*) in a range of ±1 s that corresponded to 1/20 of the total rupture time of 20 s described by Hisada (2000). The Δt_r was calculated for BG as

$$\Delta t_r = t_r * rnd * 0.2 \quad ; tr < 5\ s \quad (1)$$

$$\Delta t_r = rnd \qquad ; tr \geq 5s \quad (2)$$

To prevent generating negative rupture times in the BG because of the random numbers, we introduced equation (1) for the first 5 s of the rupture and the later times were calculated with equation (2). The rupture time of a sub-fault (t_r') in the BG was

$$t_r' = t_r + \Delta t_r$$

On the other hand, the sub-fault sizes of the ASP were too small respect to the BG and we scaled the random numbers by a coefficient (q) considering the sub-fault size (dx) and V_r to obtain the incoherent random fluctuation of the ASP (Δt_{ra}) as

$$q = dx / V_r$$

$$\Delta t_{ra} = q * rnd$$

This scaling prevented to rupture of a sub-fault later than the next neighboring sub-fault. The rupture time of a sub-fault (t_{ra}') in the ASP was calculated as

$$t_{ra}' = t_{ra} + \Delta t_{ra}$$

The rupture time contours for the BG and the ASP are shown in Figure 4.5. Since the total rupture duration in the fault of about 20 s is in agreement with observed significant duration (~19 s) of the closest station of 1711, and the assumption of the rupture velocity can be acceptable in our simulation.

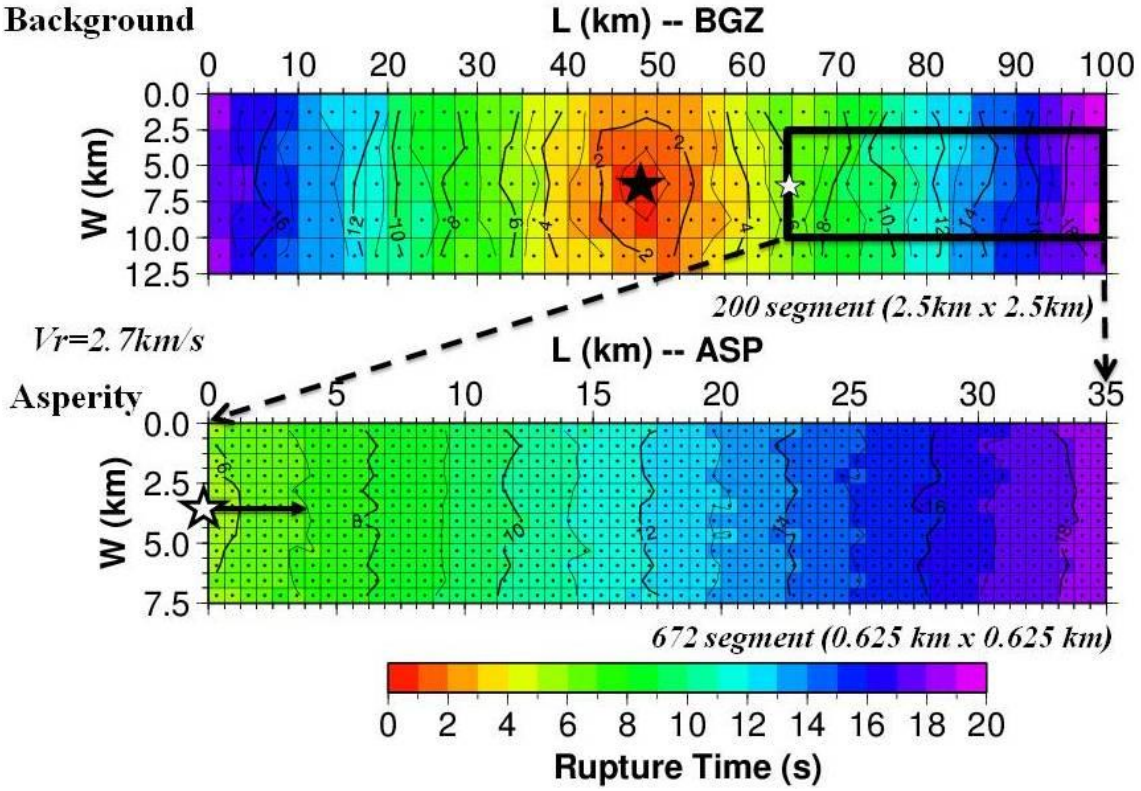

Figure 4.5 Rupture front times (seconds) for the background (top) and asperity area (bottom). The black and white stars are the rupture starting point for the BG and ASP, respectively. The grid cells show sub-fault of the ruptured area. The rupture front time at each sub-fault is shown by different colors and time contours are also given in seconds.

4.5 Comparison between synthetic and observed seismograms

We compared the synthetic velocity waveforms on the surface and their spectra at the strong motion stations from the 1D simulation using the above-mentioned model of the fault and subsurface structures including the shallow soil structures with observed ones in Figures 4.6 and 4.7. The PGVs of the observed and the synthetic seismograms are given at the right top of each plot in Figure 4.6 and Table 4.2 for the two horizontal components. The results of 1D simulation at the stations were remarked as “good”, “average” or “bad” in the last column in Table 4.1 according to the comparison of the observed and synthetic waveform shapes and their spectral contents. Good refers to the simulated and observed waveforms are in good agreement for arrival time, the general shape of the waveforms and spectra at the sites (i. e 1701, 1714). Average indicates that the simulated and observed waveforms have an average agreement with general shape of the waveforms. The spectra are not match at all frequencies. The spectra of either NS or EW components show a good match. Generally, high frequency parts of spectra show a good match between synthetic and observed waveforms (1711, 1710, 5904). Bad is used for the sites that have difficulties for matching waveforms at especially low frequencies with high amplitudes due to a local basin structure or long epicentral distance (>150km).(i.e 2201, 5908, 5910).

The synthetic arrival times of the body and surface waves are similar to the observations because our subsurface models have been constructed from the surface wave group velocity dispersion analyses. The P-wave travel time of 10.5 s in the synthetic motion at 1711 is in good agreement with the observed one of 10.0 s as shown in Figure 4.6a. The comparisons between the two horizontal components of the synthetics and the observed waveforms in Figure 4.6a-b clearly show that the travel times of the major phases in the synthetic waveforms fit with the observed ones at all stations. Although the synthetic velocities at the station 2201 located close to the epicenter have similar amplitudes as the observed ones, the large observed Rayleigh wave on the NS component at an arrival time of 65 s is not well reproduced in the 1D simulation.

The observed and the synthetic ground motions have a good match in the arrival times of major body and surface waves at 1701, 1713, and 1714 in Canakkale city center. Especially, the synthetic waveform of the EW component at 1713 at times between 35 and 70 s is in

agreement with the observed one. The synthetic waveforms at 1710 in Gelibolu are qualitatively similar to the observation with slight differences of the amplitudes of low-frequency surface waves at travel time of 60 s in the NS component. The synthetic ground motions at the stations with the epicentral distances longer than 150 km in Tekirdag city center, Corlu and Marmara Ereglisi (5910, 5902, 5908, 5907 and 5906) contain the dominant low-frequency waves between 0.1 and 0.2 Hz that are over-estimated in the 1D simulation. One of the reasons may be generation of trapped waves in the sub-surface layers with the large velocity contrast. The assumed Q values in the models may also be a reason because the attenuation of low frequency synthetic waves. There is no information about frequency depended Q values for the crust in the study area.

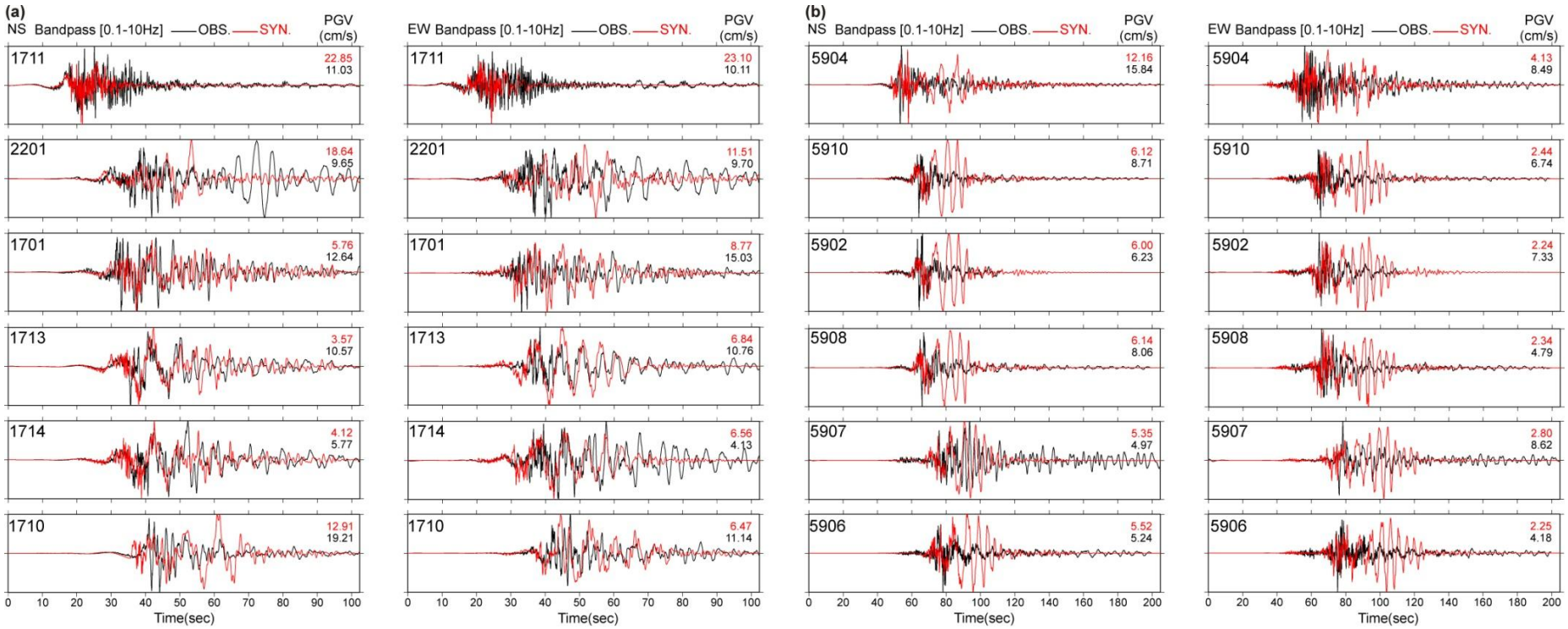

Figure 4.6 Comparison of the observed (black) and simulated (red) velocity waveforms of the Gokceada earthquake. Observed velocity waveforms were calculated by integration in the frequency domain with filtering between 0.1 and 10Hz. The NS and EW components are given left and right, respectively. The amplitudes are normalized, and the maximum peak values (cm/s) are given in the right top of each plot. (a) Gokceada, Enez, Canakkale city center, Gelibolu stations (b) Tekirdag city center, Corlu, Marmara Ereglisi stations.

The comparisons of the spectra are displayed in Figure 4.7. The predominant (f_{prd}) and fundamental (f_0) frequencies, which were obtained from the site amplifications given in Figure 2.17, for the sites, are shown with inverted red triangles on the spectra in Figure 4.7.

The synthetic spectral shapes of the two horizontal components at 1711 are in good agreement at a frequency of above 1Hz. This indicates the sufficient capability of our model of the fault and the 1D subsurface structure to generate the high-frequency motions.

Our shallow soil models indicate the site amplification with the dominant fundamental frequencies at the stations of 1711, 1713, 1714 and 5907 as shown in Figures 2.17b, d. However, such peaks cannot be found in the spectra of the observed motions. Probably the source effects can be much more dominant than the local amplification due to the shallow soil.

The maximum site amplification factors at the predominant frequencies given in Figure 2.17 are identified in the spectra of the stations 2201, 1701, 1714, 1710, 5904 and 5908. The dominant peaks are seen only in the observed spectra at 1701 and 5904 at the similar predominant frequencies of 0.85 and 1.4 Hz, respectively. Therefore, the amplification characteristics of both sites obtained from microtremor studies in Figure 2.17c, d are appropriate for the simulation.

The distinct peak at the fundamental frequency at 5902 cannot be distinguished on the observed spectra of the NS and EW components. The site amplification at the fundamental frequency of 3.5 Hz at this site has a value of ~3 given in Figure 2.17b. Therefore, it is not clearly seen on the synthetic motions. On the other hand, the site amplification factor of ~6 at the predominant frequency of 3.5 Hz is seen in the synthetic spectrums of the horizontal components at 5908. Although a dominant peak at the frequency of 2 Hz in the observed spectra at 5906 can be identified in the site amplification from microtremor array exploration (see Figure 2.17b), this peak cannot be clearly seen on the synthetic spectra. This may be caused by low amplitudes of the engineering bedrock motion at the frequency of 2 Hz.

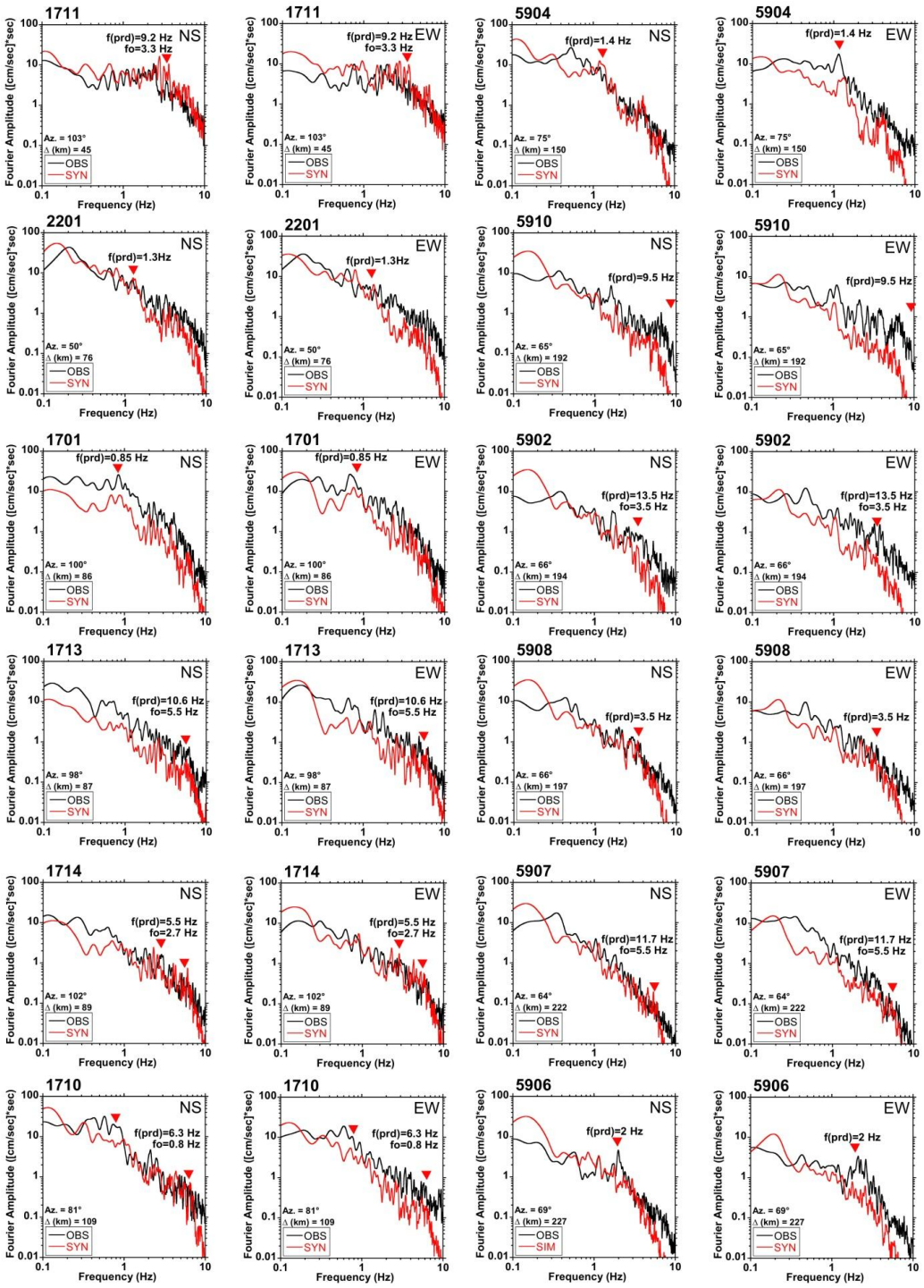

Figure 4.7 Comparison of the amplitude spectrums of the observed (black) and synthetics (red) velocity waveforms. f (prd) and f_0 are the predominant and fundamental frequencies that were obtained from site amplifications given in Figure 2.17, respectively, are shown by red inverted triangles. (a) Gokceada, Enez, Canakkale city center, Gelibolu stations (b) Tekirdag city center, Corlu, Marmara Ereglisi stations.

4.6 Discussion

Our simulation well reproduced the high frequency parts of the waveforms at most of the stations. This clearly indicates the importance of the introduction of a proper asperity area with Kostrov like slip-velocity function, fluctuating rupture front time and local site effects at individual observation sites. The low frequency parts of the spectra of the synthetic motions are generally higher than the observation between the frequency of 0.1 Hz and the corner frequency (0.2 and 0.3 Hz) at most of the stations. The synthetic ground motions in this frequency range were affected by the fault model and 1D deep velocity structures. However, our fault model was established considering the results of the inversion using low-frequency teleseismic data. It is therefore suggested that the high amplitudes on the low-frequency part of the spectra can be caused by inappropriateness of the deep part of the 1D velocity structures at the sites such as 2201, 5910, 5902, 5908, 5906 and 5907. Actually the results of the surface wave group velocity dispersion analyses indicate that the theoretical group velocity is higher than the observation at frequencies from 0.07 to 0.15 Hz at some of the stations. Therefore much more careful tuning is required in building of a 1D deep S-wave velocity model at each strong motion station.

This study provides 1D S-wave velocity structural models at the strong motion stations to calculate reliable synthetic ground motions of the 2014 Gokceada earthquake. These subsurface models can be effectively used in prediction of strong ground motion due to future large earthquake along the NAFZ in the Marmara Sea. However, it must be noted that there are failure cases of the 1D simulation if there is a different local structure around the station. For example, the Rayleigh wave with slow group velocity of ~1.2 km/s at frequency of ~0.2 Hz at an arrival time of 65 s was not generated in the 1D simulation at 2201 in Figure 4.6a. The wavelength of the surface wave is about 6 km. Dalyan Lake in Meric delta exists along the propagation path to the site in Enez, having a width of ~1.7 km (Figure 4.8). Furthermore, Siyako and Huvaz (2007) proposed a 5km-thickness of the sediments in the region (Figure 4.9). Consequently, this slow Rayleigh wave package may be formed because of the effect of the thick sedimentary layers of the Meric Delta and Thrace Basin. This clearly indicated the difficulty of the 1D simulation for low-frequency surface waves affected by local sedimentary layers. Such local effects can also be

seen in our results of the 1D simulation for stations with the epicentral distances longer than 150 km. The locally generated surface waves can be seen on the synthetic waveforms of Tekirdag (5902, 5908, 5910), Corlu (5907) and Marmara Ereglisi (5906) stations. Contrarily to the other Tekirdag stations, surface waves were recorded on the NS component of 5907 in Corlu and we obtained a good fit between observed and synthetic waveforms (see Figure 4.6b). The observed surface waves at 5907 may be generated by 2D or 3D basin effects because Corlu city is settled on the sediments of the Thrace Basin with a thickness of ~7 km given by Siyako and Huvaz (2007) in Figure 4.9. The site located on the Oligocene and Miocene young units that contain mostly sandstone, siltstone and clay stone (Figure 4.9b and Figure2.2 in Chapter 2). The sites located on the thick sediment part of the Thrace Basin show a tendency to generate the low frequency synthetic waveforms with high amplitude in 1D Simulation.

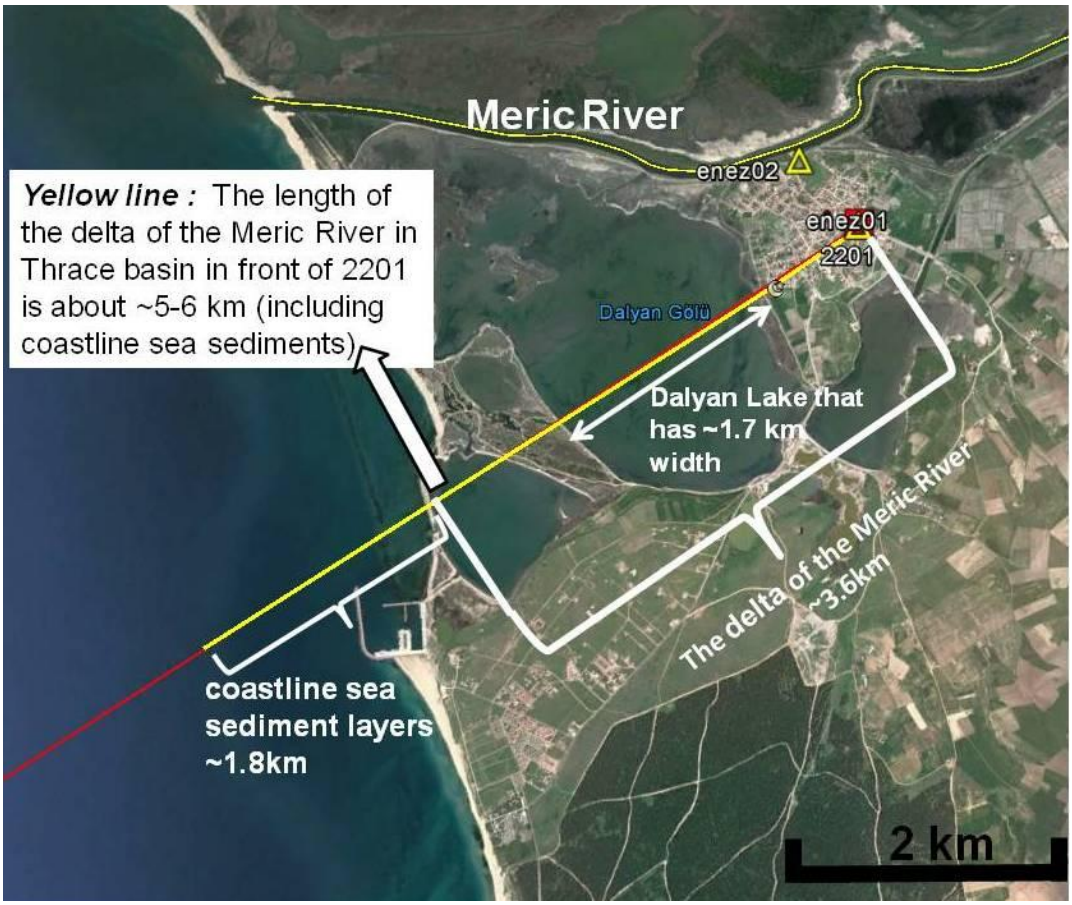

Figure 4.8 Satellite view of the Meric Delta in front of the Enez station (2201) on the Google Earth. The length of sediment area (Dalyan Lake and sediments in the sea) in Meric Delta is shown.

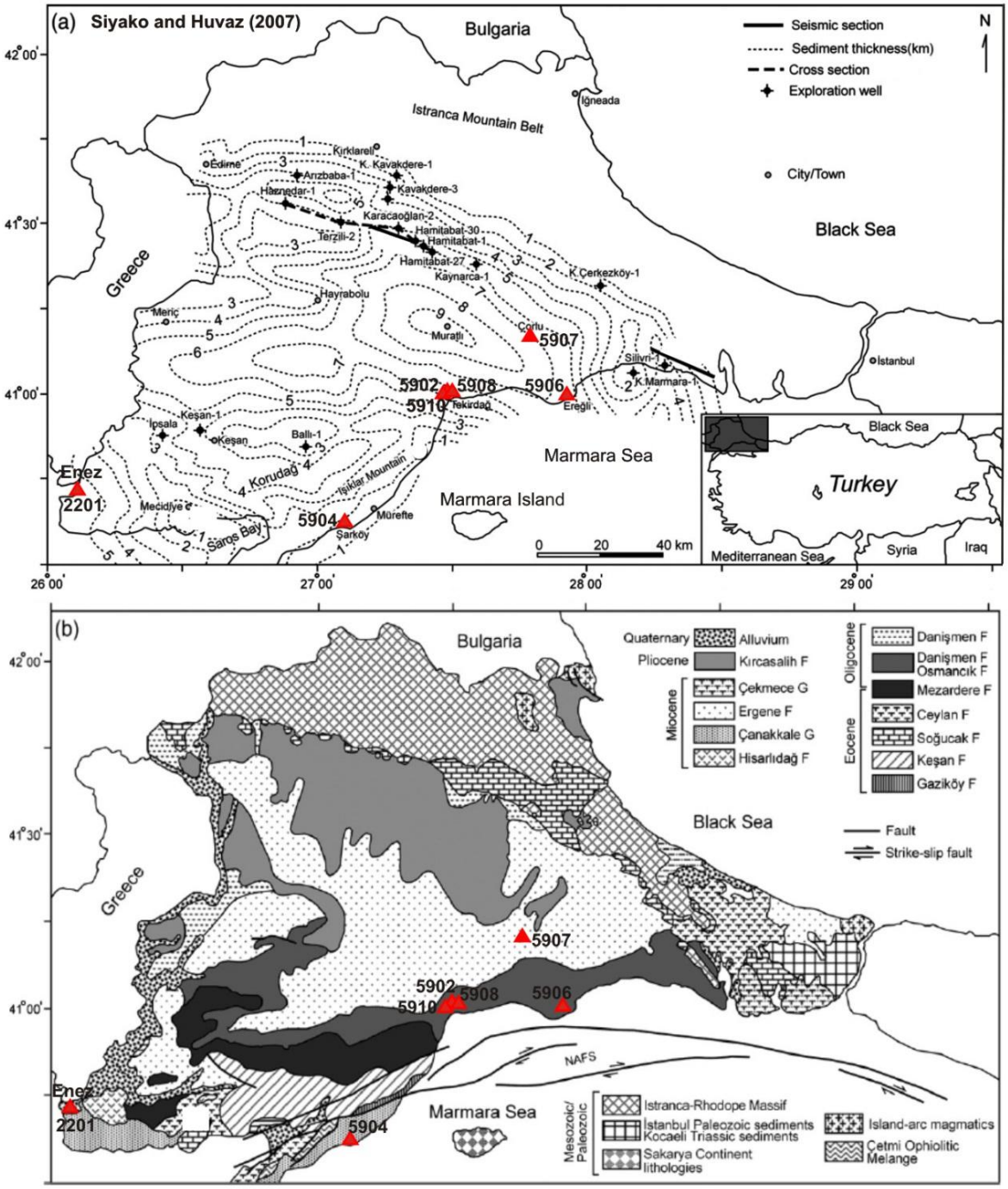

Figure 4.9 Sediment thickness map (a) and geology map of the Thrace Basin (NAFS: North Anatolian Fault System) given by Siyako and Havuz (2007). Red triangle shows the AFAD station location.

Chapter 5

Estimation of Strong Ground Motions of the 9 August 1912 Murefte Earthquake

5.1 Site Selection Criteria

5.2 Determination of Characterized Source Model

5.2.1 Outer Fault Parameters

5.2.2 Inner Fault Parameters

5.2.2.1 Model A

5.2.2.2 Model B

5.2.3 Decision of the Final Source Model

5.3 Near-Fault Response Spectra of the Ground Motions

5.3.1 Simulated Waveforms of the Selected Near-Fault Sites

5.3.2 Response Spectra of the Ground Motions

5.4 Discussion

5.1 Site Selection Criteria

The sites where the synthetic seismograms were generated for the 1912 event were selected taking into account the trend of the long axis of the intensity contours among the strong ground motion stations discussed in Chapter 4. These sites have probably high ground motions according to the damaged locations defined by Ambraseys and Finkel (1987) on the soft soils. The intensities of 1912 earthquake were given in the Medvedev-Sponheuer-Karnik (MSK-1981) scale by Ambraseys and Finkel (1987). The MSK scale is very similar to the Modified Mercalli Intensity (MMI) scale (Panza, 2005). Two sites are located in the intensity IX, four sites are between VIII and IX, one site is located in the VII-VIII. Figure 5.1 shows the selected sites on the map with digitized intensity contours and damaged locations from Ambraseys and Finkel (1987). The intensity of the selected site was determined from the damage value of the site. Because intensities are given in Roman numbers, determining the exact value of the intensity value at a site located between two intensity counters is difficult. Therefore, the damage ratios (0-9) given by Ambraseys and Finkel (1987) near the selected sites were used to approach the integer intensity value. If the damage ratio of a site located in two intensity contours is lower than the average damage ratio of the near surrounding sites, the lower intensity value was assigned to the site. If the ratio is higher than the average, the higher intensity value was assigned. The details of the selected sites are given in Table 5.1.

Table 5.1 Site location, epicentral distance, azimuth, damage and intensity information of the selected sites for the 1D simulation of 1912 Murefte earthquake.

Station Code	Site Location	Epicentral Distance (km)	Station Azimuth (°)	Damage Ratio no	Intensity (MSK)
5904	Sarkoy	12	208	5	IX
1710	Gelibolu	55	234	1	IX
1713	Canakkale	90	227	1	VIII
1711	Gokceada	124	242	1	VIII
5908	Tekirdag	45	42	0	VIII
5907	Corlu	71	45	3	VIII
5906	Marmara Ereglisi	69	65	3	VIII

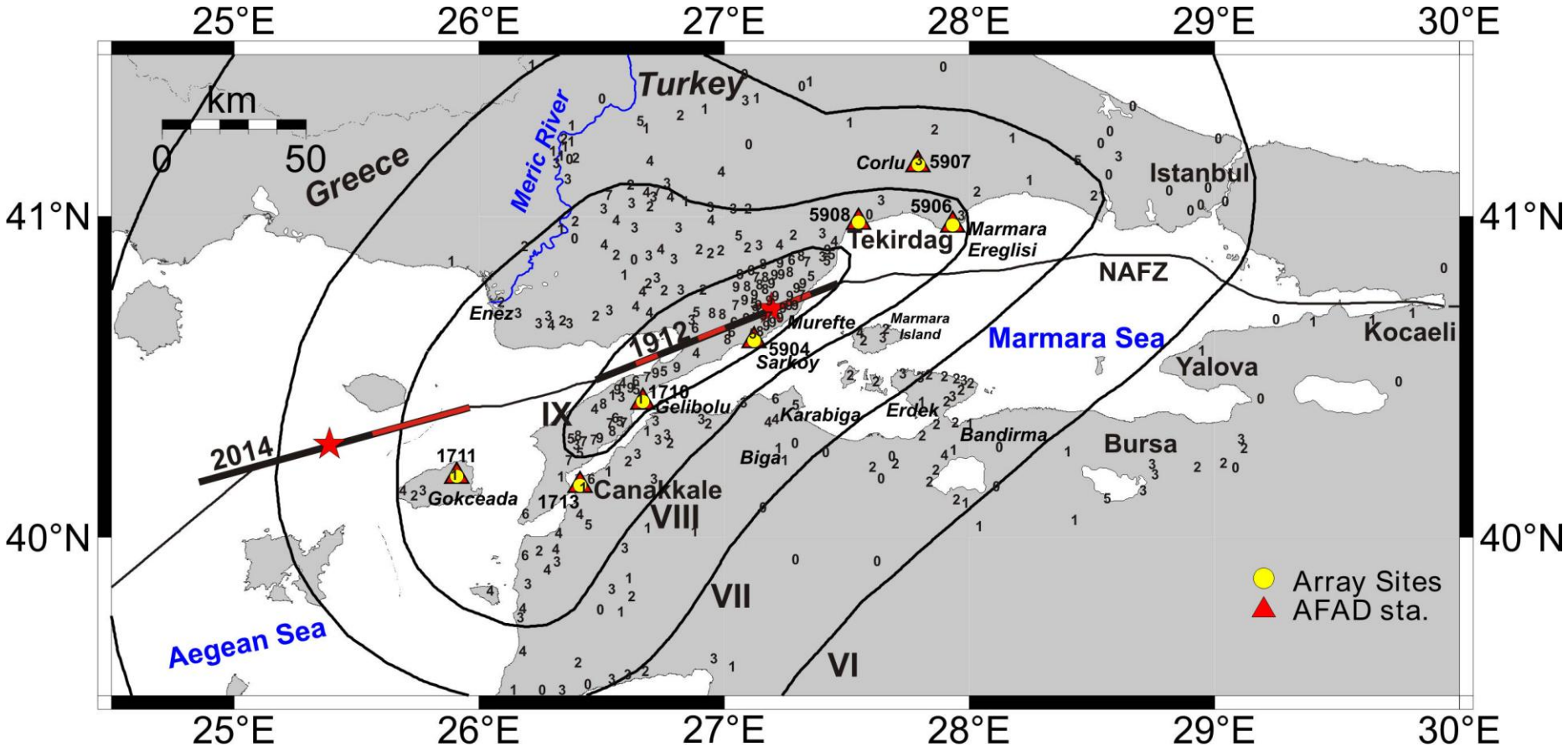

Figure 5.1 Isoseismal map and damage ratios (0-9) of the 1912 Murefte earthquake (digitized from Ambraseys and Finkel 1987). Red stars show the epicenters of the 1912 Murefte and 2014 Gokceada earthquakes. The background and asperity areas of the mainshocks are shown with thick black and red lines, respectively. The selected AFAD stations and microtremor array sites are shown with red triangles and yellow circles, respectively.

5.2 Determination of Characterized Source Model

5.2.1 Outer Fault Parameters

The first step of the source definition was to identify the rupture length of the mainshock. The Guzelkoy, Yenikoy and Saros segments of the Ganos Fault observed in the field surveys with maximum slip measurements by Aksoy et al. (2010) are shown in Figure 5.2. The empirical equations given by Wells and Coopersmith (1994) were used to estimate the fault length. They were indicated that surface (SRL) and subsurface (RLD) fault length can be calculated from the seismic moment magnitude (M_w) using the following linear relationships that obtained from the regression analysis of the worldwide 421 historical earthquakes

$$\log (SRL) = -3.55+0.74*M_w \text{ (std= 0.23, } 5.6 < Mw < 8.1)$$

$$\log (RLD)= -2.57+0.62* M_w \text{ (std= 0.15, } 4.8 < Mw < 8.1)$$

The empirical relationships give 71 and 90 km surface and subsurface rupture length, respectively, for a moment magnitude 7.3. On the other hand, Ohta et al. (1985) indicated that isoseismal lines of intensity VII are in general longer than faults and those of intensity VIII or IX correspond to the fault length. Using this approach, the measured distance between the two ends of the intensity IX of the 1912 Murefte earthquake along the fault strike is about 90 km (Figure 5.2) that is in agreement with the previous field surveys. The calculated subsurface length (90±14 km) using the empirical equation of Wells and Coopersmith (1994) is also in good agreement with the fault length measured from the intensity contour of IX along the strike. The width of the ruptured area (W) was chosen 20 km according to the step-1 ($L \geq Wmax$) in the recipe of Irikura and Miyake (2011) because the rupture length is larger than the width of the seismogenic zone (Wmax=20 km by Karabulut et al. 2006).

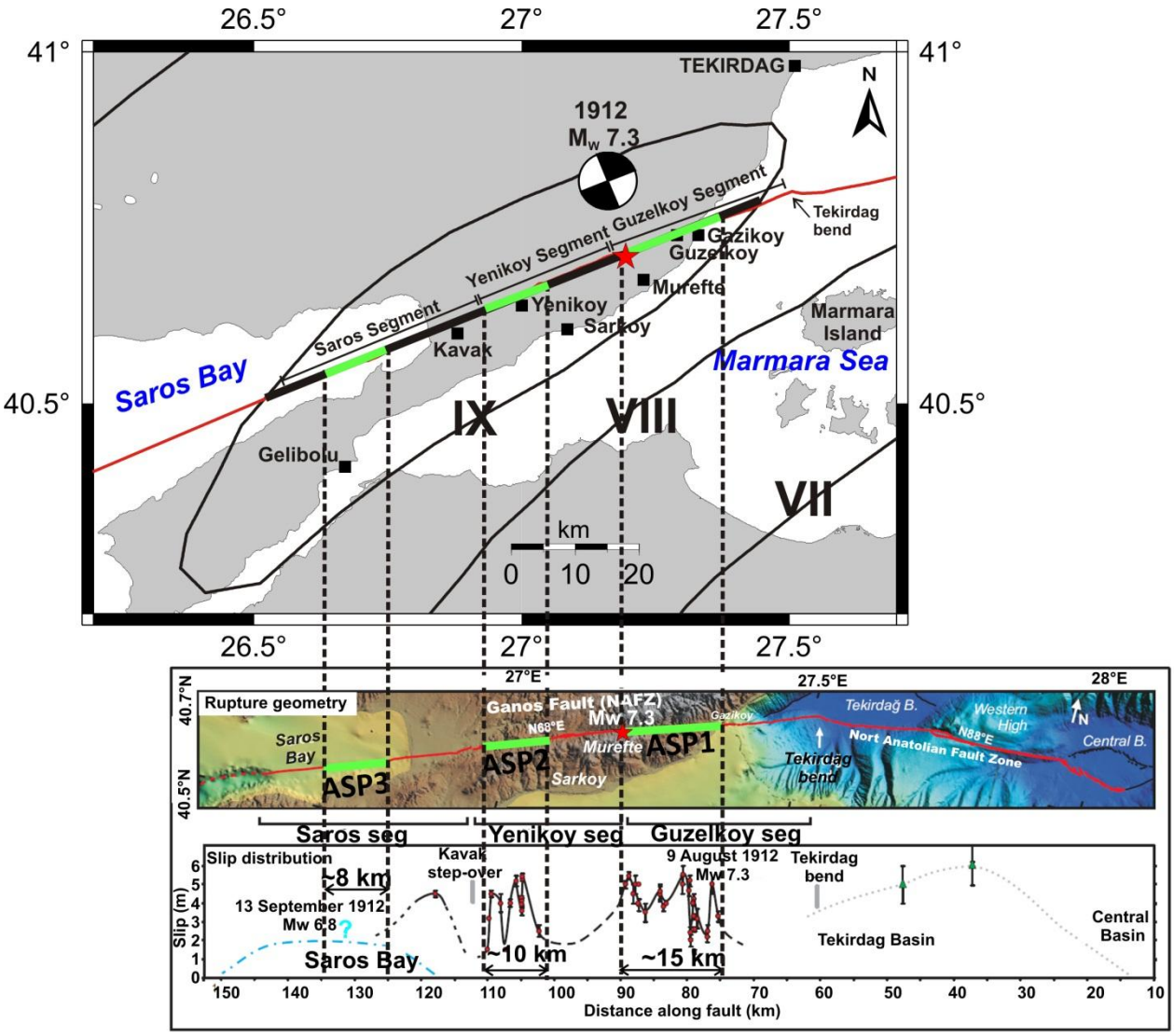

Figure 5.2 The 90 km ruptured-fault (black line) of the 1912 Murefte earthquake used in 1D simulation. The intensity contours are shown with black line. The sub-segments of the Ganos Fault determined from previous field studies are shown utilizing Aksoy et al. (2010) under the map. The red star shows the mainshock epicenter with focal mechanism solution.

The Ganos Fault trace observed on the surface indicates that the strike is 68° (Aksoy et al. 2010). Due to lack of fault plane solution on the Ganos Fault, the dip and rake angles were used 90° and 180° for the right-lateral strike-slip faulting (Figure 5.2). The previous field surveys for slip distribution on the land given by Aksoy et al (2010) in Figure 1.9 (Chapter 1) were used to define the asperity areas because there is no information about slip distribution on the fault surface for this earthquake and extremely low seismic activity in the instrumental period (see Figure 1.3).

The parameters of a characteristic source model definition were explained in Chapter 4. The BG area was divided into 36x8 sub-faults with the size of 2.5 x 2.5 km^2 similar to the 2014 Gokceada earthquake. Although the mainshock ruptured the surface, the depth of the top of the BG was taken 4 km from the surface considering low-velocity sedimentary layers in near-surface. The defined parameters of the source models used in the numerical 1D simulation are given in Table 5.2. According to the defined fault segments on the Ganos Fault, two different source models were generated. The Model A and Model B contains two and three asperities, respectively. The BG area parameters were common in both models.

Table 5.2 Source parameters of the 1912 Murefte earthquake. A and B models are the source model with two and three asperities, respectively. N and M describe the number of sub-faults along strike and dip on the ruptured fault area, respectively. No and Mo represent the sub-fault number that rupture starts. G: Guzelkoy segment, Y: Yenikoy segment, SR: Saros Bay Segment.

Fault Parameters	**Model A**			**Model B**			
	BG	**ASP-1 (G)**	**ASP-2 (Y)**	**BG**	**ASP-1 (G)**	**ASP-2 (Y)**	**ASP-3 (SR)**
Fault size (L (km) x W (km))	90x20	20x15	10x10	90x20	15x15	10x10	8.125x8.125
Number of Sub-faults (N x M)	36x8	32x24	16x16	36x8	24x24	16x16	13x13
Rupture start sub-fault no (No x Mo)	26x5	1x14	16x14	26x5	1x14	16x14	13x13
Sub-fault Size (km x km)	2.5x2.5	0.625x0.625		2.5x2.5	0.625x0.625		
Fault top (km) from surface	4	6.5	6.5	4	6.5	6.5	6.5
Seismic Moment (dyn.cm)	6.40×10^{26}	4.67×10^{26}	1.23×10^{26}	6.83×10^{26}	3.44×10^{26}	1.23×10^{26}	8.00×10^{25}
Rigidity (dyn/cm²)	3.00×10^{11}			3.00×10^{11}			
Source Time Function Type	Smoothed ramp velocity	Kostrov-like slip-velocity		Smoothed ramp velocity	Kostrov-like slip-velocity		
Rise Time (s)	2.18	3.70	1.85	2.18	2.78	1.85	1.50
Average Slip (Dave) (m)	1.2	5.2	4.1	1.3	5.1	4.1	4.0
Average Stress Drop (MPa)	2	22	30	2.2	25	30	36
Sample rate (Δt) (s)	0.05	0.05	0.05	0.05	0.05	0.05	0.05
Rupture Velocity (km/s)	2.7			2.7			
Slip Ratio (Dave/Dbg)	2.0			1.9			
Focal depth (km)	15.25 (focal depth)			15.25 (focal depth)			
Strike/Dip/Rake (°)	68° / 90° / 180°			68° / 90° / 180°			
Epicenter (°N/°E)	40.70° / 27.20° (Ambraseys and Jakson 200) 40.7133° / 27.1924° (projected to location on the fault)			40.70° / 27.20° (Ambraseys and Jakson 200) 40.7133° / 27.1924° (projected to location on the fault)			

5.2.2 Inner Fault Parameters

5.2.2.1 Model A

The average slip on the BG about 1.2 m and the stress drop is 2.0 MPa in Model A. The asperities of the Model A were located at the Guzelkoy and Yenikoy sub-segments (Figure 5.2). The size of the first asperity (ASP-1) that corresponds to the Guzelkoy segment was taken as 20x15 km^2 and the calculated average slip was 5.2 m. The Yenikoy sub-segment was named as ASP-2 with the calculated average slip of 4.1 m. I tried to keep the calculated slip values as close as the observed slip measurements along the surface fault rupture by Aksoy (2010) for two source models given in Figure 1.9 (Chapter 1). The depths of the top of the asperities were 6.5 km utilizing the 2014 Gokceada earthquake source model. The ratio of the area of the ASP to the BG was also taken into account to be 22% and their average displacement ratio (Da/D) is 2.0 from the recipe of Irikura and Miyake (2011) (steps 4 and 7).

The fault model and rupture propagation of the model is given in Figure 5.3 on the left side. The rupture start time of each sub-fault in BG and ASPs was calculating according to its distance to the focal point. The incoherent random fluctuation (Δt_r) was calculated using uniformly distributed random numbers *(rnd)* in a range of ±1 s that corresponded to 1/25 of the total rupture time of 25 s and was added to the homogeneous circular rupture front time (t_r) to increase high frequency amplitudes of synthetic seismogram by following the method mentioned in Chapter 4. The constant rupture velocity over the fault area was taken as 2.7 km/s assuming 80% of the S-wave velocity in the focal layer. The Δt_r was calculated for BG as

$$\Delta t_r = t_r * rnd * 0.2 \quad ; tr < 5\ s \qquad (1)$$

$$\Delta t_r = rnd \qquad ; tr \geq 5s \qquad (2)$$

To prevent generating negative rupture times in the BG because of the random numbers, we introduced equation (1) for the first 5 s of the rupture and the later times were calculated with equation (2). The rupture time of a sub-fault (t_r') in the BG was calculated with

$$t_r' = t_r + \Delta t_r$$

The sub-fault sizes of the ASP were too small respect to the BG and we scaled the random numbers by a coefficient (q) considering the sub-fault size (dx) and V_r to obtain the incoherent random fluctuation of the ASP (Δt_{ra}) as

$$q = dx / V_r$$

$$\Delta t_{ra} = q * rnd$$

This scaling prevented to rupture of a sub-fault later than the next neighboring sub-fault. The rupture time of a sub-fault (t_{ra}') in the ASP was calculated as

$$t_{ra}' = t_{ra} + \Delta t_{ra}$$

The rupture front times of the ASPs are in good agreement with BG.

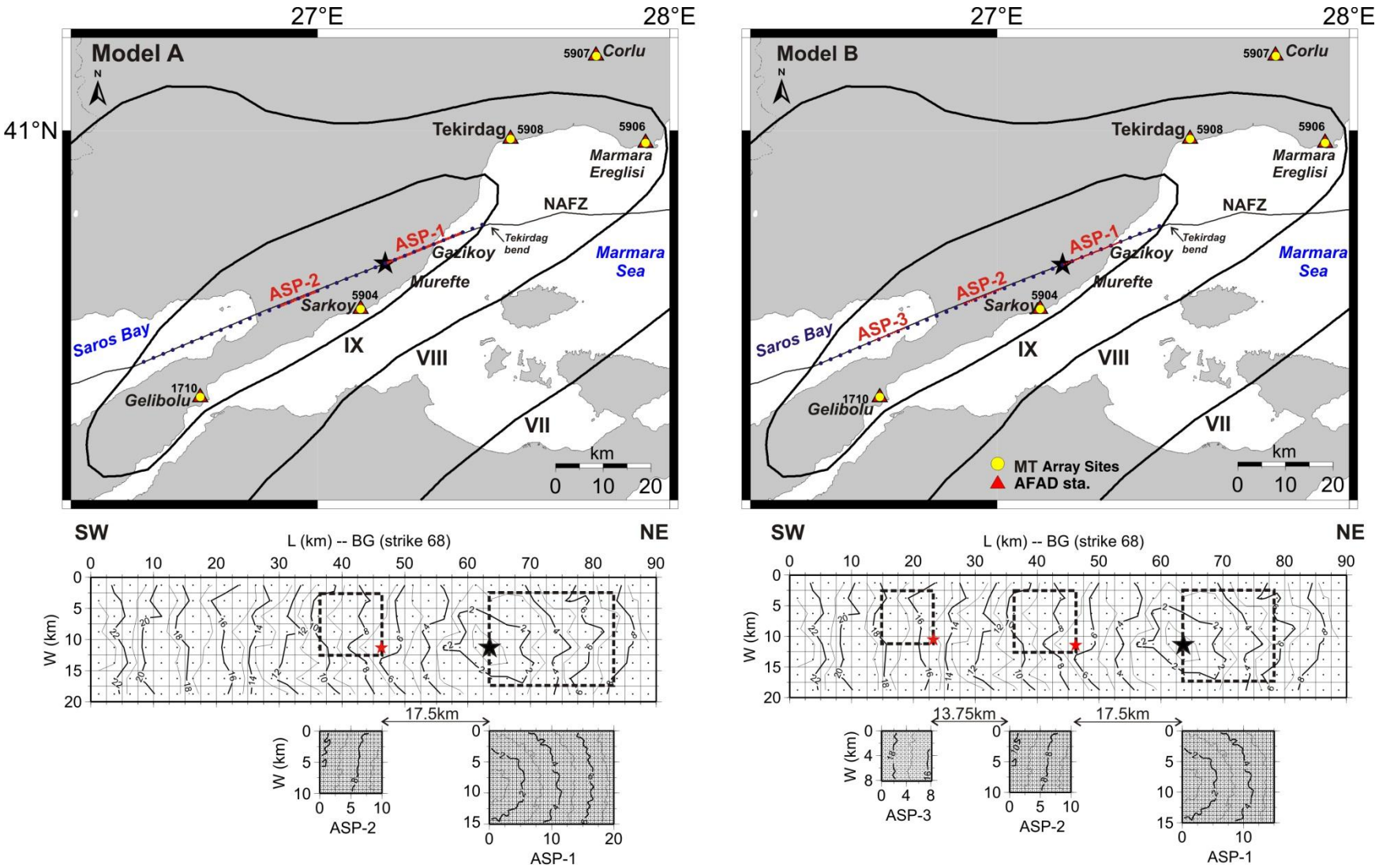

Figure 5.3 Rupture models used in 1D simulation of the 1912 Murefte earthquake. Model-A with two asperities is on the left, Model-B with three asperities is on the right. The sub-fault locations of BG and ASP are shown with blue and red dots on the maps. The rupture propagation times (seconds) on the fault are beneath the maps. The mainshock hypocenter is shown with black star on the maps and rupture propagation models. The black dashed rectangles show ASP areas with their rupture starting point (red stars). The grid cells show sub-faults of the ruptured area.

5.2.2.2 Model B

The contour of intensity IX extends to southwest therefore, one more asperity was added. The third asperity was located in the Saros Bay to understand its effect on the intensity values (Figure 5.3). The two asperities of the Model B were located to the Yenikoy (ASP-2) and Guzelkoy (ASP-1) sub-segments same with the Model-A. The size of ASP-2 was not changed while the size of ASP-1 was taken as 15x15 km^2 (Table 5.2). The third asperity has an area of about 8x8 km^2. Thus, the ratio between the areas of the ASP and BG to be 22% was preserved. The calculated average slip values of the ASP-1, 2, 3 areas are 5.1, 4.1, 4.0 m, respectively. The displacement ratio (Da/D) was 1.9 that is similar to the ratio given by Dalguer et al. (2008) and Irikura and Miyake (2011). The fault model and rupture propagation of the model is given in Figure 5.3 on the right side.

5.3 Decision of the Final Source Model

The numerical 1D simulation results of Model A and Model B are given in Figures 5.4 and 5.5, respectively. The surface velocity ground motions comparison of the two models for both NS and EW components are shown in Figure 5.6. The simulated velocity ground motions were calculated with DWNM on the engineering bedrock. 1D deep velocity structures in Table 3.2 in Chapter 3 in four azimuthal directions and defined characterized source models in this chapter by following 1D simulation flow-chart in Figure 4.3 in Chapter 4 and 1D amplification given in Figure 2.17 in Chapter 2.7 were used as inputs for 1D simulation.

It is clearly indicates the importance of the introduction of a proper asperity area with Kostrov like slip-velocity function, fluctuating rupture front time and local site effects at individual observation sites to obtain high frequency motion. The high frequency waveforms are clear at all stations. The low frequency surface waves are observed at distant stations (1713, 1711) in Figures 5.4 and 5.5. The effect of high frequency waves in the S-wave part decrease in Model B because of the additional asperity. The contribution of the ASP-3 is seen on both engineering bedrock and surface synthetic seismograms after 40s at the stations 5908, 5906 and 5907 in Tekirdag (Figure 5.5).

The waveforms of Canakkale stations (1710, 1713 and 1711) are mostly similar in both models in Figure 5.6. The high frequency contents of S-wave part increase because of the ASP-3. The PGV on the EW component (137.22 cm/s) increased at 1710 because the ASP-3 is close to the station. On the other hand, ASP-3 has more clear effect on the duration and amplitude of the waveforms at Tekirdag stations. The amplitude of the later arrival phases from ASP-2 and ASP-3 are decreased while the amplitude and high frequency content of S-wave part from ASP-1 decrease at Tekirdag stations (5908, 5906, 5907) in Figure 5.6. Therefore, ASP-3 increases the back directivity effect on the synthetics seismograms on the Tekirdag direction with azimuth average 50°.

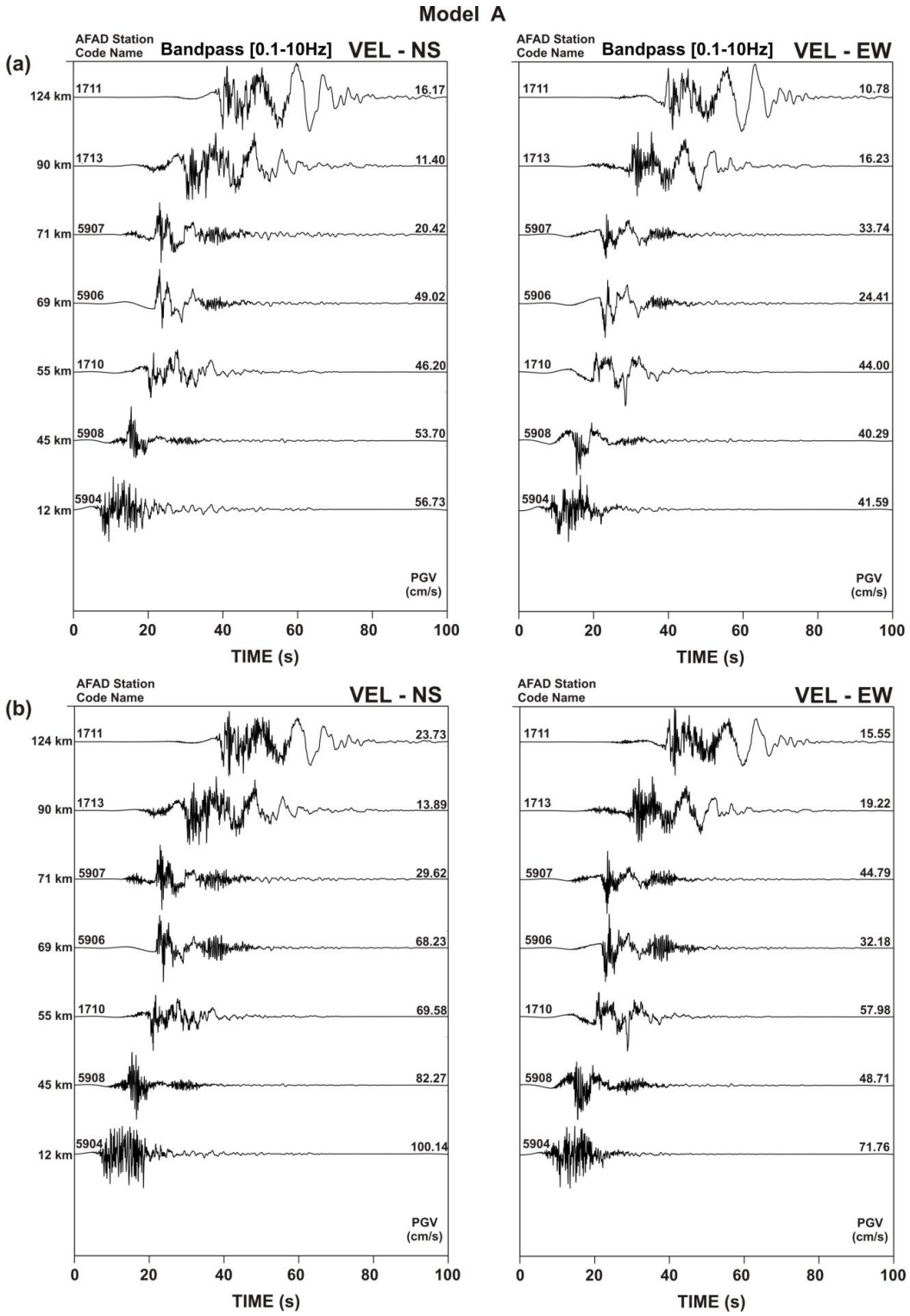

Figure 5.4 Simulated velocity ground motions on the engineering bedrock (a) and surface (b) of Model A. The engineering bedrock velocity waveforms were filtered between 0.1 and 10 Hz. The NS and EW components are given left and right, respectively. The amplitudes are normalized, and the peak values (cm/s) are given in the right of each seismogram. Epicentral distances of the stations are on the right side.

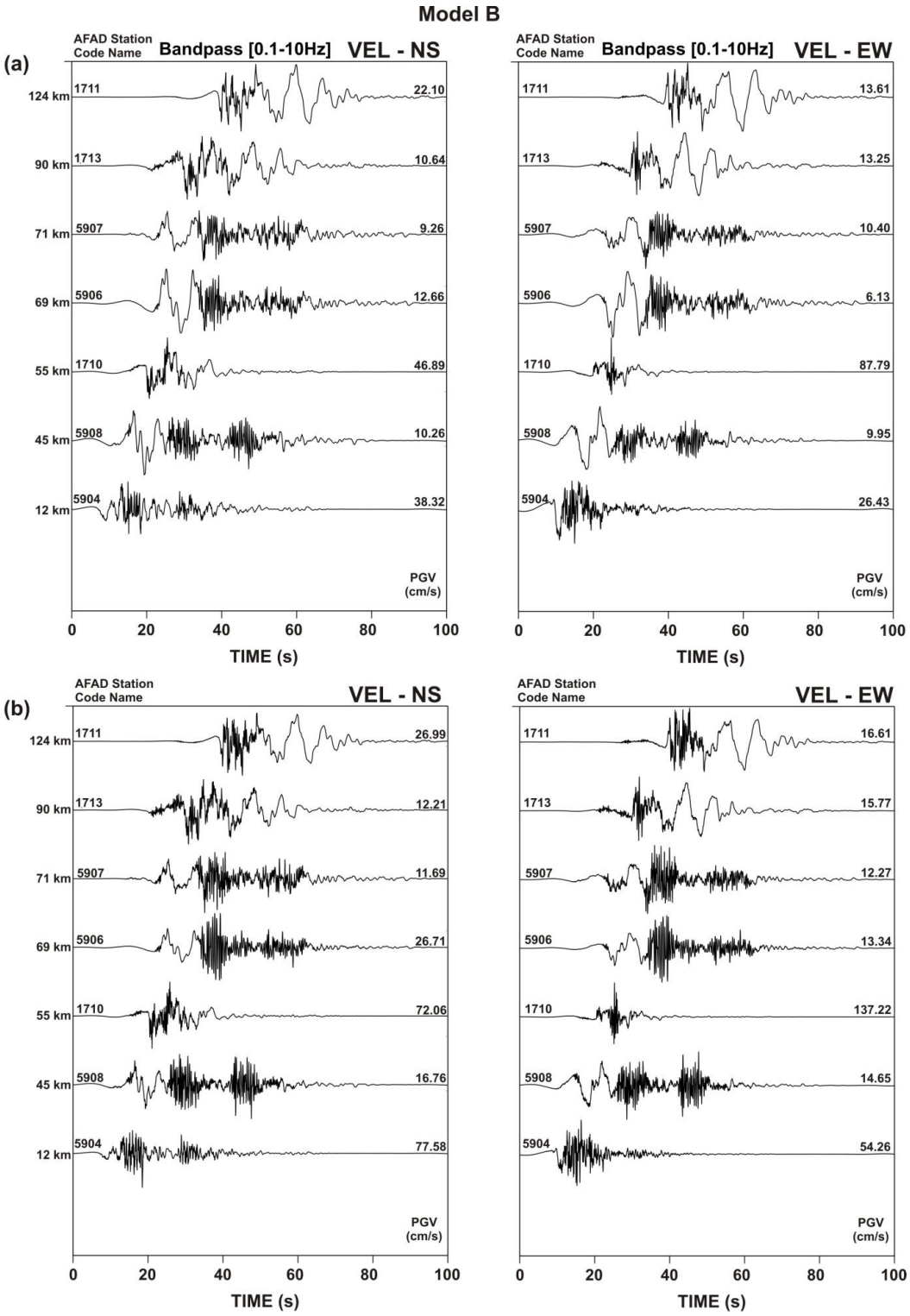

Figure 5.5 Simulated velocity ground motions on the engineering bedrock (a) and surface (b) of Model A. The engineering bedrock velocity waveforms were filtered between 0.1 and 10 Hz. The NS and EW components are given left and right, respectively. The amplitudes are normalized, and the peak values (cm/s) are given in the right of each seismogram. Epicentral distances of the stations are on the right side.

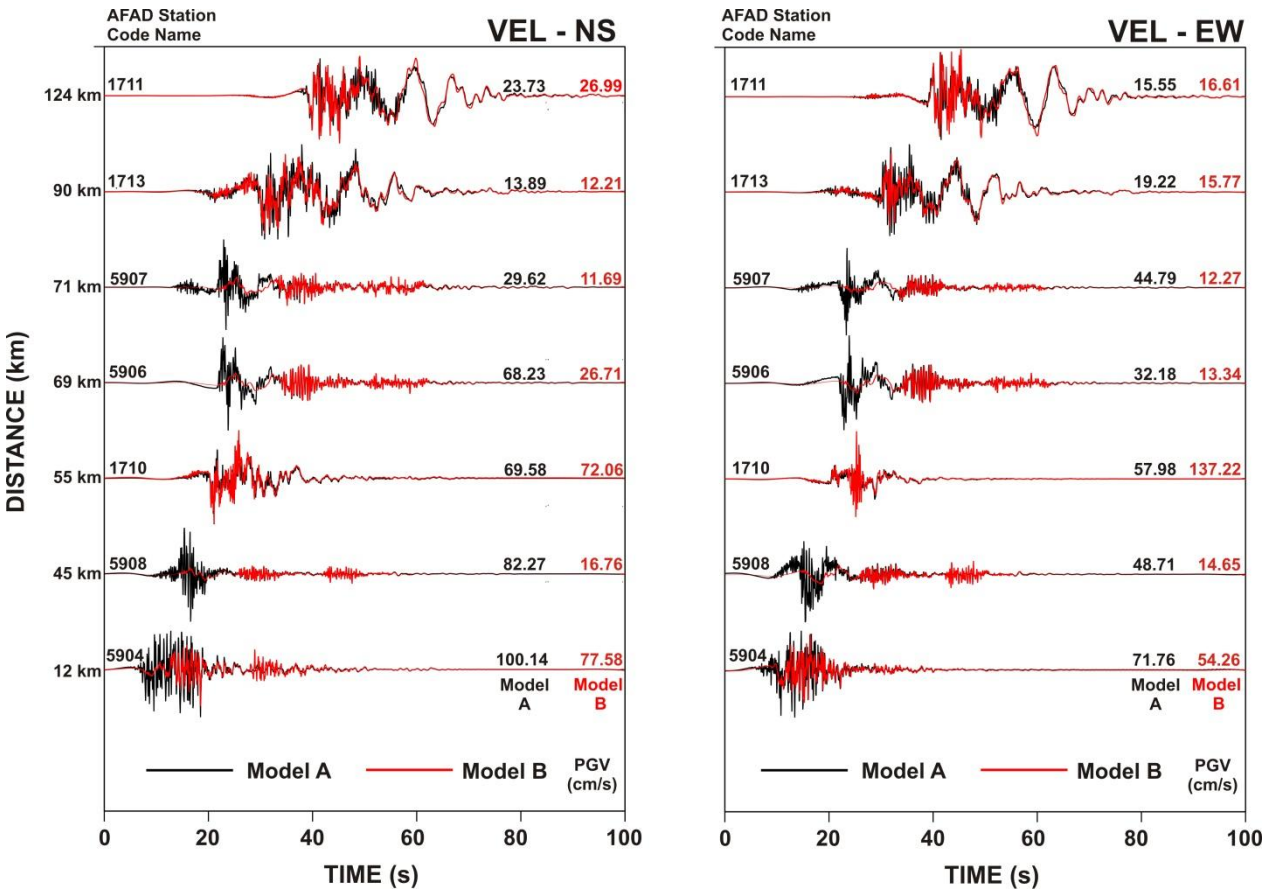

Figure 5.6 Simulated surface waveform comparison of the both Model A (black) and Model B (red). The amplitudes of each seismogram are normalized according to maximum PGV of the models, and the peak values (cm/s) are given in the right of each seismogram. Epicentral distances of the stations are on the right side.

To validate the models, the PGV values of the surface ground motions were used to calculate intensities for the stations. The PGV-Intensity relationship that was given by Bilal and Askan (2014) was used. They employed standard least squares regression technique on the horizontal component of 92 records from 14 moderate-to-large earthquakes with $5.7 \leq M_w \leq 7.4$ that occurred in Turkey between 1976 and 2011 to relate MMI simply to PGA, PGV and peak spectral acceleration (PSA). They used MMI information inferred from isoseismal maps and earthquake damage reports. The intensity relationship is given as below.

$$I = 2.673 + 4.34*\log(PGV) \qquad \text{(Bilal and Askan 2014)}$$

The differences (ΔI) between the calculated and observed intensities were given in Table 5.3 and Figure 5.7. The calculated and observed intensity differences as shown in Figure 5.7 indicated that the Model A has a uniform bias that is larger than the Model B. Therefore, calculated intensities are close to observed ones in Model B. On the other hand, the positive difference between the intensities (ΔI>0) indicates calculated ones higher than the observed in Table 5.3. Bilal and Askan (2014) intensity relationship gives large differences up to +3 for both models. The average and standard deviation of ΔI are 1.9 and 0.9 for Model A, 1.1 and 1.3 Model B, respectively given in Table 5.3. The correlation coefficients between observed and calculated intensities are 0.5 and 0.9 for Model A and B, respectively. The statistical parameters indicate that the Model B with three asperities is better than the Model A.

Table 5.3 Station code, observed intensity (I_{MSK}), PGV, calculated intensity (I_{CAL}) and intensity differences (ΔI). Statistical parameters for average ΔI and its standard deviation, and correlation coefficient (R) are given for both models.

Station Code	**Observed**	**Model A**			**Model B**		
	I_{MSK}	**PGV**	**$I_{CAL.}$**	**ΔI**	**PGV**	**$I_{CAL.}$**	**ΔI**
5904	IX	100.14	XI	+2	77.58	XI	+2
5908	VIII	82.27	XI	+3	16.76	VIII	0
1710	IX	69.58	XI	+2	137.22	XII	+3
5906	VIII	68.23	XI	+3	26.71	IX	+1
5907	VIII	44.79	X	+2	12.27	VII	-1
1713	VIII	19.22	VIII	0	15.77	VIII	0
1711	VIII	23.73	IX	+1	26.99	IX	+1
				Statistical Parameters			
Average differences of Intensity				**1.9**			**0.9**
Standard deviation				**1.1**			**1.3**
Correlation Coefficient(R)			**0.5**			**0.9**	

The PGV values for the Model B with three asperities are lower than that of Model A, and the calculated intensities decrease in Figure 5.7. The average ΔI shifted about 1 unit better than the Model A (Table 5.3). The correlation coefficient (R) of Model A is lower than the Model B obtained from the relationship. The R value is 0.9 for the Model B and indicates that the correlation between observed and calculated intensities is better than the Model A.

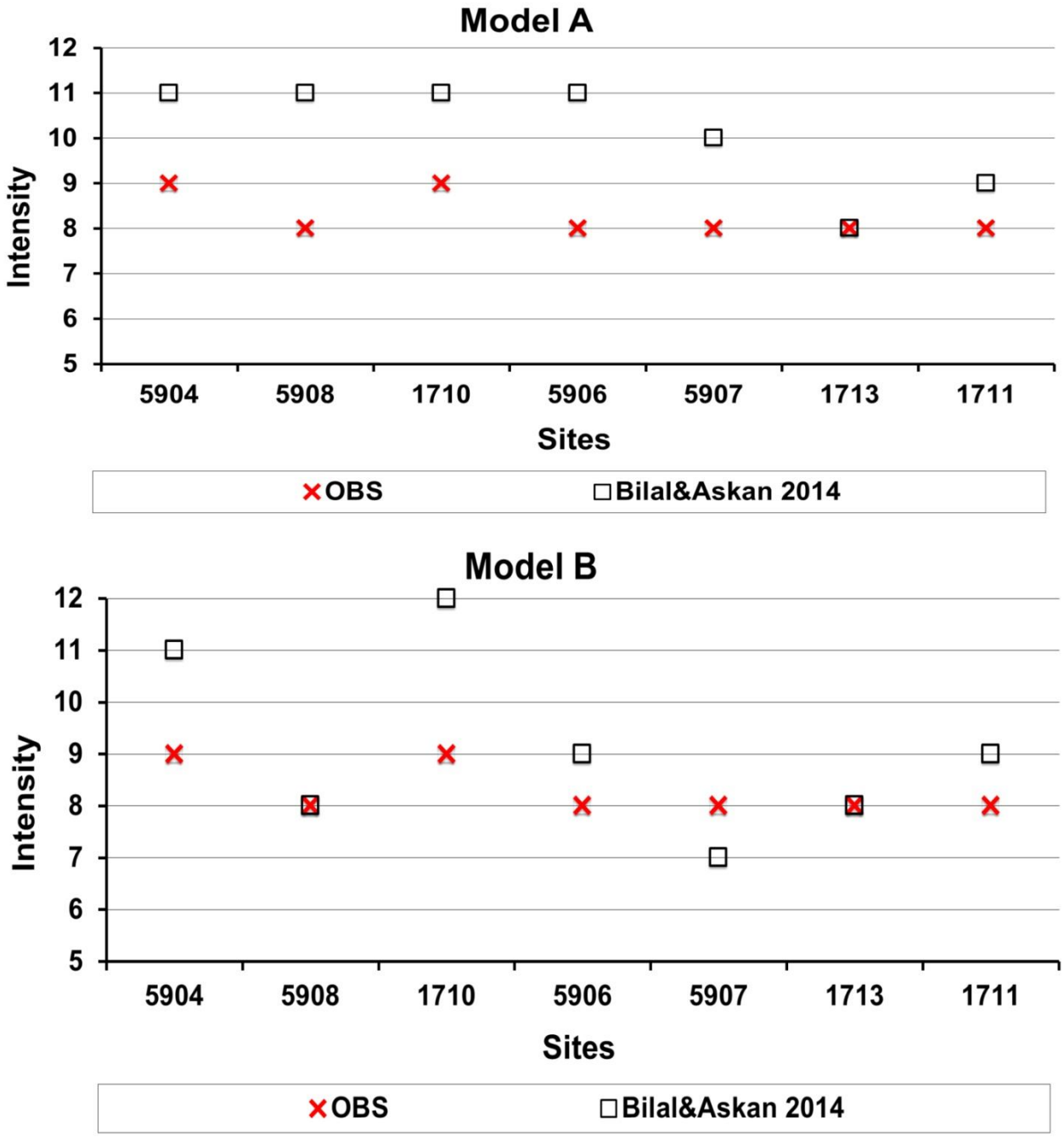

Figure 5.7 Comparisons of the observed and calculated by using Bilal and Askan 2014 relationship intensities for Model A (top) and Model B (bottom).

5.3 Near Fault Response Spectra of the Ground Motions

Earthquakes produce complicated loading in a broad frequency range. Structures such as buildings and bridges that located on slopes or soil deposits are sensitive to the frequency distribution of loading. The response spectrum that is used extensively in earthquake engineering practice describes the maximum response of a single-degree-of-freedom system (SDOF) to a particular input motion as a function of the natural period (or natural frequency) and damping ratio of the system. SDOF gives a practical method in structure design using the information of structural dynamics and progress in lateral force requirements in building design codes. The response can be expressed in terms of acceleration, velocity or displacement. The maximum values of each ground parameters depend only on the natural period and damping ratio of the SDOF system for a particular input motion. The response spectrum does not describe the actual ground motion, but it provides valuable additional information on potential effects on structures.

5.3.1 Simulated Waveforms of the Selected Near-Fault Sites

The damage of the 1912 Murefte earthquake in the epicentral region was heavier than the other sites. Therefore, the four sites located in the epicentral region were selected to understand characteristics of the ground motions (Figure 5.8). Information about the selected sites is given in Table 5.4. The perpendicular distances between the Ganos Fault and Kavak (KVAK), Golcuk (GLCK), Gazikoy (GZKY) and Murefte (MRFT) sites are 1.5 km, 0.4 km, 0.6 km and 6.5 km, respectively. The KVAK and GLCK sites do not have 1D S-wave shallow structure. The empirical relationship between AVs30 and average slope that obtained for the continental clastic rocks geological unit in Figure 2.21c (in Chapter 2) is used to calculate AVs30. Then the empirical relationship for AVs30- average site amplification is used to calculate average site amplifications for these sites. During the 1D simulation procedure, the input motion on the engineering bedrock was divided two to eliminate the free surface effect and multiplied with the calculated average site amplification value in the frequency domain to obtain the surface motions at those sites.

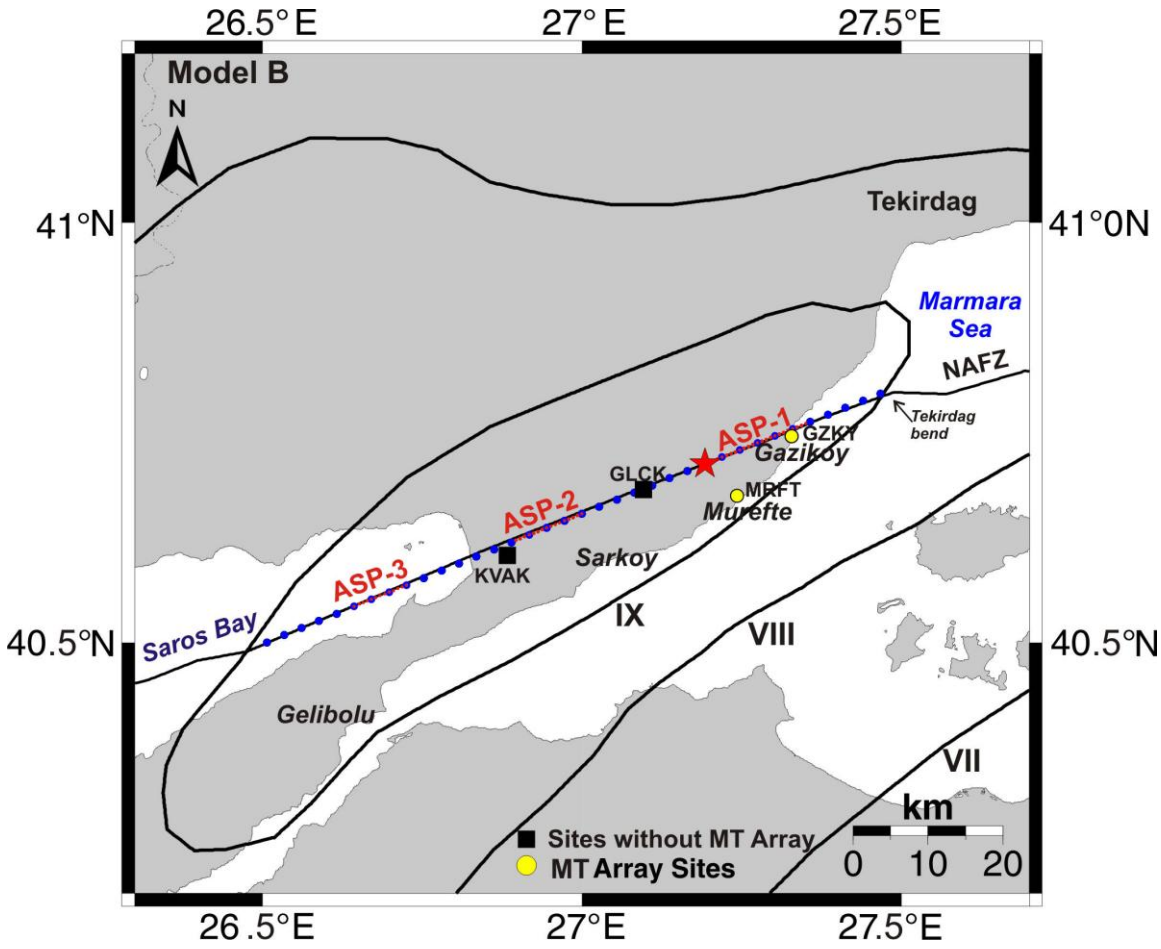

Figure 5.8 Selected sites for calculation of acceleration spectra for the 1912 Murefte earthquake. The sites that have MT array observations are shown with yellow circle. The sites without MT observations (Kavak-KVAK and Golcuk-GLCK) are shown with black squares.

Table 5.4 Location, perpendicular distance from the fault, azimuth, average slope, AVs30, NEHRP site class, average site amplification, damage and intensity information of the selected sites for the 1D simulation of 1912 Murefte earthquake.

Site Code	Latitude (°N)	Longitude (°E)	Distance from the fault (km)	Site Azimuth (°)	Average Slope	AVs30 (m/s)	NEHRP Site Class	Ave. Site Amp.	Damage Ratio No	Intensity (MSK)	
										Obs.	Cal.
KVAK	40.60601	26.88500	1.5	245.5	0.12128	591[+]	C	2.5[+]	8	X	XIII
GLCK	40.68346	27.09500	0.4	248.2	0.07393	522[+]	C	2.7[+]	9	X	XIII
GZKY	40.74766	27.32757	0.6	71.5	0.21400	580[*]	C	2.7[*]	9	X	XIV
MRFT	40.66780	27.24481	6.5	138.8	0.00015	295[*]	D	4.6[*]	9	IX	XII

[+]AVs30 was calculated from the AVs30-slope relationship for continental clastistic rocks in Figure 2.21c. Average site amplifications were calculated by using AVs30 and average site amplification relationship given in Figure 2.18.
[*]AVs30 and average site amplifications were obtained from the 1D shallow S-wave profiles in microtremor array explorations.

The simulated surface velocity waveforms are given in Figure 5.9. Gazikoy and Murefte were totally destroyed with 162 and 306 losses of lives that were mentioned in Ambraseys and Finkel (1987), respectively. GZKY is located in the forward propagation direction of the ASP-1 and backward of the ASP-2 and ASP-3. The velocity seismograms have a clear peak on the S-wave part in the both NS and EW components because of the forward directivity and proximity of the ASP-1 (Figure 5.9). MRFT site is located on the backward propagation of the three ASPs and it is 6.5 km far from the fault. Contrary to the other sites, it has the lowest PGV. It is difficult to mention a dominant directivity effect on this site because it is on the fault normal direction. GLCK located in the middle of ASP-1 and ASP-2. It is clear that the ASP-2 has dominant amplitudes on the synthetic velocity seismograms in Figure 5.9, because the stress drop of ASP-2 is higher and its rise time is shorter than ASP-1. On the other hand, the PGV is lower than the GZKY and KVAK because of the backward directivity of the ASPs. KVAK located on the forward propagation of the ASP-2 and that made the more amplified ground motions than GLCK (Figure 5.9). ASP-1 and ASP-3 have the backward directivity effect at KVAK site. The calculated intensities are higher than the observed ones at KVAK, GLCK and GZKY in Table 5.4. One of the reasons of high-calculated intensities is that the sites are very close to the asperities on the fault. The limited recent earthquake data used in the empirical relationship of Bilal and Askan (2014) may be another reason for the high values.

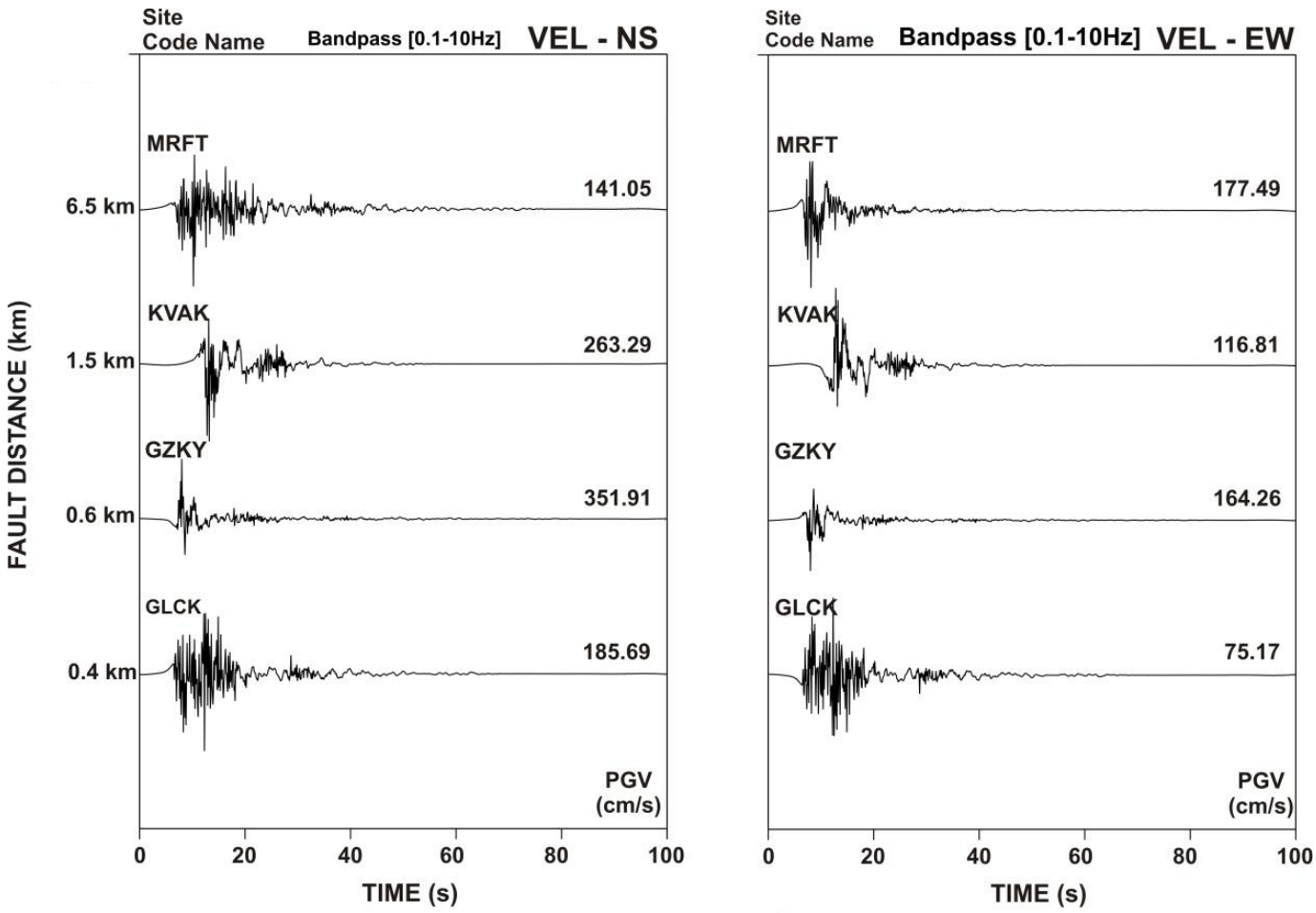

Figure 5.9 Simulated surface velocity (VEL) waveforms at near field sites. The NS and EW components are given left and right, respectively. The amplitudes are normalized, and the peak values are given in the right of each seismogram. Perpendicular fault distances of the sites are on the right side.

5.3.2 Response Spectra of the Ground Motions

To understand the characteristic of the 1912 Murefte earthquake strong ground motions, the acceleration response spectra were calculated according to the Turkish Building Code 2007 (TBC-2007, see Appendix C) at near-fault sites. The effective ground acceleration coefficient (*Ao*) is used as 0.4 g because the sites were in 1st seismic zone (Figure 1.5 in Chapter 1). The building importance factor was used for residential buildings (*I*=1.0). The spectrum coefficient *S(T)* was calculated for 5% damping as described in the TBC-2007.

The response acceleration and velocity spectra of the near-fault ground motions are shown in the Figure 5.10. The selected sites are in C and D class according to the NEHRP classifications that correspond to the Z3 and Z4 in TBC-2007 (see Appendix C Table C.1-2-3). The spectral acceleration of the NS components of the selected sites is higher than the design requirements between 0.1 and 3 s for the Z4 class defined in the TBC-2007 (Figure 5.10a). For the EW component, the upper limit of this period range is about 1 s. The spectral accelerations of the all sites at low periods (0.15-0.60 s) are also higher than the requirements of the TBC-2007 for Z2 and Z3 type of soil in Figure 5.10a. GZKY shows high spectral acceleration amplitude on the NS component, especially at low periods (high frequencies), due to the forward propagation effect of the ASP-1. However, MRFT shows the lowest values for the same component while highest spectra on EW component for the period range of 0.3 – 1 s. The results indicate that the location of the sites respect to the fault and location of asperities are important on the spectral acceleration characteristics of the ground motions.

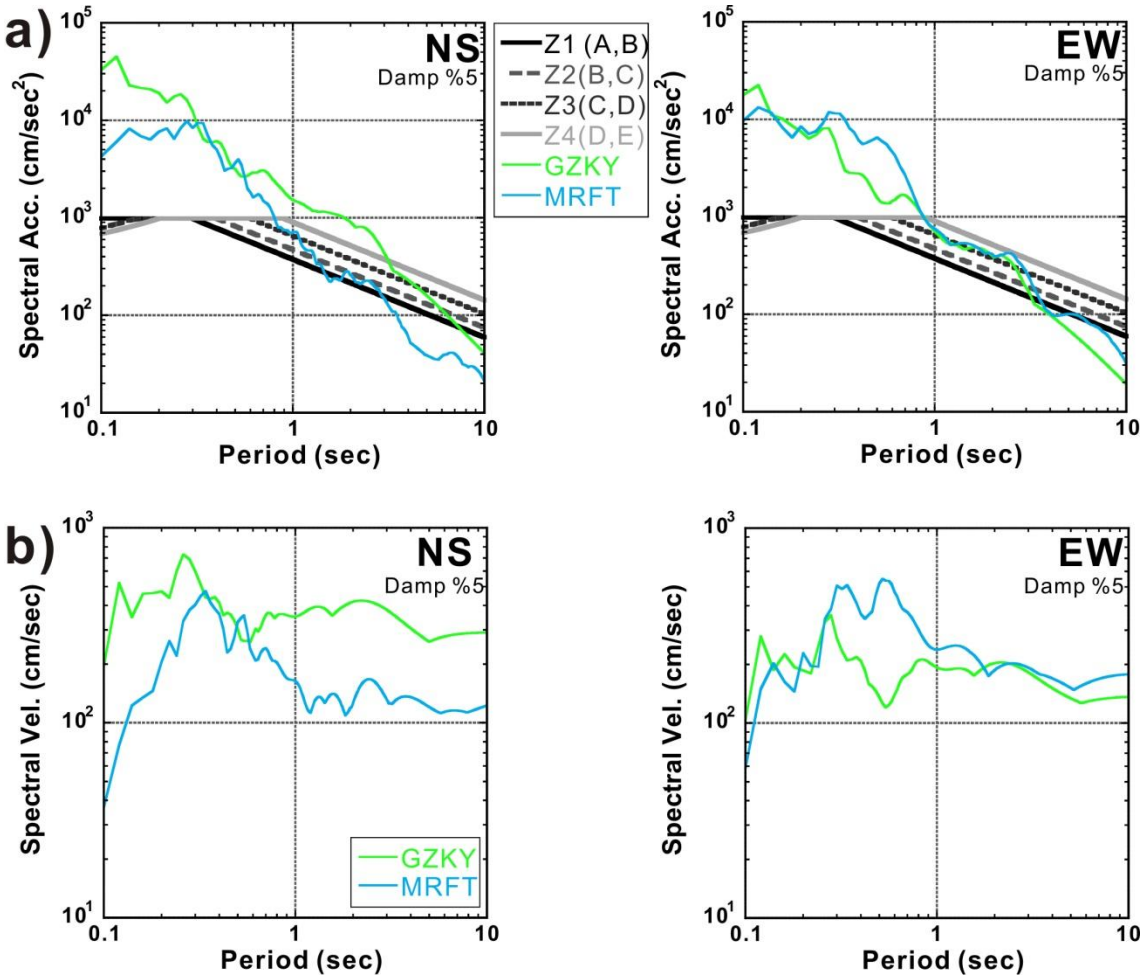

Figure 5.10 Response acceleration and velocity spectra for the near-fault sites are given in (a) and (b) for both NS and EW components. The response acceleration design spectra according to the TBC-2007 are calculated for four different site class (Z1-4).

The response velocity spectra indicate higher amplitudes at GZKY (Figure 5.10b). GZKY that located almost on the Ganos fault have higher spectral velocity than MRFT on NS component, while MRFT has high amplitudes over the period of 0.3 s on the EW component (on the intermediate periods). On the other hand, MRFT has peak spectral velocity at about 0.3 s and 0.3-0.6 s on the NS and EW components, respectively, due to high shallow soil amplification factor of 4.6 at the predominant period of 0.38 s (2.6 Hz). The intermediate periods (0.5-1 s) of the ground motions are important to estimate the lateral forces for the bridges and tall buildings. Therefore, further analyses may be useful for the planned Canakkale 1915 Bridge in Gelibolu (Canakkale) where is about 15 km far from the Ganos Fault Segment of the NAFZ.

5.4 Discussions

The results indicate the importance of analyzing high frequency waveforms with ground motion simulation. In this perspective, exploration of shallow S-wave velocity that controls the amplifications due to soil structure is also an important issue in engineering applications in the western Marmara Region.

Akkar and Gulkan (2002) indicated that the PGA values at near-source records were not high as expected in 1999 Kocaeli and Duzce earthquakes in Marmara and the structural damage along the Izmit Bay did not agree peak ground velocity observations. They concluded that the records at close distances to the NAFZ showed complex fault characteristics due to the surface rupture respect to geological conditions. The complexity of ruptures is not included in the definitions in the TBC-2007 because of lack of strong ground motion database. On the other hand, the TBC-2007 has no near-fault factors and defines the same peak value for different soil types (Dogangun and Livanoglu, 2006). Fault characteristics and near-fault factors must be included in the TBC like the Uniform Building Code (UBC 1997) in the USA.

Chapter 6

Conclusions and Future Tasks

6.1 Conclusions

6.2 Future Tasks

6.1 Conclusions

In this thesis, the 1D S-wave velocity structures of the shallow and deep soils were obtained using the microtremor array explorations and surface wave group velocity dispersion curve analysis of the 2014 Gokceada mainshock records. The characteristics of the 2014 Gokceada earthquake ground motions were investigated and the characterized source model and ground motions of the 1912 Murefte earthquake was determined in the western Marmara Region (NW Turkey) by using 1D simulation method including the 1D deep and shallow structures soil amplification effects.

The first comprehensive microtremor array measurements were performed at 44 sites to estimate S-wave velocity structures of the shallow soil layers in Tekirdag city center, Marmara Ereglisi, Muratli and Corlu districts, in the study area. Additionally, we applied microtremor array measurements at six sites close to the AFAD strong motion stations in Gelibolu, Enez, Gokceada and Canakkale city center to understand the site effects. The observed Rayleigh wave phase velocities were varied between ~90 m/s and 930 m/s in a frequency range from 2 to 30 Hz. We deduced the 1D S-wave structures of the shallow soils in Tekirdag city center and coastal area. The inversion results indicate that the 1D S-wave profiles can be grouped into four layers:

- 34 sites had the first layer with an S-wave velocity between 90 and 320 m/s.
- 31 sites had the second layer with an S-wave velocity in a range from 320 to 500 m/s.
- 25 sites contain the third layer with an S-wave velocity range from 500 to 700 m/s.
- 29 sites had the fourth layer with an S-wave velocity between 700 and 930 m/s defined as engineering bedrock.

Only two sites in Marmara Ereglisi had high velocities (>1000 m/s) for the deep parts that may be interpreted as the fifth layer. The top layers of sites located on the sandstone, claystone, and siltstone units had velocities of ~200 m/s. The velocities and thickness of the alluvial creek beds in coastal area were also clearly identified. The most significant part of the study area belongs to the alluvial creek beds. The results indicate that the observed phase velocities change due to the thickness of alluvium. Additionally, we noticed that the shapes of the observed dispersion curves of alluvial units were similar.

The AVs30 for most of the sites were distributed from 300 to 500 m/s in Tekirdag and it indicates a normal distribution with an average value of 410 m/s. Although the sites located near the seaside in Tekirdag showed low AVs30 (class E-D), high AVs30 were found (class C-B) in Marmara Ereglisi. The sites close to the AFAD stations in Gelibolu, Enez, Gokceada and Canakkale city center are in C and D site class in NEHRP with low AVs30.

The site amplifications were computed to understand the seismic motion behavior on the different geological units in the study area. There was only one site in Marmara Ereglisi on B class (rock) with a predominant frequency of 15.5 Hz and an amplification value of 2. The E class sites had predominant frequencies of 1.0-1.6 Hz, with similar high amplifications of ~9. The predominant frequencies in NEHRP class C were 5 – 15 Hz with amplification range from 3 to 9. The sites in class D showed predominant frequencies between 2 and 6 Hz. Comparison between the observed H/V ratio and calculated ellipticity of the fundamental mode Rayleigh waves for the inverted 1D soil profiles show that the observed peak frequency characteristics are generally in good agreement at frequencies between 1 and 20 Hz. The relationship equations with good correlation for AVs30-slope and AVs30-amplification were proposed for future usage in site response prediction studies.

The 1D deep velocity structures, especially shallower than 4-5 km, beneath the engineering bedrock with the S-wave velocity of 0.78 km/s at different azimuthal directions were tuned by comparing the observed group-velocity dispersion curves of Rayleigh and Love waves from the 2014 Gokceada main shock (Mw 6.9) records at AFAD stations with theoretical ones. The results show that the observed dispersion curves at frequencies between 0.07 and 0.80 Hz are sensitive to the layers above 4-5 km while the layers deeper than 4-5 km control the group velocity at the frequencies lower than 0.07 Hz. The tuned surface wave group velocity dispersion curves are generally in good agreement with the observed data for the frequencies between 0.15 and 0.8 Hz. Contrary to the other stations in the study area, the tuned model is the best model for Rayleigh and Love wave group velocities dispersions at Gokceada and Canakkale stations. The surface-wave dispersion analysis using the observed group velocities of Rayleigh and Love wave provides to determine effectively the S-wave velocities and thickness of the layers in the upper 4-5 km part of the crust. The tuned models indicate deeper layer interfaces than the initial model

defined from previous studies. The engineering bedrock thicknesses are found thicker than the initial model.

The broad band (0.1-10 Hz) ground motions of the 24 May 2014 Gokceada earthquake were simulated at 12 AFAD stations in the western part of the Marmara Region with the characterized source model considering effects of 1D shallow and deep shallow soil layers revealed from the analysis of earthquake data and microtremor array measurements. The source model parameters for the background and asperity areas were defined considering the results of teleseismic source inversion (Pinar 2014) and the recipe by Irikura and Miyake (2011). According to the large slip areas of Pinar's model, the defined asperity area in the source model is sufficient to generate high frequency synthetic ground motions of the 2014 Gokceada earthquake. To generate high frequency motions in the seismograms, (1) the Kostrov-like slip-velocity function was used for asperity area, (2) incoherent random fluctuation was added to the homogenous circular rupture front time and (3) 1D shallow soil amplifications were added on the engineering bedrock motion to increase high frequency amplitudes. The total rupture duration is acceptable for all the sites in the 1D simulation due to matching with significant duration at the closest station. The synthetic arrival times of the body and surface waves are close to the observations because 1D deep subsurface models have been constructed from the surface wave group velocity dispersion analyses.

The synthetic spectra of the horizontal components at the closest station are in good agreement at a frequency of above 1Hz. This indicates the sufficient capability of the models of the fault and 1D subsurface structure to generate the high-frequency motions.

Consequently, the importance of preparation of a proper 1D deep velocity structure beneath engineering bedrock to simulate low frequencies is emphasized by 1D ground motion simulation of the 2014 Gokceada earthquake. The local site effects were mostly successfully generated on the synthetic high frequency seismograms. The 1D simulation cannot generate sufficient results at special sites. As observed in Enez, Tekirdag, Corlu, a thick sediment basin with low seismic velocity beneath stations may cause slow and large surface waves, which cannot be generated in the 1D simulation, because of generation of locally trapped waves.

The 1912 Murefte earthquake was simulated by using 1D velocity structures to determine the characteristic source model and to understand the near-fault ground motions. The fault length is determined about 90 km. The 20 km-width of the ruptured area was chosen same as the seismogenic zone in the region. According to the defined surface fault segments on the Ganos Fault from the field surveys, two different source models were generated. The Model A and Model B contains two (ASP-1, 2) and three asperities (ASP-1, 2, 3), respectively. The ASP-1, ASP-2 and ASP-3 correspond to Guzelkoy, Yenikoy and Saros segments of the Ganos Fault, respectively.

The waveforms of Canakkale stations are mostly similar in both models. The contribution of the ASP-3 in Model B is seen on both engineering bedrock and surface synthetic seismograms after 40 s at the stations in Marmara Ereglisi, Corlu and Tekirdag. The amplitude of the later arrival phases from ASP-2 and ASP-3 are increased while the amplitude and high frequency content of S-wave part from ASP-1 decrease at Tekirdag stations.

To validate the models, the PGV values of the surface ground motions were used to calculate intensities for the stations by using Bilal and Askan (2014) PGV-intensity relationship. The intensity differences of the Model B with three asperities are minimum at the stations. Therefore, the characteristic model with three asperities is much appropriate for the 1912 Murefte earthquake.

The damage of the 1912 Murefte earthquake in the epicentral region was heavier than the other sites. Therefore the four sites located in the epicentral region were selected to understand characteristics of the ground motions. The results indicate that spectral acceleration characteristic change according to the site location respect to the location of fault and asperities. The amplitudes of the spectra of the near-fault sites are higher than the limits of the TBC (2007).

6.2 Future Tasks

The proposed future tasks from the results of this thesis are listed below:

1. The comprehensive microtremor array exploration studies for other provinces such as Edirne and Balikesir, and also for important large industrial districts (i.e. Bandirma) in the Marmara Region should be done. This provides to generate complete hazard analyses for the region.
2. The assumed Q-values for the layers were used for the site amplifications and synthetic seismogram generation in this study. Detailed Q-value estimation studies (i.e. spectral inversion method) are needed for the hazard assessment studies in the Marmara Region.
3. The low-frequency waves are over-estimated in the 1-D simulation due to local basin structures at an epicentral distance more than 150 km. Therefore, 3D velocity structure of the region must be studied.

REFERENCES

AIJ (1993) Earthquake motion and ground conditions: in commemoration of the 20th anniversary of the Research Subcommittee on Earthquake Ground Motion, the Architectural Institute of Japan. Edited and published by the Architectural Institute of Japan (AIJ).

Aki K, Richards PG (1980) Quantitative Seismology: Theory and Methods, W. H. Freeman, San Francisco, California.

Aksoy ME (2009) Active Tectonics and Paleoseismology of the Ganos Fault Segment and Seismic Characteristics of the 9 August 1912 Mürefte Earthquake of the North Anatolian Fault (Western Turkey). Eurasia Institute of Earth Sciences - Istanbul Technical University and Institute de Physique du Globe de Strasbourg - University of Strasbourg. Joint PhD program, 304p.

Aksoy ME, Meghraoui M, Vallee M, Çakır Z (2010) Rupture characteristics of the A.D. 1912 Murefte (Ganos) earthquake segment of the North Anatolian fault (Western Turkey). Geology 38:991-994.

Allen TI, Wald DJ (2007) Topographic slope as a proxy for seismic site-conditions (VS30) and amplification around the globe. U.S-Geol-Surv- Open-File Rept. 2007-1357, 69.

Altınok Y, Alpar B, Yaltırak C (2003) Şarköy - Mürefte 1912 Earthquake's Tsunami, extension of the associated faulting in the Marmara Sea, Turkey. J of Seismol 7:329-346.

Altunel E, Meghraoui M, Akyüz H S, Dikbas A (2004) Characteristics of the 1912 co-seismic rupture along the North Anatolian Fault Zone (Turkey): implications for the expected Marmara earthquake. Terra Nova 16:198-204.

Ambraseys N, Jackson J (2000) Seismicity of the Sea of Marmara (Turkey) since 1500. Geophys J Int 141: F1–F6.

Ambraseys NN, Finkel CF (1987) The Saros-Marmara earthquake of 9 August 1912. Earthq Eng Struct D 15:189-211.

Ambraseys NN, Finkel CF (1995) The Seismicity of Turkey and Adjacent Areas - A Historical Review, 1500–1800. M. S. Eren Publications and Books, Istanbul.

Aochi H, Ulrich T (2015) A probable earthquake scenario near Istanbul determined from dynamic simulations. Bull Seismol Soc Am 105:1468–1475.

Archuleta R, Hartzell S (1981) Effects of fault finiteness on near source ground motion. Bull Seismol Soc Am 71: 939–957.

Armijo R, Pondard N, Meyer B, Uçarkus G, Lepinay B M, Malavieille J, Dominguez S, Gustcher M A, Schmidt S, Beck C, Çagatay N, Çakir Z, Imren C, Eriş K, Natalin B, Özalaybey S, Tolun L, Lefevre I, Seeber L, Gasperini L, Rangin C, Emre O, Sarikavak K (2005) Submarine fault scarps in the Sea of Marmara pull- apart (North Anatolian Fault): Implications for seismic hazard in Istanbul. Geochem Geophy Geosy 6:Q06009.

Asten MW, Askan A, Ekincioglu EE, Sisman FN, Ugurhan B (2014) Site characterization in north-western Turkey based on SPAC and HVSR analysis of microtremor noise. Explor Geophys 45:74–85.

Barka A (1992) The North Anatolian Fault zone. Annales Tectonicae 6:164–95.

Basarir N (2011) Reassessment of the seismic parameters from historical seismograms of 1912-Mürefte-Şarköy, 1935-Erdek-Marmara Island and 1963-Çinarcik earthquakes. MSc Thesis. Boğaziçi University the Kandilli Observatory and Earthquake Research Institute, 49p.

Bécel A, Laigle M, de Voogd B, Hirn A, Taymaz T, Galvé A, Shimamura H, Mura Y, Lépine J, Sapin M, Özalaybey S (2009) Moho, crustal architecture and deep deformation under the North Marmara trough, from the Seismarmara leg1 offshore-onshore reflection-refraction survey. Tectonophysics 467:1–21.

Bilal M, Askan A (2014) Relationships between Felt Intensity and Recorded Ground-Motion Parameters for Turkey. Bull Seismol Soc Am 104:484-496.

Bouchon M (1979) Discrete Wavenumber Representation of Elastic Wave Fields in Three-space Dimensions.J Geophys Res 84; 3609–3614.

Bouchon M (1981) A Simple Method to Calculate Green's Functions in Elastic Layered Media. Bull Seismol Soc Am 71: 959–971.

Bouchon M (2003) A review of the discrete wavenumber method. Pure Appl Geophys 160: 445–465.

Bouchon M., Aki K. (1977) Discrete Wave number Representation of Seismic Source Wave Fields. Bull Seismol Soc Am 67:259–277.

Bozdag E, Kocaoglu, AH (2005) Estimation of site amplifications from shear-wave velocity profiles in Yesilyurt and Avcilar, Istanbul, by frequency-wavenumber analysis of microtremors. J Seismol 9: 87–98.

Brune JN (1970) Tectonic stress and the spectra of seismic shear waves from earthquakes. J Geophys Res 75:4997-5009. doi: 10.1029/JB075i026p04997.

Brune JN (1971) Seismic Sources, Fault Plane Studies and Tectonics. J Geophys Res 52:178-187. doi: 10.1029/EO052i005pIU178.

Buyuksarac A, Tunusluoglu MC, Bekler T, Yalciner CÇ, Karaca Ö, Ekinci YL, Demirci A, Dinç ŞÖ (2013) Canakkale Belediyesi Imar Planına Esas Jeolojik-Jeoteknik Etut Projesi (Geological-Geotechnical Investigation Project for the Master Plan of Canakkale Municipality)(in Turkish).

Cakır Z, Barka A, Chabalier J B, Armijo R, Meyer B (2003) Kinematics of the November 12, 1999 (Mw=7.2) Düzce Earthquake Deduced from SAR Interferometry. Turk J Earth Sci 12: 105-118.

CEN (2004) Eurocode 8- design of structures for earthquake resistance. Part 1: general rules, seismic actions and rules for buildings. European standard EN 1998-1, December 2004, European Committee for Standardization, Brussels.

Chimoto K, Karagoz O, Citak S, Ozel O, Yamanaka H, Hatayama K (2016) Microtremor array exploration at damaged sites during the 1912 Murefte Earthquake, Turkey. 5th IASPEI / IAEE International Symposium: Effects of Surface Geology on Seismic Motion, August 15-17, 2016 Taipei, Taiwan.

Chimoto K, Karagoz O, Citak S, Ozel O, Yamanaka H, Hatayama K (2015) Estimation of deep S-wave velocity structures from microtremor array measurements in Zeytinburnu and Tekirdag, Turkey. Proceedings of the 12th SEGJ International Symposium, 18-20 November, The Ito International Research Center, The University of Tokyo, Tokyo, Japan.

Dalguer LA, Miyake H, Irikura K (2004) Characterization of dynamic asperity source models for simulating strong ground motions. Proceedings of the 13th World Conference on Earthquake Engineering, No 3286.

Dalguer LA, Miyake H, Irikura K (20048) Surface Rupturing and Buried Dynamic-Rupture Models Calibrated with Statistical Observations of Past Earthquakes. Bull Seismol Soc Am 98:1147–1161.

Das S, Aki K (1977) A numerical study of two-dimensional spontaneous rupture propagation. Geophys J Roy Astr S 50:643–668.

Dhakal Y, Sasatani T, Takai N (2009) Tuning the deep velocity structure model by 1-D simulation of long-period S-waves. Proceedings of the 9th SEGJ International Symposium – Imaging and Interpretation, 12-14 October 2009, Sapporo, Japan.

Douglas J, Aochi H (2016) Assessing Components of Ground-Motion Variability from Simulations for the Marmara Sea Region (Turkey). Bull Seismol Soc Am 106:300-306.

Dziewonski A, Bloch S, Landisman M (1969) A technique for analysis of transient seismic signals. Bull Seismol Soc Am 59:427–444.

Erdik M (1999) Kocaeli and Duzce (Turkey) earthquakes. Bogazici University, Report No. 2000-12.

Erdik M (2005) Earthquake Risk, Earthquake Rapid Response System, and Early Warning System in Istanbul. Macalester International 15:12.

Erdik M and Drukal E (2001) A hybrid procedure for assessment of design basis earthquake ground motions for near-fault conditions. Soil Dyn Earthq Eng 21:431-443.

Erdik M, Demircioglu M, Sesetyan K, Durukal E, Siyahi B (2004) Earthquake hazard in Marmara Region, Turkey. Soil Dyn Earthq Eng 24:605–631.

Erdik M, Durukal E (2001) A Hybrid Procedure for the Assessment of Design Basis Earthquake Ground Motions for Near-fault Conditions. Soil Dyn. Earthq. Eng. 21:431–443.

Erdik M, Pınar A, Akkar S, Zulfikar C, Kalafat D, Kekovalı K, Ozel NM, Necmioglu O (2014) Earthquake Report: 24 May 2014 Northern Aegean Sea. BU Kandilli Observatory and Earthquake Research Institute. http://www.koeri.boun.edu.tr/sismo/2/wp-content/uploads/2014/05/KOERI_Press_Bulletin_NAn_EQ_24May2014_v7.pdf (last access 9 November 2016).

Ergin M, Ozalaybey S, Aktar M, Yalcin MN (2004) Site amplification at Avcilar, Istanbul. Tectonophysics 391:335–346.

Eshelby JD (1957) The determination of the elastic field of an ellipsoidal inclusion, and related problems. Proc Roy Soc Lond A MAT 241:376-396.

Evangelidis CP (2015) Imaging supershear rupture for the 2014 Mw 6.9 Northern Aegean earthquake by back projection of strong motion waveforms. Geophys Res Lett 42:307-315. doi: 10.1002/2014GL062513.

Gok E, Polat O (2012) Microtremor HVSR Study of Site Effects in Bursa City (Northern Marmara Region, Turkey). Earthquake Research and Analysis - New Frontiers in Seismology, Dr Sebastiano D'Amico (Ed.), ISBN: 978-953-307-840-3, InTech.

Grutas R, Yamanaka H (2012) Shallow shear-wave velocity profiles and site response characteristics from microtremor array measurements in Metro Manila, the Philippines. Explor Geophys 43:255–266.

Hartzell S, Frazier G, Brune J (1978) Earthquake modeling in a homogeneous half-space. Bull Seismol Soc Am 68:301– 316.

Haskell NA (1953) The dispersion of surface waves on multilayered media. Bull Seismol Soc Am 43:17–34.

Heaton TH, Helmberger DV (1979) Generalized ray models of the San Fernando earthquake. Bull Seismol Soc Am 69, 1311 – 1341.

Hisada Y (2000) A theoretical omega-squared model considering the spatial variation in slip and rupture velocity. Bull Seismol Soc Am 90:387–400.

Horasan G, Gülen L, Pınar A, Kalafat D, Özel N, Kuleli H, Işıkara A (2002) Lithospheric structure of the Marmara and Aegean regions, western Turkey. Bull Seismol Soc Am 92:322–329.

Iida M, Yamanaka H., Yamada N. (2005) Wave field estimated by borehole recordings in the reclaimed zone of Tokyo Bay. Bull Seismol Soc Am 95:1101–1119. doi:10.1785/0120040010.

Irikura K, Miyake H (2011) Recipe for predicting strong ground motion from crustal earthquake scenarios. Pure Appl Geophys 168:85–104. doi:10.1007/s00024-010-0150-9.

J Douglas, Aochi H (2016) Assessing components of ground-motion variability from simulations for the Marmara Sea region (Turkey) Bull Seismol Soc Am 106:300-306.

Karabulut H, Roumelioti Z, Benetatos, C, Komec Mutlu A, Ozalaybey S, Aktar M, Kiratzi A (2006) A source study of the 6 July 2003 (Mw 5.7) earthquake sequence in the Gulf of Saros (Northern Aegean Sea): Seismological evidence for the western continuation of the Ganos fault. Tectonophysics 412:195-216.

Karabulut H, Schmittbuhl J, Ozalaybey S, Lengline O, Komec Mutlu A, Durand V, Bouchon M, Daniel G, Bouin MP (2011) Evolution of the seismicity in the eastern Marmara Sea a decade before and after the 17 August 1999 Izmit earthquake. Tectonophysics 510:17-27. doi: 10.1016/j.tecto.2011.07.009.

Karagoz O, Chimoto K, Citak S, Ozel O, Yamanaka H, Hatayama K (2015) Estimation of shallow S-wave velocity structure and site response characteristics by microtremor array measurements in Tekirdag region, NW Turkey. Earth Planets Space 67:176. doi: 10.1186/s40623-015-0320-1.

Kennet BLN, Kerry NJ (1979) Seismic waves in a stratified half space. Geophys J R Astr Soc 57:557–583.

Ketin I (1948) Über die tektonisch-mechanischen Folgerungen aus den großen Anatolischen Erdbeben des letzten Dezennium. Geol Rundschau 36:77-83.

Ketin I (1968) Turkiye'nin genel tektonik durumu ile baslica deprem bolgeleri arasindaki iliski. Maden Tetkik ve Arama Enstitüsü Dergisi 71:129–134.

Kikuchi M, Kanamori H (1991) Inversion of complex body wave- III. Bull Seismol Soc Am 81:2335–2350.

Kiliç H, Özener PT, Ansal A, Yildirim M, Özaydin K, Adatepe Ş (2006) Microzonation of Zeytinburnu region with respect to soil amplification: A case study. Eng Geol 86: 238–255.

Kiratzi A, Tsakiroudi E, Benetatos C, Karakaisis G (2016) The 24 May 2014 (Mw6.8) earthquake (North Aegean Trough): Spatiotemporal evolution, source and slip model from teleseismic data. Phys Chem Earth 95:85-100.

Kitsunezaki C, Goto N, Kobayashi Y, Ikawa T, Horike M, Saito T, Kurota T, Yamane K, Okuzumi, K (1990) Estimation of P- and S-wave velocity in deep soil deposits for evaluating ground vibrations in earthquake. J Japan Soc Natural Disaster Science 9:1-17 (in Japanese).

Kudo K, Kanno T, Okada H, Ozel O, Erdik M, Sasatani T, Higashi S, Takahashi M, Yoshida (2002) Site specific issues for strong ground motions during the Kocaeli, Turkey earthquake of August 17, 1999, as inferred from array observations of microtremors and aftershocks. Bull Seismol Soc Am 92: 448–465. doi:10.1785/0120000812.

Kuzak DE (2003) Turkey Earthquake Risk Model, Financing the Risks of Natural Disasters World Bank Meeting ,Washington, DC , June 2-3,2003. (http://documentslide.com/documents/turkey-earthquake-risk-model-financing-the-risks-of-natural-disasters-world.html) (last access 13.02.2017).

Le Pichon X, Rangin N, Chamot-Rooke C, Şengör AMC (2003) The North Anatolian fault in the Sea of Marmara. J Geophys Res 108:2179-2179.

Lemoine A, Douglas J, Cotton F (2012) Testing the Applicability of Correlations between Topographic Slope and VS30 for Europe. Bull Seismol Soc Am 102: 2585-2599. doi: 10.1785/0120110240.

Lomax A, Snieder R (1994) Finding sets of acceptable solutions with a genetic algorithm with application to surface wave group dispersion in Europe. Geophys Res Lett 21:2617–2620.doi:10.1029/ 94GL02635.

Macovei G (1912) Sur La Tremblement De Terre De La Mer De Marmara Le 9 Aout 1912. Bull Sect Sci Acad Rumanie 1:9-18.

Matsuoka M, Wakamatsu K, Fujimoto K, Midorikawa S (2006) Average Shear-Wave Velocity Mapping Using Japan Engineering Geomorphologic Classification Map. Struct Eng/Earthq Eng, JSCE 23: 57-68.

McClusky S, Balassanian S, Barka A, Demir A, Ergintav S, Georgiev I, Gurkan O, Hamburger M, Hurst K, Kahle H, Kastens K, Kekelidze G, King R, Kotzev V, Lenk O, Mahmoud S, Mishin A, Nadariya M, Ouzounis A, Paradissis D, Peter Y, Prilepin M, Reilinger R, Sanli I, Seeger H, Tealeb A, Toksöz MN, Veis G (2000) Global Positioning System constraints on plate kinematics and dynamics in the eastern Mediterranean and Caucasus. J Geophys Res 105: 5695–5719.

Medvedev S, Sponheuer W, Karnik Y (1981) Report of the ad-hoc panel meeting of experts on the updating of the MSK-64 seismic intensity scale. Gerlands Beitr. Geophys. 90:261-268.

Mert A, Fahjan Y, Pinar A, Hutchings L (2014a) Prens adaları fayında kuvvetli yer hareketi benzesimleri. IMO Teknik Dergi 419:6775–6804.

Mert A, Fahjan Y, Pinar A, Hutchings L (2014b) Marmara Bölgesinde Ampirik Green Fonksiyon Yöntemiyle Deprem Benzeşimlerinin Elde Edilmesi. Hacettepe Universitesi Yerbilimleri Uygulama ve Araştırma Merkezi Bulteni, Yerbilimleri 35:55–78.

Mert A, Fahjan Y, Hutchings L J, Pınar A (2016) Physically based probabilistic seismic hazard analysis using broadband ground motion simulation: a case study for the Prince Islands Fault, Marmara Sea. Earth Planets Space (2016) 68:146.

Mihailovic J (1927). Trusne katastrofe na Mramornome moru. In Posebno izdan. srpse akad nauka 16:1-303.

Mindevalli OY, Mitchell BJ (1989) Crustal structure and possible anisotropy in Turkey from seismic surface wave dispersion. Geophys J Int 98:93–106.

MTA (2003) General Directorate of Mineral Research and Exploration (MTA) 1:500,000 scale geological map, Ankara, Turkey.

Nakamura H, Miyatake T (2000) An approximate expression of slip velocity time functions for simulation of near-field strong ground motion. Zisin (J Seism Soc Japan) 53:1–9 (in Japanese).

NEHRP (2003) NEHRP Recommended Provisions for Seismic Regulations for New Buildings and other Structures (FEMA 450), Part 1: Provisions, Building Seismic Safety Council, Washington, D.C.

Okada H (2003) The microtremor survey method. Geophysical Monograph series:Society of Exploration Geophysicists.

Okada H (2006) Theory of efficient array observations of microtremors with special reference to the SPAC method. Explor Geophys 37: 73–85. doi:10.1071/EG06073.

Ozalaybey S, Zor E, Ergintav S, Tapirdamaz M-C (2011) Investigation of 3-D basin structures in the Izmit Bay area (Turkey) by single-station microtremor and gravimetric methods. Geophys J Int 186:883–894.

Ozel N M, Sasatani T, Ozel O (2004) Strong ground motion during the largest aftershock (Mw=5.8) of the 1999 Izmit earthquake, Turkey. Tectonophysics 391:347–355.

Ozel O, Cranswick E, Meremonte M, Erdik M, Safak E (2002) Site Effects in Avcilar, West of Istanbul, Turkey from Strong and Weak Motion Data. Bull Seismol Soc Am 92: 499-508.

Ozel O, Sasatani T, Kudo K, Okada H, Kanno T, Tsuno S, Yoshikawa M, Noguchi S, Miyahara M, Goto H (2004) Estimation of S-wave velocity structures in Avcilar–Istanbul from array microtremor measurements. Jour. Fac. Sci., Hokkaido Univ., Ser. VII (Geophysics), 12: 115-129.

Panza G F (2005) Intensity (technical report) The Abdus Salam International Center for Theoretical Physics – SAND group. Trieste, Italy. (http://www.isprambiente.gov.it/files/progetti/inqua/correlation-among-intensity-scales-panza.pdf (last access 20 December 2016).

Picozzi M, Strollo A, Parolai S, Durukal E, Ozel O, Karabulut S, Zschau J, Erdik M (2009) Site characterization by seismic noise in Istanbul, Turkey. Soil Dyn Earthq Eng 29:469-482.

Pinar A. (2014) Teleseismic Bodywave Modeling. In Erdik et al. Earthquake Report: 24 May 2014 Northern Aegean Sea http://www.koeri.boun.edu.tr/sismo/2/wp-content/uploads/2014/05/KOERI_Press_Bulletin_NAn_EQ_24May2014_v7.pdf (last access 9 November 2016).

Pulido N, Ojeda A, Atakan K, Kubo T (2004) Strong ground motion estimation in the Sea of Marmara region (Turkey) based on a scenario earthquake. Tectonophysics 391:357–374.

Sadi D Y (1912) Marmara Havzasının 26-27 Temmuz Hareket-i Arzı 15 Eylül 1328. Resimli Kitap Matbaası, İstanbul, 45.

Sahin A, Sisman R, Askan A, Hori M (2016) Development of integrated earthquake simulation system for Istanbul. Earth Planets Space 68:115.

Saltogianni V, Gianniou M, Taymaz T, Yolsal-Çevikbilen S, Stiros S (2015) Fault slip source models for the 2014 Mw 6.9 Samothraki-Gökçeada earthquake (North Aegean Trough)

combining geodetic and seismological observations. J Geophys Res Solid Earth 120:8610–8622. doi:10.1002/2015JB012052.

Sekiguchi H, Iwata T (2002) Rupture process of the 1999 Kocaeli, Turkey, earthquake estimated from strong-motion waveforms. Bull Seismol Soc Am 92:300–311.

Şengör AMC (1979) The North Anatolian transform fault: its age, offset and tectonic significance. J Geol Soc of London 136: 269-282.

Siyako M, Huvaz Ö (2007) Eocene stratigraphic evolution of the Thrace Basin, Turkey. Sediment Geol 198:75-9. doi: 10.1016/j.sedgeo.2006.11.008.

Somerville P, Irikura K, Graves R, Sawada S, Wald D, Abrahamson N, Iwasaki Y, Kagawa T, Smith N, Kowada A (1999) Characterizing crustal earthquake slip models for the prediction of strong ground motion. Seismol Res Lett 70:59–80.

Sørensen BM, Pulido N, Atakan K (2007) Sensitivity of ground-motion simulations to earthquake source parameters: a case study for Istanbul, Turkey. Bull Seismol Soc Am 97:881–900.

Sørensen M, Oprsal I, Bonnefoy-Claudet S, Atakan K, Martin Mai P, Pulido N, Yalcinar C (2006) Local site effects in Atakoy, Istanbul, Turkey, due to a future large earthquake in the Marmara Sea. Geophys J Int., 167:1413–1424.

Spagnuolo E, Akinci A, Herrero A, Pucci S (2016) Implementing the Effect of the Rupture Directivity on PSHA for the City of Istanbul, Turkey. Bull Seismol Soc Am 106:6. doi:10.1785/0120160020.

Spudich P, Archuleta R (1987) Techniques for earthquake ground-motion calculation with application to source parameterization of finite faults, seismic strong motion synthetics. In: Bolt BA (ed) Seismic strong motion synthetics, Academic Press Inc., Orlando, 205–265.

Stewart J, Seyhan E, Boore DM, Campbell KW, Erdik M, Silva WJ, Di Alessandro C, Bozorgnia Y (2012) Site Effects in Parametric Ground Motion Models for the GEM-PEER Global GMPEs Project. 15th World Conference on Earthquake Engineering, Lisboa, Portugal.

Takeo M (1985) Near-field synthetic seismograms taking into account of the effects of anelasticity: The effects of anelastic attenuation on seismograms caused by a sedimentary layer. Meteorol Geophys 36:245– 257 (in Japanese with English abstract).

Tanırcan G (2012) Istanbul icin 3 boyutlu hız modeli ile yer hareketi simulasyonu. J Fac Eng Archit Gazi 27:27-35.

Tanırcan G, Savaş N (2011) Strong Ground Motion Simulation by the Empirical Green's Function Method for Bursa-Yalova Region, Turkey, B Earthq Eng 9: 1327-1338.

TBC (2007) Specification for Buildings to be Built in Seismic Zones (Turkish Earthquake Building Code) 2007, The Official Gazette of Turkey, 6 March 2007, No: 26454.

Tekirdag Municipality (2006) Geology Maps of Tekirdag (1:25.000 scale), Project for Investigation of Suitability for Settlement.

Wessel P, Smith WHF (1998) New, improved version of the Generic Mapping Tools released. EOS 79:579.

Yalcinkaya E, Pinar A, Uskuloglu O, Tekebas S, Firat B (2012) Selecting the most suitable rupture model for the stochastic simulation of the 1999 Izmit earthquake and prediction of peak ground motions. Soil Dyn Earthq Eng 42:1-16.

Yamanaka H (2007) Inversion of surface-wave phase velocity using hybrid heuristic search method. Butsuri Tansa 60: 265–275 (in Japanese). doi:10.3124/segj.60.265.

Yamanaka H, Ishida H (1996) Application of Genetic Algorithms to an inversion of surface-wave dispersion data. Bull Seismol Soc Am 86: 436–44.

Zaineh H E, Yamanaka H, Dakkak R, Khalil A, Daoud M (2012) Estimation of shallow S-Wave velocity structure in Damascus city Syria, using microtremor exploration. Soil Dyn Earthq Eng 39: 88-99.

Zaineh H E, Yamanaka H, Dhakal YP, Dakkak R, Daoud M (2013) Strong ground motion simulation during the November 1759 Earthquake along Serghaya Fault in the metropolitan of Damascus, Syria. J Seismol 17:1295-1319. doi: 17.10.1007/s10950-013-9393-0.

Zor E, Özalaybey S, Karaaslan A, Tapirdamaz MC, Özalaybey ÇS, Tarancioğlu A, Erkan B (2010) Shear wave velocity structure of the İzmit Bay area (Turkey) estimated from active–passive array surface wave and single-station microtremor methods. Geophys J Int 182: 1603–1618.

Appendix A

Inversion of Phase Velocities from Dispersion Curves and Horizontal-to-Vertical Spectral Ratios

The 1:12,000-scaled geology map of Tekirdag Municipality (2006), Muratli, Corlu and Marmara Ereglisi regions are from MTA (2003) given in Figure A.1. Fitness of observed phase velocity and calculated from the inversion models, fitness of the observed H/V spectral ratio and calculated ellipticity for the fundamental mode of Rayleigh wave for different geological groups are given in Figure A.2. The inversion results of the all sites are given in Table A.1.

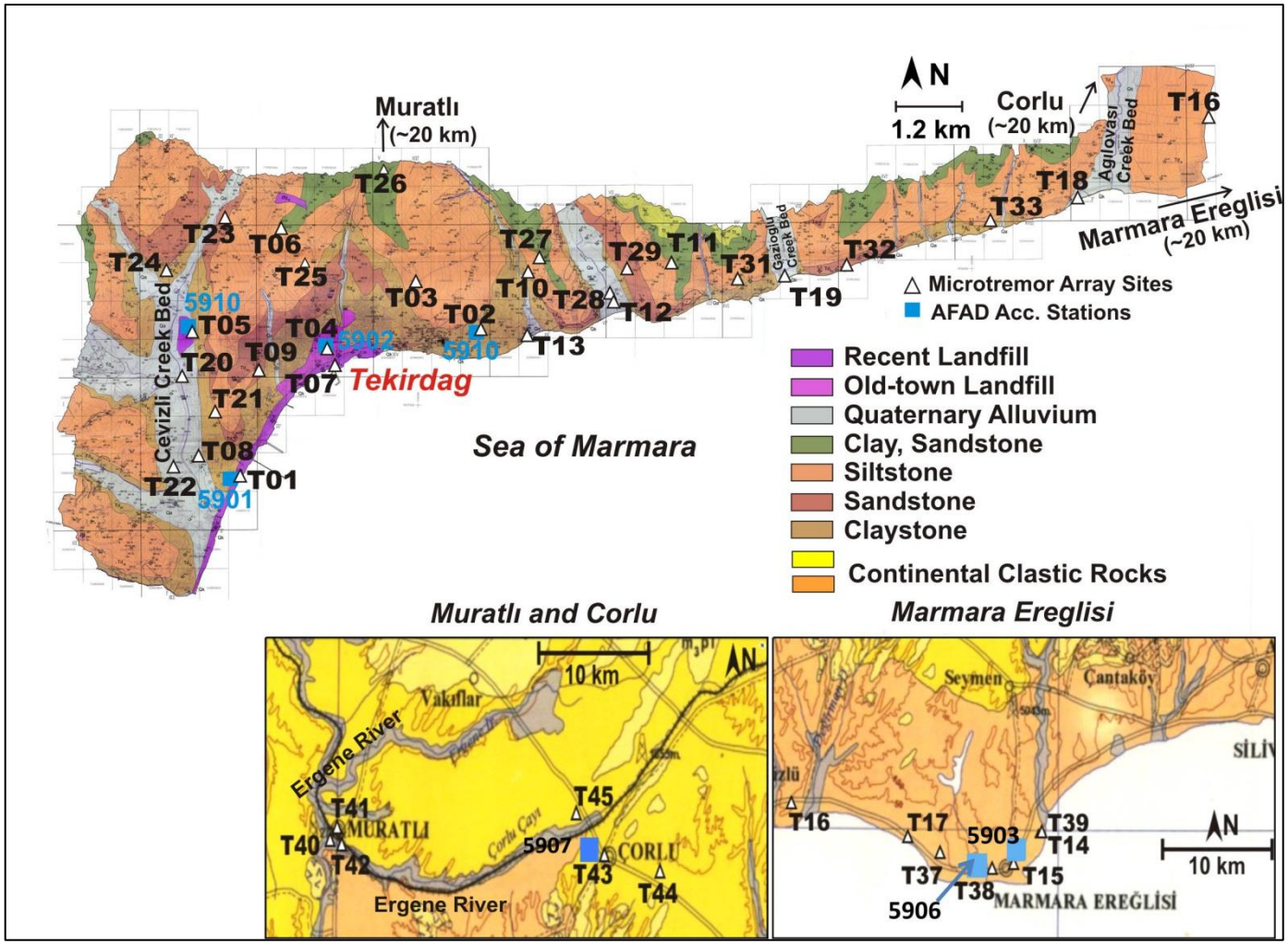

Figure A.1. 1:12,000-scaled geology map of Tekirdag Municipality (2006), Muratli, Corlu and Marmara Ereglisi regions are from MTA (2003) web page http://www.mta.gov.tr/v2.0/daire-baskanliklari/jed/index.php?id=500bas) 1:500,000 Istanbul Geology Map. White triangles are microtremor small array observation sites; blue squares are AFAD strong motion stations.

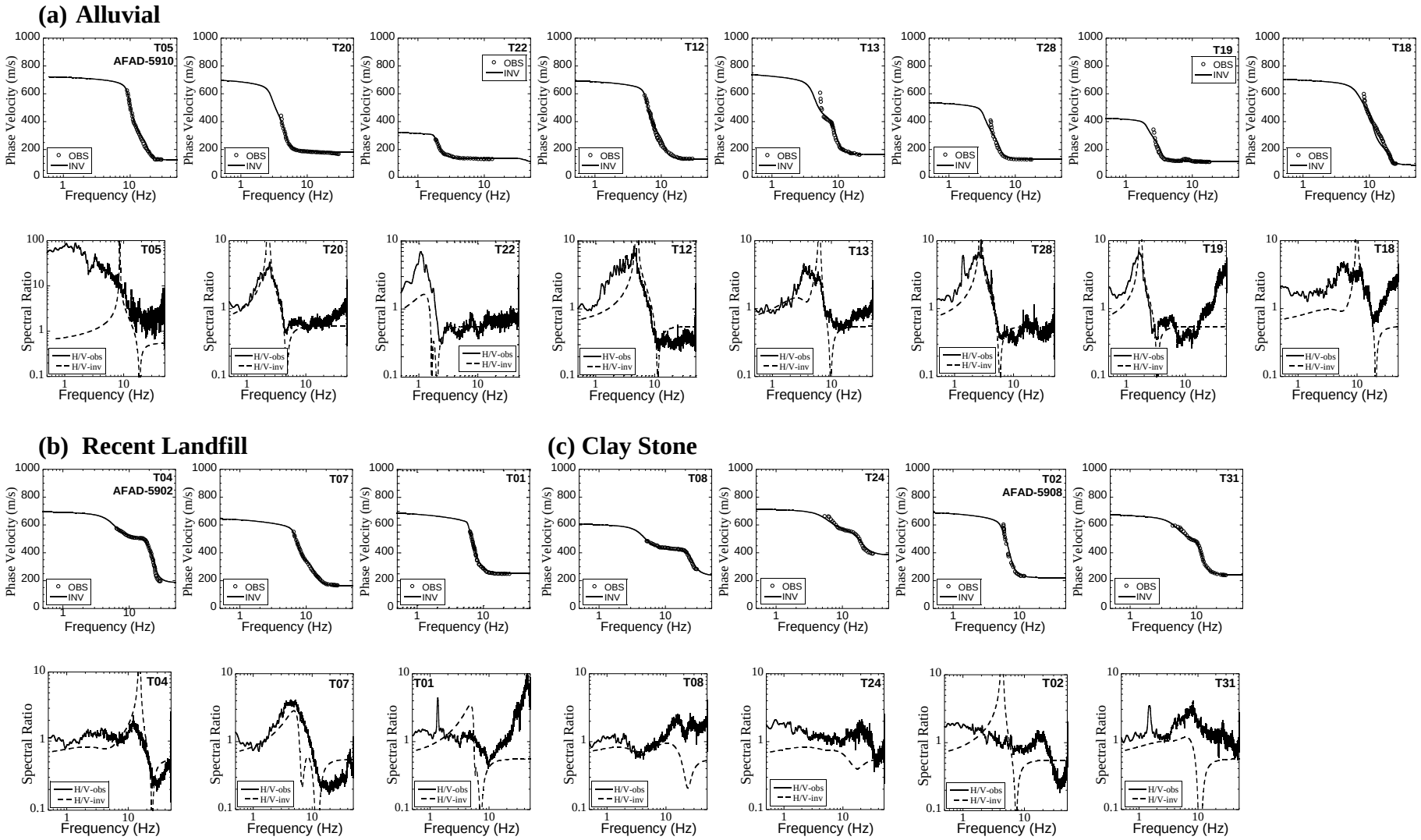

Continue on next page

(d) Sand Stone

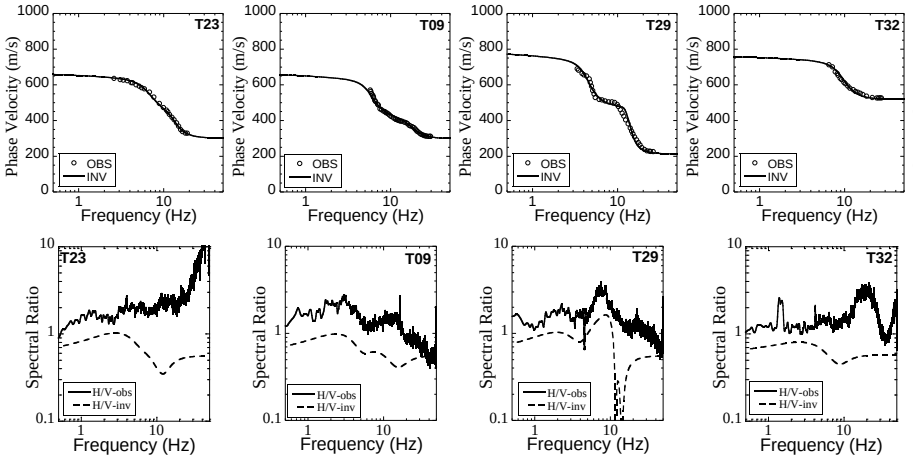

(f) Clay&Sand Stone

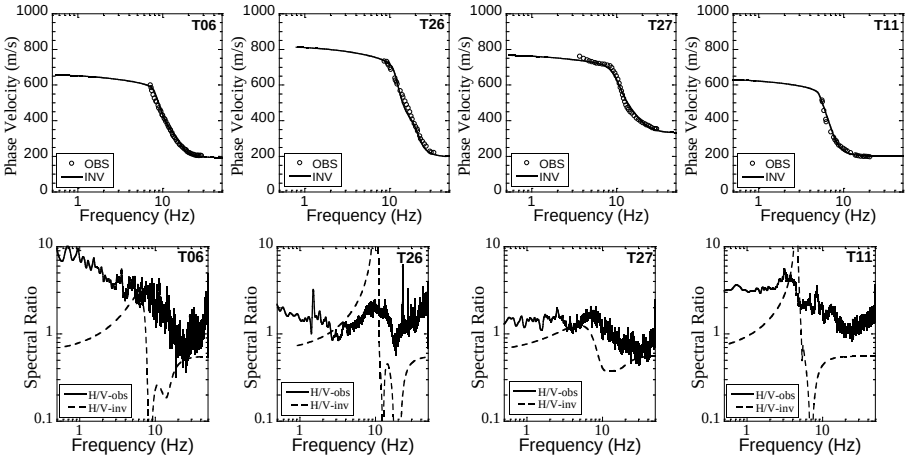

(e) Silt Stone

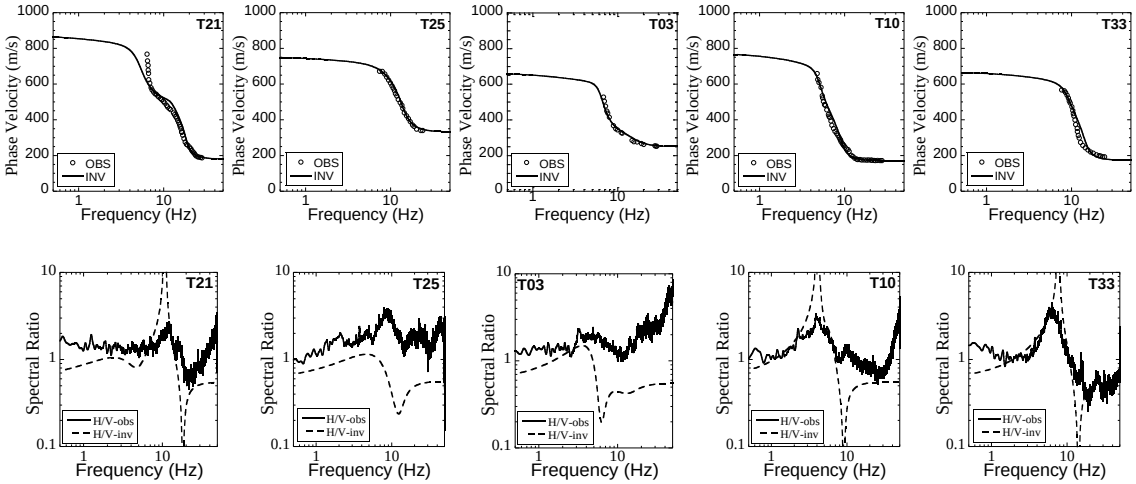

Continue on next page.

(g) Continental Clastic Rocks (Murali and Corlu)

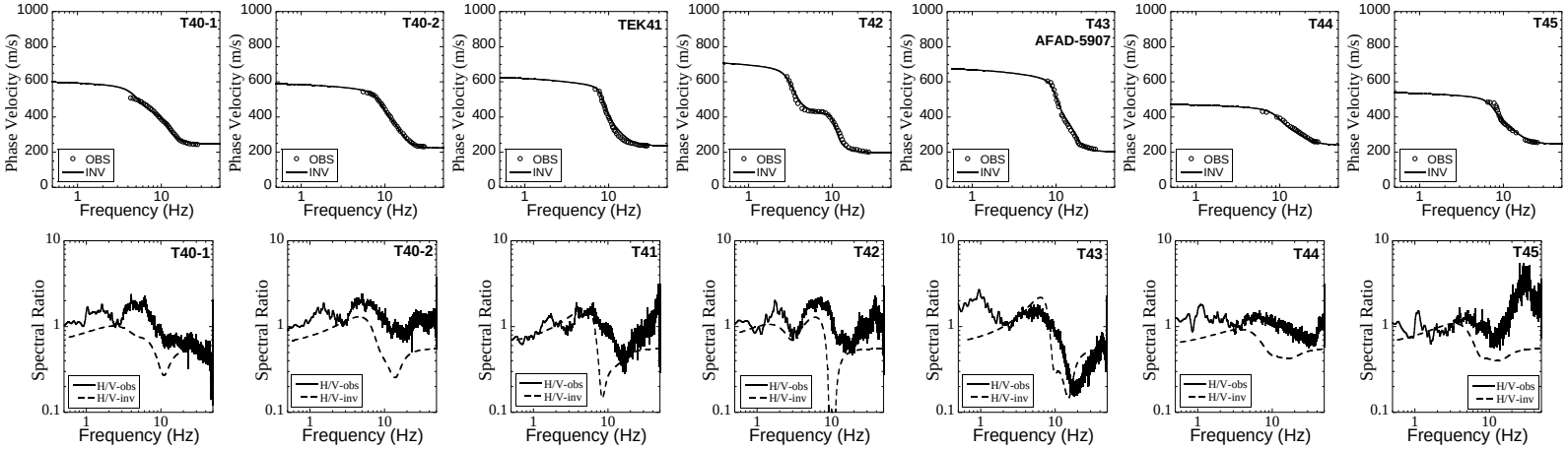

(h) Continental Clastic Rocks (Marmara Ereglisi)

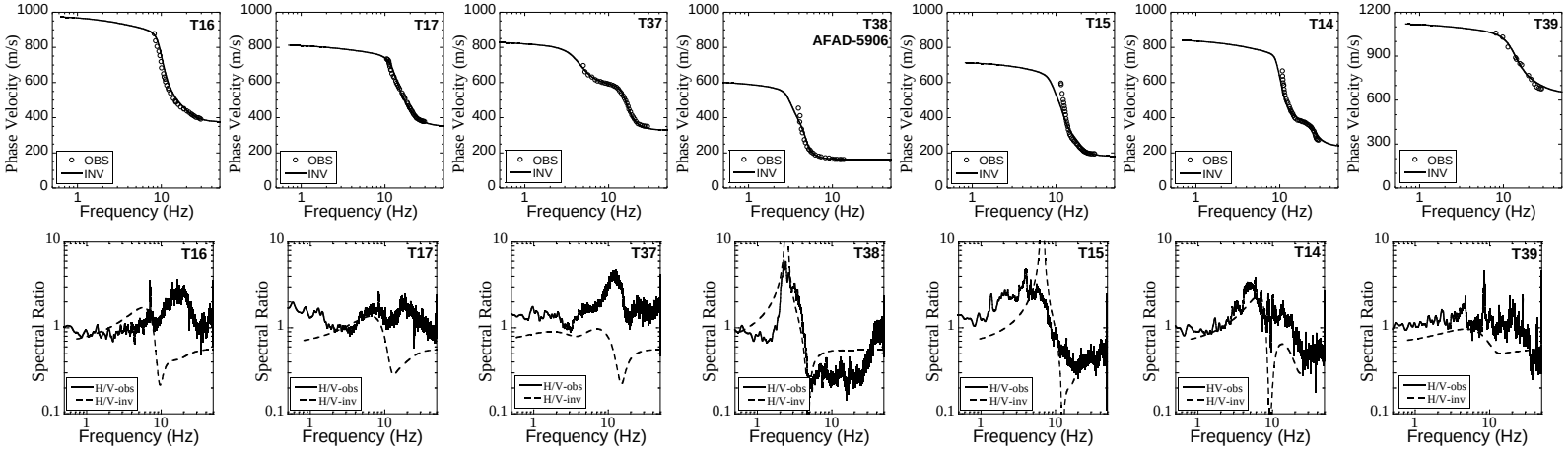

Continue on next page.

Gazikoy-Sarkoy-Gelibolu-Enez-Gokceada-Canakkale

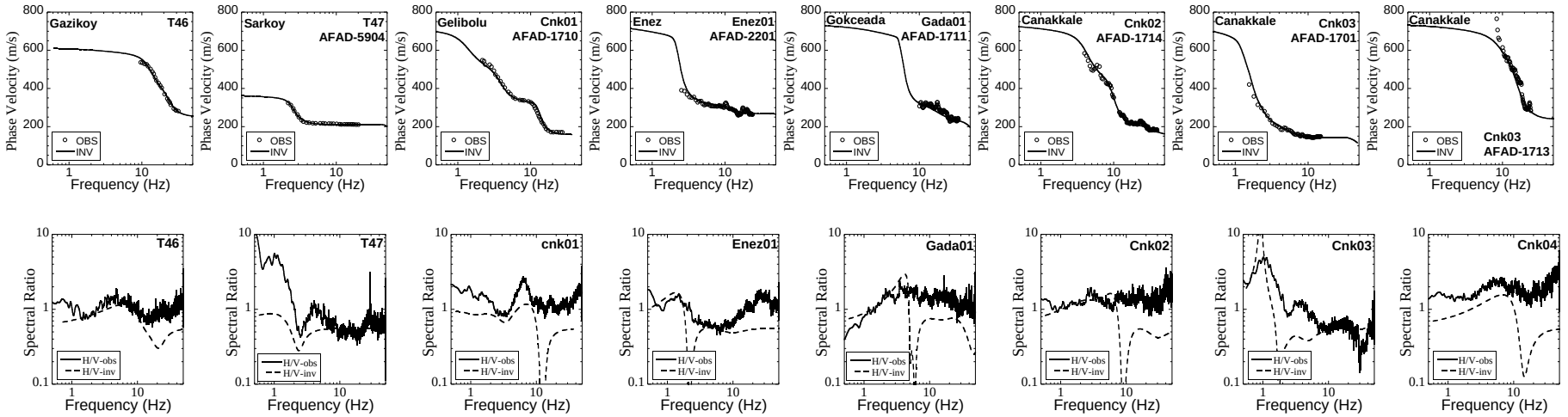

Figure A.2. Top row: Comparisons between the observed (open circle) and calculated (solid line) phase velocities. Bottom row: Spectral ratio (H/V) of the observed microtermor data (solid line) with computed ellipcity of the fundamental-mode Rayleigh waves (dashed lines).

Murefte

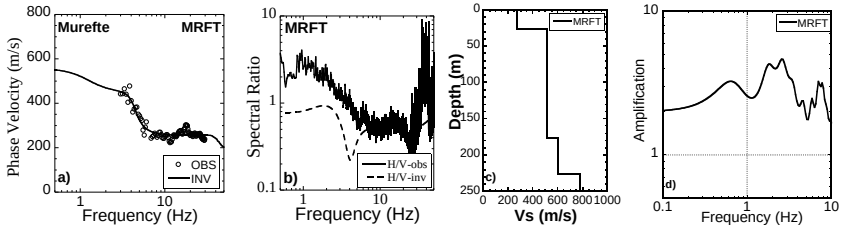

Figure A.3.a) Comparisons between the observed (open circle) and calculated (solid line) phase velocities. b) Spectral ratio (H/V) of the observed microtermor data (solid line) with computed ellipcity of the fundamental-mode Rayleigh waves (dashed lines). c) 1D S-wave profile d) Site amplification.

Table A.1. A) Tekirdag, Muratlı, Corlu, Marmara Ereglisi. B) Gazikoy-Sarkoy-Gelibolu-Enez-Gokceada-Canakkale-Murefte. S-wave velocities (Vs) and thicknesses (h) of the layers (1 to 5) at the microtremor array sites. SG: Site Group; Geology index (GI): al: Alluvium, c: Claystone, sa: Sandstone, s: Siltstone, cs: Clay&Sand stone rf: Recent Fill, lm: Limestone cr: Continental Clastic Rocks units; h_{eng}: Assumed thickness of the engineering bedrock; H_{eng}: Depth of the engineering bedrock from surface; (L): Large array result.

A) Tekirdag, Muratlı, Corlu, Marmara Ereglisi

SG	Site	GI	1st Layer		2nd Layer		3rd Layer		4th Layer		5th Layer		h_{eng}	H_{eng}
			Vs (m/s)	h (m)	Vs (m/s)	h (m)	Vs (m/s)	h (m)	Vs (m/s)	h (m)	Vs (m/s)	h (m)	(m)	(m)
a	T05	al	129.4	3.5	---	---	538.1	15.6	769.2	133	1135 (L)	---		19.1
	T20	al	192.3	18.9	481.9	18.1	---	---	748.4	---	---	---		37
	T12	al	136.6	5.8	466.2	17	---	---	738.2	---	---	---		22.8
	T13	al	171.7	8.3	480.7	40.9	---	---	793.7	---	---	---		49.2
	T18	al	92.1	2.2	498.8	27.9	---	---	750.4	---	---	---		30.1
	T28	al	134.8	11.1	394.8	22.7	573.5	---	---	---	---	---	15	49
	T19	al	121.2	17.8	453.2	---	---	---	---	---	---	---	20	38
	T22	al	142.4	31.8	349.3	---	---	---	---	---	---	---	25	56.8
b	T04	rf	193.1	3.7	---	---	571.0	38.9	742.2	87	1609 (L)	---		42.6
	T07	rf	168.8	5.6	361.2	17.6	687.2	---	---	---	---	---	15	39
	T01	rf	262.3	14.3	481.9	15.2	---	---	731.6	---	---	---		29.5
c	T02	c	231.4	14	---	---	546.9	19.8	735.6	---	---	---		33.8
	T08	c	246.03	4.3	467.9	39.6	648.1	---	---	---	---	---	10	54
	T24	c	---	---	403.6	9.4	621.4	36.3	762.4	---	---	---		45.7
	T31	c	252.02	9.5	---	---	556.2	38.2	720.2	---	---	---		47.7
d	T09	sa	314.01	8.1	465.7	27.1	---	---	701.6	---	---	---		35.2
	T23	sa	316.9	10.4	---	---	518.3	24.8	702.7	---	---	---		35.2
	T29	sa	223.1	7.1	---	---	543.6	46.4	830.5	---	---	---		53.5
	T32	sa	---	---	---	---	547.8	25.04	806.5	---	---	---		25
e	T03	s	261.6	7.7	368.4	17.4	---	---	701.6	38	849 (L)	---		25.1
	T10	s	179.8	9.1	452.5	27	---	---	822.9	---	---	---		36.1
	T21	s	189	5	---	---	589.8	42.7	929.5	---	---	---		47.7
	T25	s	---	---	350.2	11.1	643.0	20.2	798.4	---	---	---		31.3
	T33	s	182.4	5.8	441.6	14.7	---	---	707.6	---	---	---		20.5

Table A1. continue

SG	Site	GI	1st Layer		2nd Layer		3rd Layer		4th Layer		5th Layer		h_{eng}	H_{eng}
			Vs (m/s)	h (m)	Vs (m/s)	h (m)	Vs (m/s)	h (m)	Vs (m/s)	h (m)	Vs (m/s)	h (m)	(m)	(m)
f	T06	cs	200.3	5.6	375.8	13.3	---	---	700	---	---	---		18.9
	T11	cs	209.4	11.9	417.5	18.3	672.4	---	---	---	---	---	20	50.2
	T26	cs	204.4	4.1	442.8	12.04	---	---	867.7	---	---	---		16.14
	T27	cs	---	---	346.7	8.2	520.6	14.1	816.7	---	---	---		22.3
g	T40-1	cr	258.8	9.5	462.4	30	640.4	---	---	---	---	---	20	59.5
	T40-2	cr	233.7	6.6	413.8	14.3	626.8	---	---	---	---	---	15	35.9
	T41	cr	247.8	7.3	377.8	12.1	664.7	---	---	---	---	---	25	44.4
	T42	cr	207.2	8.4	474.8	54.7	---	---	763.2	---	---	---		63.1
	T43	cr	211.5	5.5	410	13.3	---	---	717.8	---	---	---		18.8
	T44	cr	252.4	5.6	354.2	10.3	500.0	---	---	---	---	---	5	20.9
	T45	cr	258.4	7.3	377	14.3	573.3	---	---	---	---	---	5	26.6
h	T16	cr	---	---	394.3	9	556.2	15.6	---	---	1046	---	13	37.6
	T37	cr	---	---	345.2	9.3	663.4	55	890		---	---		64.3
	T17	cr	---	---	368.1	7.7	540.1	10.6	867.9	---	---	---		18.3
	T38	cr	170.7	16.3	441.7	31.8	645.7	---	---	---	---	---	13	61.1
	T15	cr	188.2	4.4	336.1	9.3	---	---	762.1	---	---	---		13.7
	T14	cr	246.2	4.2	427.5	15.1	---	---	900.1	22	1313 (L)	236		19.3
	T39	cr	---	---	---	---	681.9	10.6	803.5	15.5	1205	---		10.6

B) Gazikoy-Sarkoy-Gelibolu-Enez-Gokceada-Canakkale-Murefte

Site	GI	1st Layer		2nd Layer		3rd Layer		4th Layer		5th Layer		6th Layer		h_{eng}	H_{eng}
		Vs (m/s)	h (m)	Vs (m/s)	h (m)	Vs (m/s)	h (m)	Vs (m/s)	h (m)	Vs (m/s)	h (m)	Vs (m/s)	h (m)	(m)	(m)
T46	cr	264.1	4.9	447.4	10.6	648.0	---	---	---	---	---	---	---	104.2	119.7
T47	cr	221.6	38	389		---	---	---	---	---	---	---	---	10	48
Cnk01	cr	165.4	5.4	372.6	36.9	573.1	93.6	635.5	78.9	765.4	---	---	---		214.8
Enez01	al	280	11	350	44	470	---	---	---	---	---	---	---	25	80
Gada01	cr	142	1.2	260	5.1	350	---	---	---	---	---	---	---	20	26.3
Cnk02	cr	160	2.0	230	7.0	390	6	500	17	550	18	690	---	20	52
Cnk03	al	150	12	230	29	380	55	480	---	---	---	---	---	25	66
Cnk04	lm	250	5	380	3	410	3	580	6	620	12	780	---		29
MRFT	cr	269.4	26.8	509.4	149.6	600.5	---	---	---	---	---	---	---	50	226.4

Appendix B

Multiple Filter Analyses of the 2014 Gokceada Earthquake

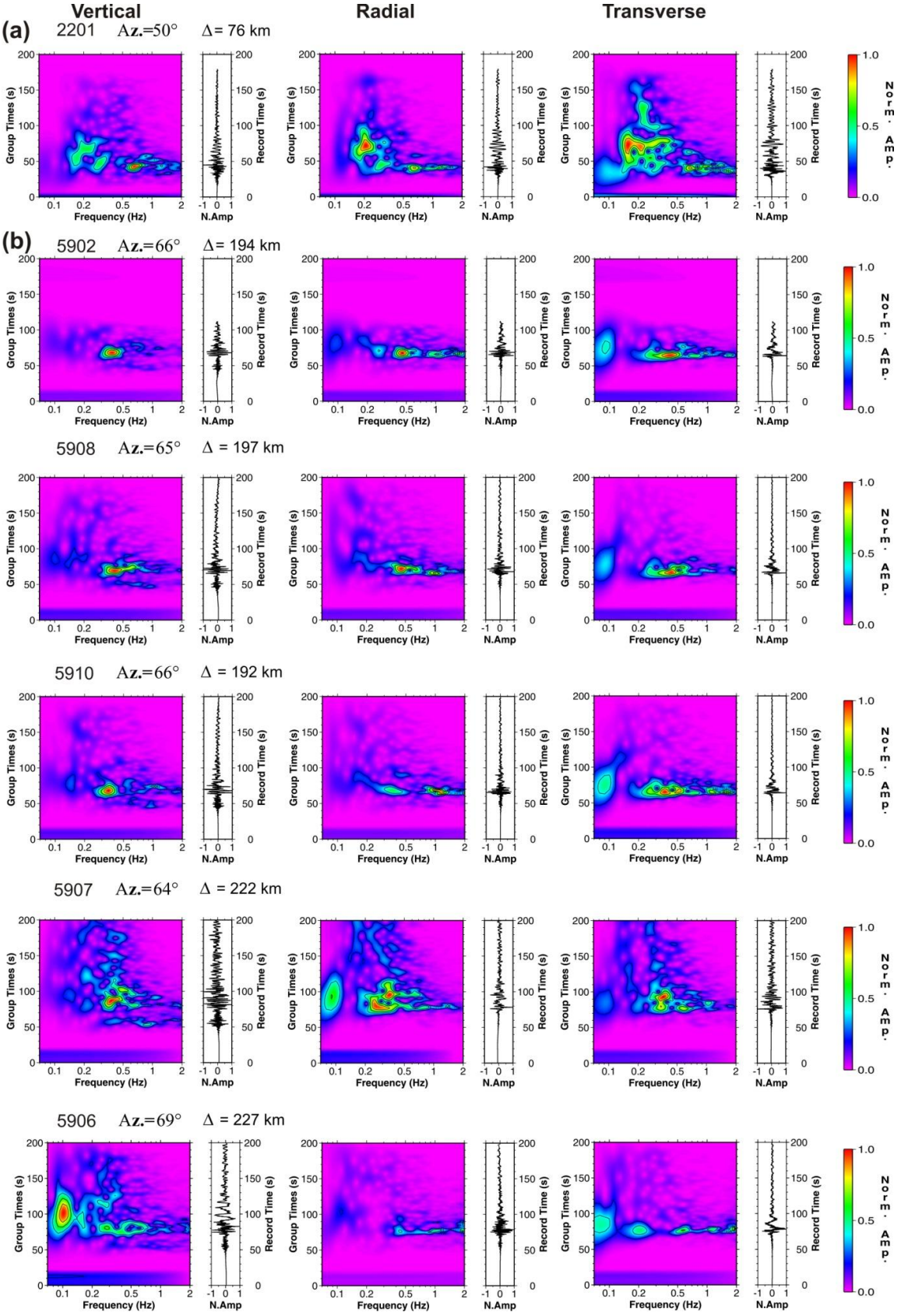

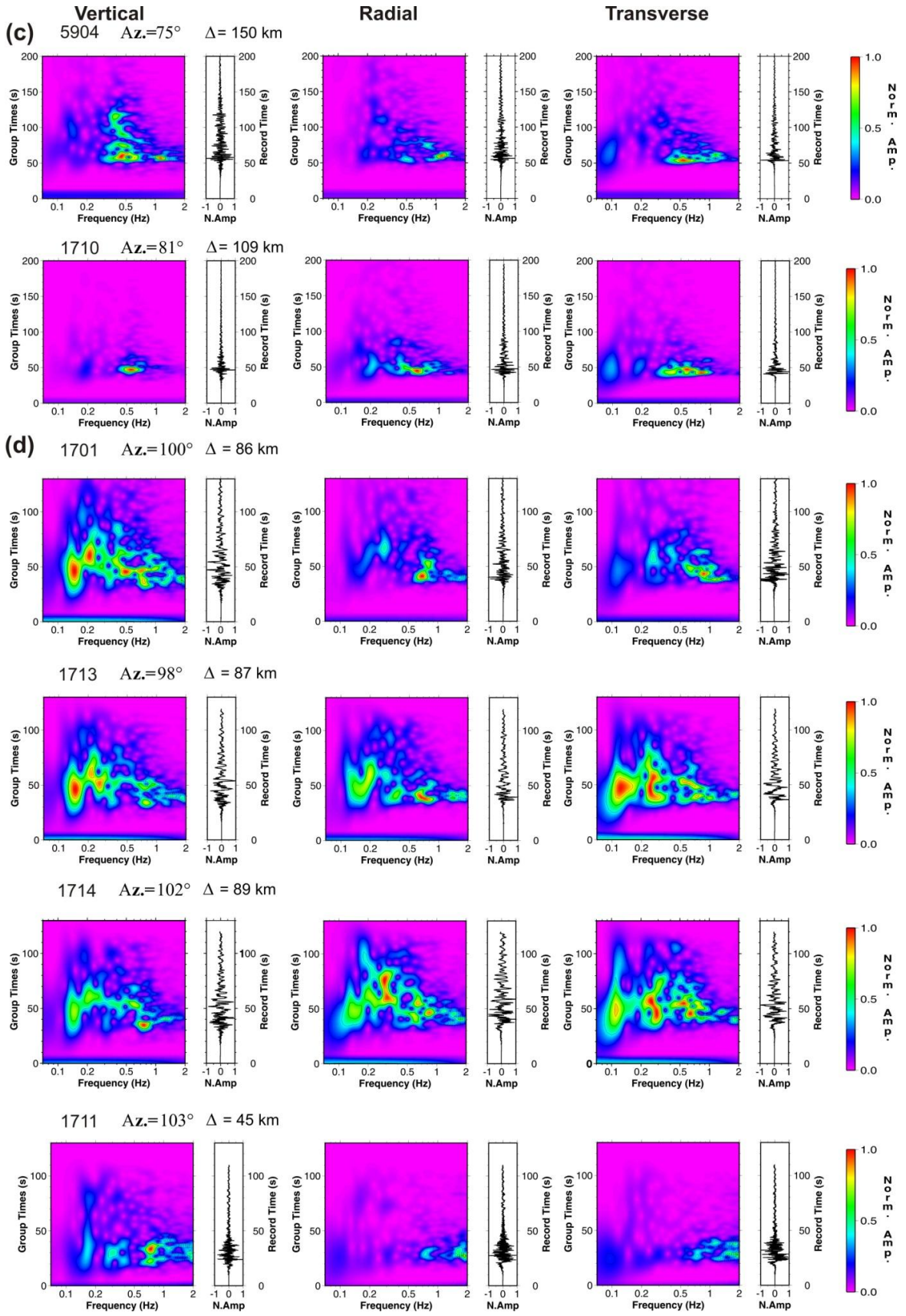

Figure B.1. Results of multiple filter analyses for the velocity waveforms of the 2014 Gokceada earthquake. The normalized amplitudes were shown in the frequency versus group-time domain with colored scale. Each waveform envelope was normalized with the maximum envelope amplitude in the spectra. The seismograms are given at the right side of each plot. AFAD station code, station azimuth and epicentral distance are given above the graphics.

Appendix C

Spectral Acceleration and Site Classification in Turkish Building Code 2007

The spectral acceleration coefficient (*A(T)*) in the Turkish Building Code 2007 (TBC-2007) is defined as

$$A(T) = Ao * I * S(T)$$

where *Ao* is the effective ground accelerations coefficient in unit of *g*, *I* is the building importance factor and *S(T)* is the spectrum coefficient. The value of *Ao* is selected according to the seismic zones (Table C.1).

Table C.1 Effective ground accelerations coefficients according to the seismic zones in Turkey.

Seismic Zone	***Ao* (g)**	***Ao* (cm/s^2)**
1	0.4	392
2	0.3	294
3	0.2	196
4	0.1	98

The building importance factor (I) in the TBC-2007 ranges from 1.0 and 1.5. The buildings that will be used after an earthquake such as hospitals, fire departments, telecommunication facilities, power generation and distribution facilities, administration buildings, and buildings that contain or store toxic, explosive and flammable materials have the importance factor of 1.5. Educational buildings and facilities, dormitories, military buildings, prisons and museums are defined as intensively and long-term occupied buildings and their factor is 1.4. The factor of intensively but short-term occupied buildings such as sport facilities, cinema, theatre and concert halls is 1.2. The other buildings (i.e. residential and office buildings, hotels) are designed with I = 1.0.

The spectrum coefficient S(T) is a function of period. The maximum value of S(T) is fixed assuming the amplification factor of 2.5 (Bommer et al. 2000) for a standard 5% damped spectrum. The general definition of damping level (η) is

$$\eta = \sqrt{\frac{10}{5+\xi}}$$

where ξ is the factor of damping. In example, ξ is 5 for 5% damped spectrum and η is calculated as 1.0 in the TBC-2007.

The maximum value of *S(T)* is constant between the spectrum characteristic periods (T_A and T_B) given in Table C.2 that depends on the local site classifications defined in Table C.3. The functional form of *S(T)* is

$$S(T) = 1.0 + (2.5\eta - 1)\,(T / T_A) \qquad (0 \le T \le T_A)$$

$$S(T) = 2.5\eta \qquad (T_A < T \le T_B)$$

$$S(T) = (2.5\eta - 1)\,(T_B / T)^{0.8} \qquad (T_B < T)$$

and the graphical presentation is given in Figure C.1.

Table C.2 Spectrum characteristic periods in the TBC-2007 according to the local site classification defined in Table C.3.

Local site class	T_A **(s)**	T_B **(s)**
Z1	0.10	0.30
Z2	0.15	0.40
Z3	0.15	0.60
Z4	0.20	0.90

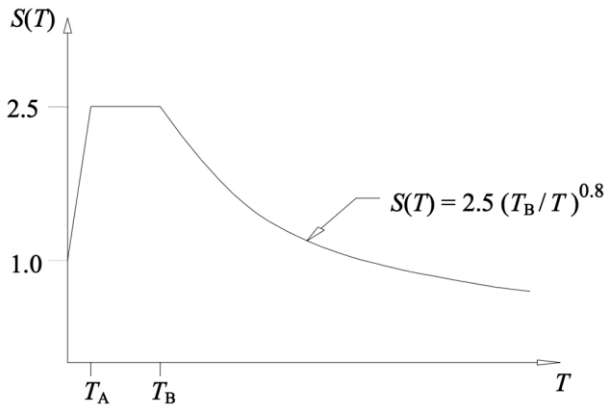

Figure C.1. Spectrum coefficient, *S(T)*, for 5% damping as a function of period given in the TBC-2007. The maximum amplification factor is 2.5.

Table C.3. Soil groups (A) and local site class definition (B) in the TBC-2007. Additionally, equivalent NEHRP classification used in this study is given in B.

A

Soil Group	Description of Soil Group	Vs (m/s)
(A)	1. Massive volcanic rocks, unweather sound metamorphic rocks, stiff cemented sedimentary rocks	> 1000
	2. Very dense sand, gravel	> 700
	3. Hard clay and silty clay	> 700
(B)	1. Soft volcanic rocks such as tuff and agglomerate, weathered cemented sedimentary rocks with planes of discontinuity	700 - 1000
	2. Dense sand, gravel	400 - 700
	3. Very stiff clay, silty clay	300 - 700
(C)	1. Highly weathered soft metamorphic rocks and cemented sedimentary rocks with planes of discontinuity	400 - 500
	2. Medium dense sand and gravel	200 - 400
	3. Stiff clay and silty clay	200 - 300
(D)	1. Soft, deep alluvial layers with high ground water level	< 200
	2. Loose sand	< 200
	3. Soft clay and silty clay	< 200

B

Local Site Class	Soil Group and Top most Soil Layer Thickness (h_1)	NHERP class equivalent
Z1	Group (A) soils Group (B) soils with $h_1 \leq 15$ m	A - B
Z2	Group (B) soils with $h_1 > 15$ m Group (C) soils with $h_1 \leq 15$ m	B - C
Z3	Group (C) soils with 15 m $< h_1 \leq 50$ m Group (D) soils with $h_1 \leq 10$ m	C - D
Z4	Group (C) soils with $h_1 > 50$ m Group (D) soils with $h_1 > 10$ m	D - E